Single-Stage Interleaved Photovoltaic (PV) Step-up Resonant Converter Modules for Magnetron Application

AREF MOLAEI

A THESIS SUBMITTED TO
THE FACULTY OF GRADUATE STUDIES
IN PARTIAL FULFILLMENT OF THE REQUIREMENTS
FOR THE DEGREE OF
MASTER OF APPLIED SCIENCE

GRADUATE PROGRAM IN
ELECTRICAL AND COMPUTER ENGINEERING
YORK UNIVERSITY
TORONTO, ONTARIO

SUMMER 2025

Abstract

With the growing need for compact, efficient, high-voltage DC power supplies for magnetron applications and the global interest in renewable energy sources, the power electronics industry has new challenges and opportunities. Photovoltaic (PV) energy, as a clean energy source, is widely available and requires efficient power conversion interfaces to satisfy the magnetron load's high-voltage, low-ripple, and high-efficiency demands.

In this thesis, a high-gain single-stage DC/DC converter with soft-switching capability is proposed for PV-driven magnetron applications. This thesis is divided into two main sections. The first part addresses the topology development and analysis of the proposed converter. The topology combines an integrated interleaved boost stage, a CLL resonant network and a voltage doubler rectifier for high voltage gain and low input current ripple. The converter maintains zero-voltage switching (ZVS) for all the switches and zero-current switching (ZCS) for all the diodes over a wide range of operation conditions. In-depth theoretical analysis and design considerations followed by simulation and experimental verification with a hardware prototype, are presented in this section. The second part of the thesis offers maximum power point tracking (MPPT) control schemes tailored for PV integration. Two duty-ratio-based approaches are utilized: a discrete logic-based Perturb and Observe (P&O) algorithm and a closed-loop proportional-integral (PI) controller. A small-signal modeling of the boost-integrated stage is addressed to ensure dynamic stability and accurate tracking under variable irradiance conditions. The converter’s performance and the effectiveness of the control strategies are validated through both simulation and experimental testing.

Acknowledgement

First, I would like to thank my supervisor, Dr. John Lam, most sincerely for the priceless guidance and support he has provided me. Besides being one of the most knowledgeable experts in the field, he is also a great mentor and individual. His relentless support over the past two years has acted as my greatest encouragement throughout the entire period.

I would also like to thank my committee members, Dr. Houshang Karimi and Dr. Paul G. O'Brien, for their patience, feedback, and constructive comments towards my thesis.

My gratitude would also extend to my lab mates and friends at the Power Electronics Laboratory for Sustainable Energy Research (PELSER) for all the support and all the moments we shared in the lab during these times. I would also like to thank my friends back home, Amir and Mohammad, for their strong friendship, even across these significant distances.

Very special thanks go to Rojin for all her love, support, and energy. She has grown to be a wonderful part of my life, and I truly appreciate having her by my side.

More than anyone, I owe my highest gratitude to my great parents and my brother, Amirreza, for their endless love and encouragement. It would be beyond words to express my gratitude for all of their efforts and support. It is due to my parents' hard work and sacrifice that I have grown up to the extent that I have today. And my little brother, I have never come across anyone more energetic than him. He has brought immense joy to our lives from the very moment he was born.

Table of Contents

List of Figures

List of Tables

Chapter 1 Introduction

1.1 Microwaves

Microwaves consist of electromagnetic waves whose frequencies usually range between 300 MHz and 300 GHz, between radio waves and infrared radiation in the spectrum of electromagnetism. Due to the capability of microwaves to penetrate through clouds, smoke, and thin rain, microwaves are vital in scientific as well as industrial applications. Some of the uses of microwaves include satellite communications, radar uses, medical diathermy, as well as microwave cooking. Due to their relatively short wavelengths, short, compact antennas can be designed as well as high-resolution imaging devices, and therefore, microwaves are used in commercial as well as military applications [1].

Reflecting this broad application, the global microwave-device market has grown enormously. According to a 2024 industry report, the microwave equipment market now exceeds $8 billion annually, driven by demand in markets such as aerospace, defense, medical imaging, and wireless infrastructure. Growth is expected to continue as industries invest in emerging technologies like 5G, autonomous vehicles, and advanced radar systems—all of which rely heavily on microwave-frequency components [2]. Figure 1.1 shows a market trend of the global microwave devices market report.

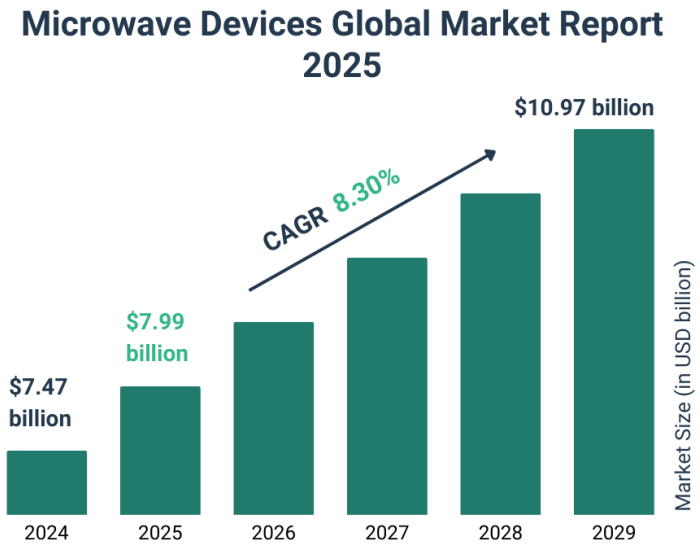

Figure 1.1- Global microwave devices market report 2025 [2]

1.2 Magnetron

A magnetron is a device responsible for generating high-frequency microwaves through the interaction of electrons emitted from a central cathode and a magnetic field. When a high DC voltage is applied between the cathode and anode, due to the magnetic field, the electrons radiate outward in a spiral motion, and as they interact with the resonant cavities in the anode, they induce microwave oscillation. This means that the magnetron generates microwave energy using only DC power and a magnetic field [3], [4]. The efficiency and power output of a magnetron depend on the design of these cavities, the strength of the magnetic field, and the applied voltage. Typical operating frequencies range from 900 MHz to 2.45 GHz, depending on the application [5][6]. A picture of a sample magnetron is shown in Figure 1.2.

The first magnetron can be traced back to early vacuum tube innovations in the 1920s; however, the development of the cavity magnetron in 1940 was revolutionary in the microwave landscape. This innovation integrated essential technologies into a small and compact device for

high-power microwave generation [7]. During World War II, the magnetron played a major role by making microwave radar practical. Several improvements were made during the war in the stability, efficiency, and weight of the device, which led to advancements for post-war applications. In the 1950s, a new generation of high-power magnetrons was developed, incorporating ceramic vacuum envelopes, advanced cathodes, and improved mechanical tuning [4].

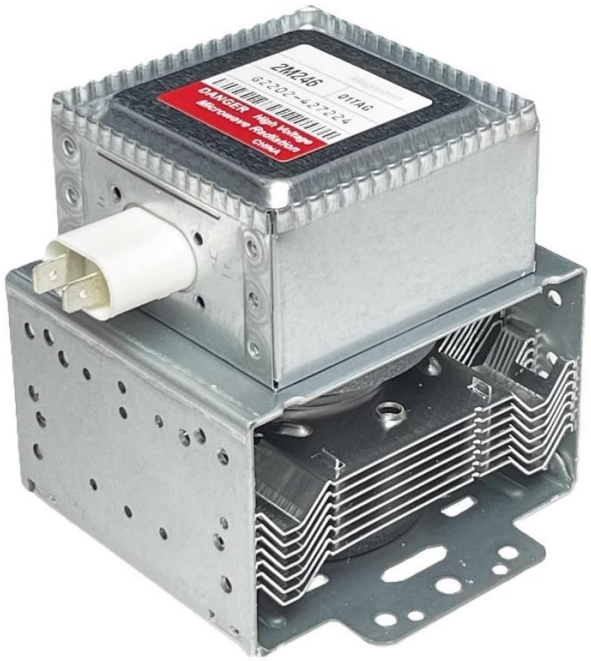

Figure 1.2 - A photo of a sample Magnetron[1]

1.2.1 Applications of Magnetron

Magnetrons are widely used across various industrial, scientific, medical, and consumer applications because they are efficient and compact sources of high-power microwaves. They play a pivotal role in systems that require robust, localized, and controlled electromagnetic radiation.

[1] https://www.amazon.ca/2M246-01TAG-Microwave-Compatible-6324W1A001L-6324W1A001B/dp/B09DPJ6C9X

Microwave heating

One of the most common applications of magnetrons is microwave heating in domestic and industrial systems. More than 5 million domestic microwave ovens are produced annually. This significant market capacity is due to their cost-effectiveness, high reliability, and minimal maintenance [2]. In industry, the generated microwaves are used to heat materials through dielectric loss. There are many uses for this technology, including heating metallic powder, rubber vulcanization, drying food, treating wood, and processing textiles and paper products. In addition to volumetric heating (uniform internal temperatures), microwave systems are more energy efficient, environmentally friendly, and compact [8], [9].

Radar and Navigation Systems

As mentioned before, since the development of cavity magnetrons during World War II, this device has been a key component in radar technology, which has helped in high-frequency, high-resolution detection. They continue to be used in many modern applications that require radar and navigation systems, such as marine and weather radar, airport surveillance, and military tracking. Their simple design, low cost, pulsed high-power output, and robustness in harsh environments are the main characteristics that are still desirable. Radar magnetrons typically operate in the X-band (8–12 GHz) or S-band (2–4 GHz), with minimal interference and enhanced resolution [4], [10].

Plasma Generation

Another magnetron application is materials processing by microwave-induced plasma. This includes semiconductor manufacturing, surface treatment, thin film deposition, etching, and cleaning. These systems generate plasma through the introduction of microwave energy into a gas such as argon, resulting in ionization. Microwave plasmas are favored because they have high uniformity, low ion energy (which minimizes damage to sensitive substrates), and the ability to operate efficiently at low pressures [10], [12].

Medical Applications

Magnetrons are at the heart of many medical devices that utilize electromagnetic energy, including microwave ablation for tumor destruction by thermal coagulation, diathermy for pain relief and improved circulation by deep tissue heating, and hyperthermia treatments that warm cancer cells to enhance the effectiveness of radiation or chemotherapy. The precision with which microwave energy can concentrate heat in the desired tissues while sparing nearby healthy tissues makes it especially well-suited to these applications [6].

Soot Pollution Reduction

One of the emerging applications of microwave technology, specifically magnetron-based systems, is soot emission reduction from combustion. Magnetrons improve soot particle thermal oxidation by delivering microwave energy into combustion zones, resulting in improvements in post-combustion cleanup in industrial burners and engines. This method enhances the flame temperature uniformity and in-situ carbon particulate breakdown, resulting in lower soot concentration in exhaust gases, lower diesel particulate filter (DPF) filter loading, and potential

CO and NO_x emission reductions. As a non-invasive and energy-saving technology, it offers an effective emissions control solution under more stringent environmental requirements [13].

1.2.2 Magnetron Power Supply

As mentioned earlier, magnetrons require a high DC voltage to function. Because of the nonlinear characteristics and sensitivity to voltage ripple of magnetrons, this DC voltage needs to be precisely regulated to ensure reliable operation. Over the years, power supplies for magnetrons have evolved from bulky transformer-rectifier designs to compact, efficient power electronics converters.

Previously, magnetron power supplies used line-frequency (50/60 Hz) transformer-rectifier technology. A transformer boosted the AC mains voltage, and the voltage was rectified and filtered to produce high-voltage DC [8]. These circuits usually consisted of a diode bridge rectifier, a smoothing capacitor bank, and occasionally a choke to reduce ripple. While they were simple, they were large, inefficient, and not very dynamic. The large size of the low-frequency transformer and voltage regulation methods added to the system cost, size, and slowness. Furthermore, magnetrons' highly nonlinear I–V characteristics show that this device operates within a narrow voltage range, with small deviations in anode voltage causing drastic shifts in anode current, affecting the oscillation performance [14]. A small voltage change may cause inefficient microwave output, frequency instability, or internal arcing. Traditional power supplies lacked rapid feedback control and thus were prone to performance degradation and magnetron failure with time.

These limitations of conventional magnetron power supplies have resulted in the popularity of Switch-Mode Power Supplies (SMPS). In recent years, power electronics has developed very rapidly, mainly due to two causes. First, the advent of fast semiconductor switches that have the ability to switch very quickly and provide high power. Second, the development of real-time computer controllers capable of running complex control algorithms [15]. These two advancements have enabled:

- High efficiency
- Significant size and weight reduction due to high-frequency operation
- Better dynamic regulation and control
- Compatibility with soft-switching techniques for reduced losses and EMI

To achieve a high-performance and low-cost high-voltage DC power supply, various techniques have been researched in recent years. Among them, high-voltage DC/DC converters allow for compactness through the use of silicon-carbide (SiC) devices, low-on-resistance MOS-gated power devices, and high-frequency core materials [16]- [19].

1.3 DC/DC Converters for Magnetron Power Supplies

1.3.1 Basic Step-up Converter Topologies

This section provides a discussion on the most commonly used basic step-up power electronics converters [20].

Boost Converter

The boost converter is the most fundamental and widely used topology for stepping up DC voltage. Figure 1.3 (a) shows the conventional boost converter topology. The converter includes an inductor, a semiconductor switch (usually a MOSFET), a diode, and an output capacitor. It increases voltage by storing energy in the inductor and transferring it to the output capacitor. In continuous conduction mode (CCM), the inductor current never falls to zero, and the ideal relationship between input and output voltages is given by $V_o = \frac{V_d}{1-d}$, where V_o is the output voltage, V_d is the input voltage, and d is the duty cycle. The boost converter is widely used in low to moderate power applications due to its simplicity and effectiveness; however, there are some limitations. For large voltage gains, boost converter requires extremely high duty cycles for large gains, which is undesirable due to high stress on the inductor and switch. Also, due to high switching and conduction losses, the converter can show poor efficiency. Besides, it cannot provide electrical isolation between the input and output. As a result, traditional boost converters are rarely used alone in magnetron systems but may appear in multi-stage or pre-regulation circuits [21].

Flyback Converter

When galvanic isolation between the input and output is required in a step-up application, the flyback converter is often the topology of choice. The flyback topology is shown in Figure 1.3 (b). The converter includes a transformer, a semiconductor switch (usually a MOSFET), a diode, and an output capacitor. The flyback stores energy in the magnetic core of a transformer rather than in an inductor, which was the case in a boost converter. The output voltage of a flyback converter in continuous conduction mode is given by $V_o = \left(\frac{N_s}{N_p}\right).\frac{d}{1-d}\ .V_d$, where N_s and N_p are

the number of turns in the secondary and primary windings, respectively. Depending on the turns ratio of the transformer, it can allow for both step-down and step-up capability. One of the strengths of the flyback converter is that it can generate multiple output voltages with multiple secondary windings. However, it suffers from heavy output voltage ripple and poor regulation under heavy loads unless a sophisticated feedback mechanism is employed. The design of the transformer is critical because it serves as the isolation and energy storage element at the same time. Moreover, the transformer must be designed in such a way that it doesn't saturate and that leakage inductance is minimized; otherwise, voltage spikes would occur and snubber circuits would be required for protecting the switching device.

Push-Pull Converter

For the medium-power cases where isolation and a better utilization of the transformer are required, the push-pull converter can be a popular topology, as presented in Figure 1.3 (c). It uses two switches alternatively for driving a center-tapped transformer primary winding. Symmetrical operation should be prioritized to ensure both halves of the transformer are utilized throughout every switching period, which results in increased magnetic efficiency and power density. The output voltage of a push-pull converter is given by $V_o = 2(\frac{N_s}{N_p})dV_d$, assuming 50% duty cycle for both switches and ideal conditions. One challenge with this converter is to prevent the transformer core from saturating by maintaining close synchronization between the two switches. Also, voltage imbalance and shoot-through conditions, which can lead to circuit failure, should also be avoided.

Half-Bridge and Full-Bridge Converters

Half-bridge and full-bridge converters are shown in Figure 1.3 (d) and (e). The half-bridge converter uses two switches, a capacitive voltage divider, and a transformer. On the other hand, the full-bridge converter employs four switches to accomplish the same with improved voltage utilization. In the half-bridge topology, the effective input voltage across the transformer is half the bus voltage, and the voltage gain is $V_o = \left(\frac{N_s}{N_p}\right) d \frac{V_d}{2}$. The topology has fewer switches but requires bulky capacitors for voltage balancing and is also more sensitive to bus imbalance. The full-bridge converter uses four switches and applies the whole input voltage across the transformer, leading to a higher voltage gain of $V_o = \left(\frac{N_s}{N_p}\right) dV_d$. This topology is preferred for higher power levels than the half-bridge. While half-bridge and full-bridge converters have improved efficiency and voltage conversion capability, they both require complex control circuits, including dead-time insertion, gate drive isolation, and current-mode or voltage-mode feedback.

Although some previous magnetron power supplies employ these basic converters or newer topologies derived from them, most of them lack the following key requirements.

High Voltage Gain**:** Typical domestic and industrial magnetrons require 2–14kV input voltage to operate. This means that the power supply must provide this range of voltage, with input voltages ranging from 20V to 400V. This must be achieved without extreme stress on switches and inductors, and with proper isolation [22].

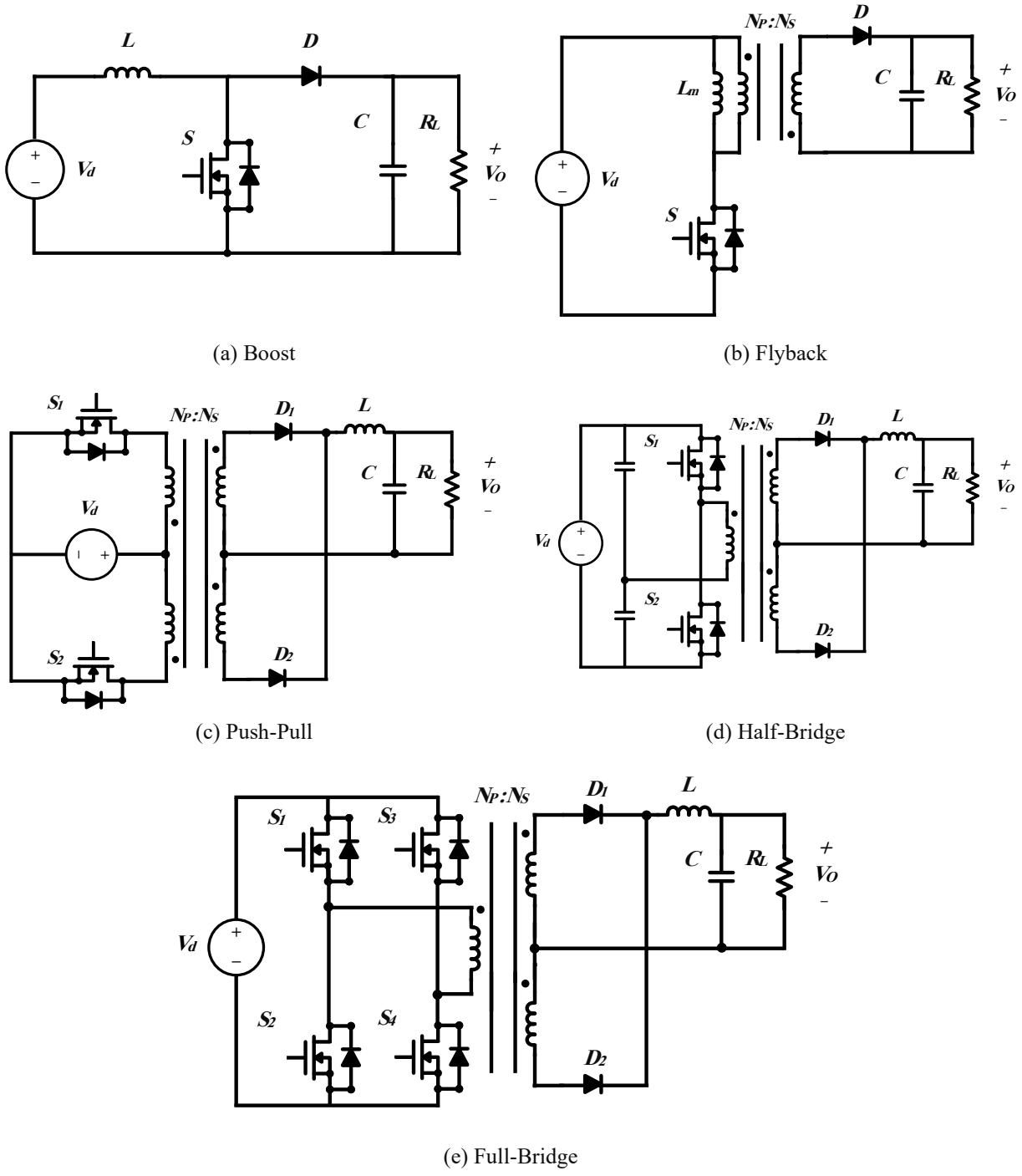

(a) Boost

(b) Flyback

(c) Push-Pull

(d) Half-Bridge

(e) Full-Bridge

Figure 1.3- Basic step-up converter topologies (a) Boost, (b) Flyback, (c) Push-Pull, (d) Half-Bridge, (e) Full-Bridge

High Efficiency: Operations such as industrial heating and plasma generation, which are among the main magnetron applications, are very energy-intensive. Even a few percentage points of efficiency loss translates to substantial energy waste and heat dissipation [23]

Soft Switching: converters with soft-switching operation (Zero-Voltage Switching (ZVS) for MOSFETs and Zero-Current Switching (ZCS) for diodes) reduce switching losses, minimize noise, and alleviate electrical stress [24]. Also, soft-switching allows operation at higher frequencies, resulting in smaller magnetic component size. These characteristics are required for a magnetron power supply, which is prone to arcing. This is a risk that is intensified when hard-switching converters are used due to their high stresses, increased electromagnetic interference (EMI), and peak voltage overshoots.

Current Ripple and Noise Suppression: The stability of magnetron operation can be impacted by noise and current ripple. Variations in the microwave output caused by high power supply ripple can impact the operation of applications such as microwave heating or plasma processing [25].

Compactness and Thermal Management: High power density is a requirement for modern converter topologies, especially in systems mounted in small spaces [24]. High switching frequency reduces the component size but also causes thermal concerns. Thus, the design of the power supply must encompass thermal considerations as well.

1.3.2 Resonant Converters

Considering the magnetron power supply requirements, utilizing resonant converters is one of the most popular methods due to their low loss and soft-switching capability. Figure 1.4 shows a typical DC/DC resonant converter. First, the DC voltage is fed to the inverter stage (switch network). Then, this network generates a square-wave voltage at a controllable frequency and duty ratio to the resonant tank. The resonant circuit, consisting of capacitors, inductors and sometimes a transformer, has the effect of filtering the higher harmonics. The resonant tank enables the soft-switching condition of the switch network and stepping up or down of the input voltage. The voltage gain is usually controlled by frequency. In the next step, the output of the resonant tank is fed to a rectifier and a low-pass filter to convert the AC voltage to DC. In this step, voltage multipliers can be exploited to provide an additional stepping up in the voltage, as well as rectifying it [26]. Different topologies can be used, such as voltage doublers, voltage quadruplers, and voltage multiplier topologies [27]-[30].

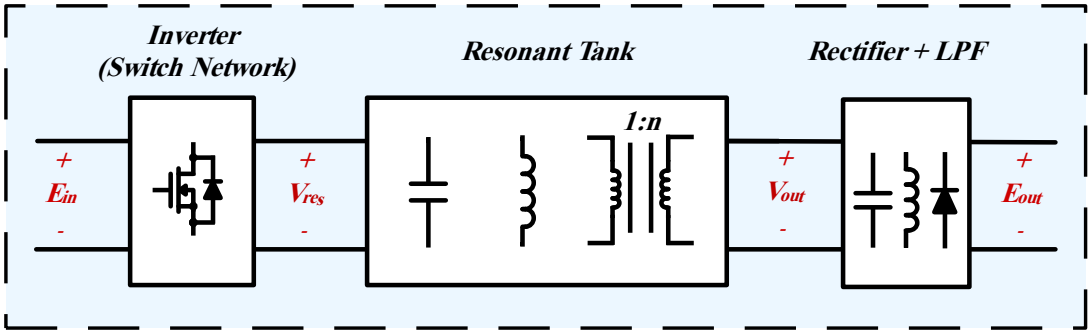

Figure 1.4 - Typical structure of a DC/DC resonant converter

Two basic and pivotal resonant circuit topologies are series resonant and parallel resonant, as shown in Figure 1.5(a) and 1.5(b) [31], [32]. A series resonant circuit is used for step-down applications, since its maximum voltage gain is only one. A key advantage of the series resonant

converter is that the series capacitor naturally functions as a DC-blocking element. Also, the current of the power devices decreases as the load decreases. However, the main disadvantage of this topology is that the output voltage cannot be regulated under light loads, meaning that the voltage gain is almost constant over different operating frequencies in this load condition. Figure 1.6 (a) shows the voltage gain of this topology as a function of the relative angular frequency $\omega_r = \frac{\omega_s}{\omega_0}$, where ω_s and ω_o are the switching and resonant angular frequencies. Also, another drawback of this circuit is the high current ripple of the output capacitor. Compared to the series resonant circuit, the parallel resonant topology is used when stepping up in voltage is required. The output voltage can be easily regulated under different load conditions over a small operating frequency range. The voltage gain characteristic is shown in Figure 1.6(b). However, this circuit has a low light load efficiency since the circulating current remains almost constant over different load conditions. This current also increases as the input voltage increases.

To overcome the drawbacks of the classic series/parallel resonant circuits, one or two elements (capacitors and/or inductors) can be added to them to form new configurations [30]. Among them, the LCC, LLC, and CLL resonant topologies are the most popular ones, as shown in Figure 1.5(c)-(e) [33] [34]. The LCC circuit is a combination of the series and the parallel topology, designed to eliminate the drawbacks of both and take advantage of the best characteristics [31]. However, this circuit suffers from the main disadvantage of the parallel resonant topology, which is a high circulating current leading to a drop in efficiency. As a result, LLC and CLL configurations have recently received more attention in the literature. In both topologies, the magnetizing inductor of a transformer can be used as the parallel inductor (L_P), resulting in isolation between the two sides and an additional voltage step. The main difference between the two is that, in the CLL configuration, the series inductor is positioned after the other

two components, allowing it to be placed on the secondary side of the transformer (if a transformer is used). This placement helps reduce overall system size and cost. Figure 1.6(c) and 1.6(d) show the voltage gain of these three configurations.

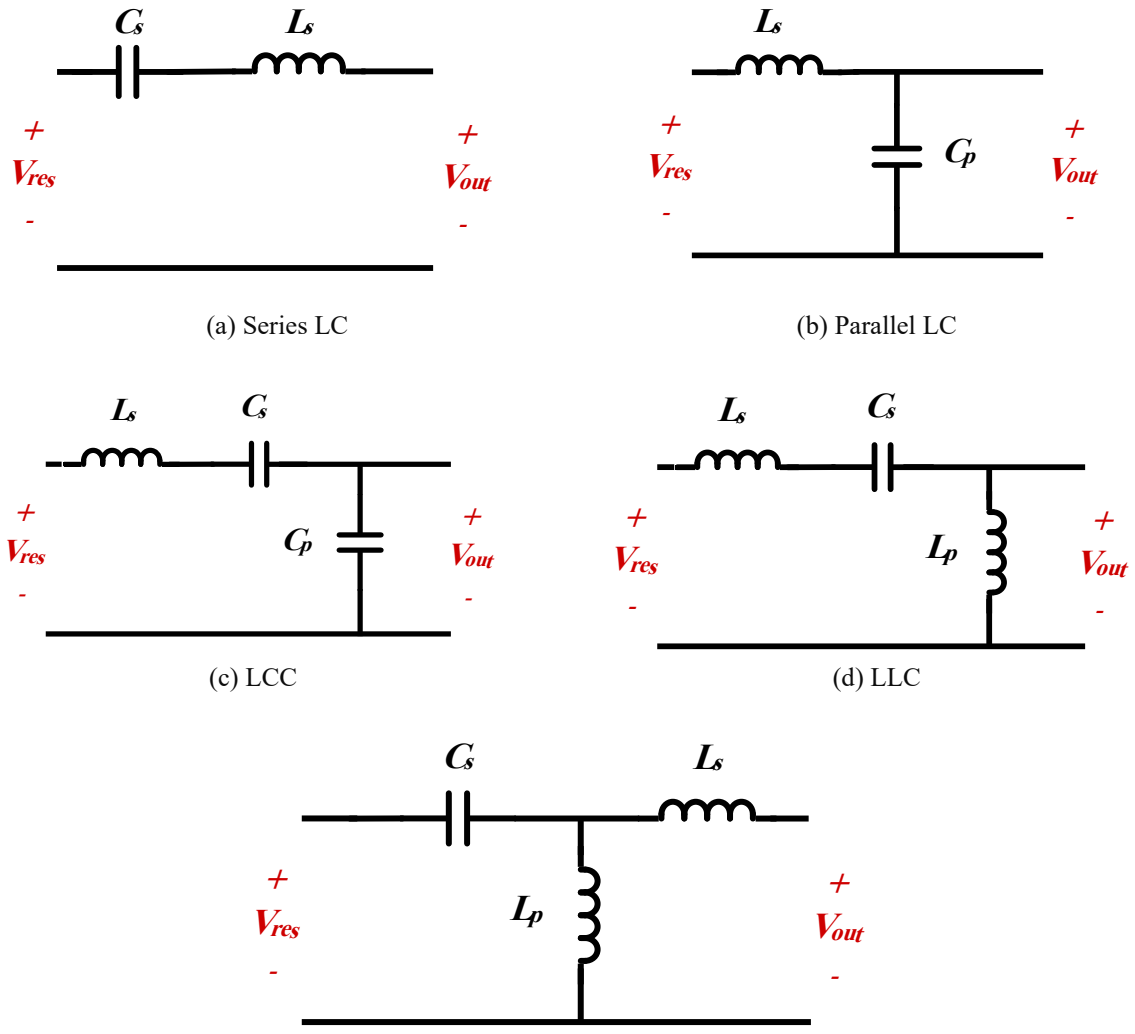

Figure 1.5 - Different resonant topologies (a) Series LC, (b) Parallel LC, (c) LCC, (d) LLC, and (e) CLL

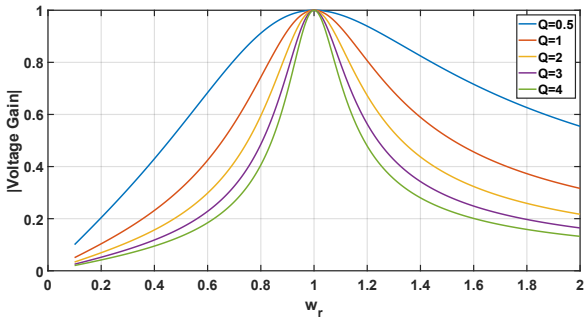

(a) Series LC

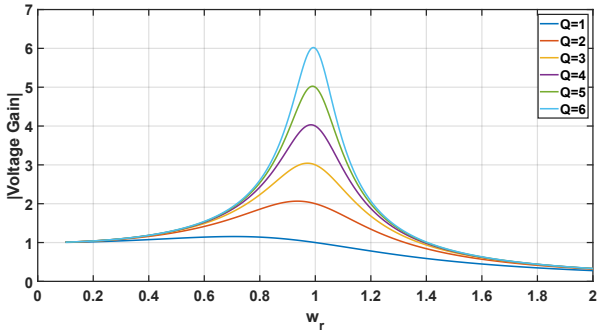

(b) Parallel LC

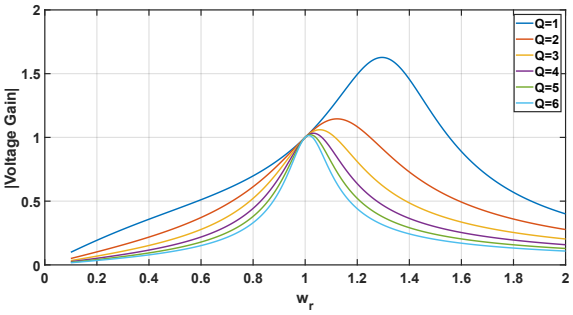

(c) LCC

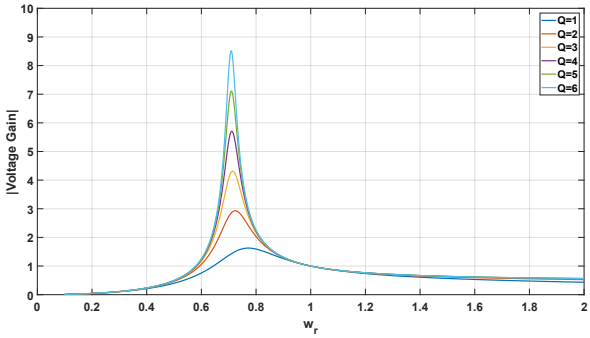

(d) LLC

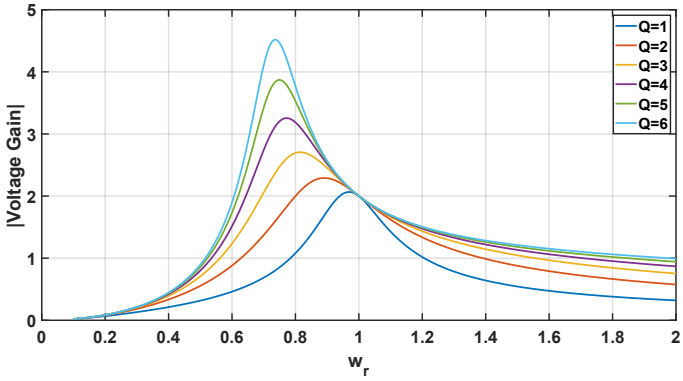

(e) CLL

Figure 1.6 - Voltage gain characteristic (a) Series LC, (b) Parallel LC, (c) LCC, (d) LLC, and (e) CLL

Various topologies exploiting resonant converters have been introduced in the literature. [35] introduces a sophisticated LLC-based topology designed to support magnetrons operating across a wide range of output voltages. It uses two input-series-connected full-bridge inverters along with six LLC resonant networks and reconfigurable voltage multipliers. The system

maintains soft-switching and high efficiency across a wide voltage range. In [22], the optimization of a high-voltage converter for industrial magnetrons using an input-parallel, output-serial (IPOS) LLC configuration is addressed. The paper tackles challenges posed by parasitic capacitances in high-isolation transformers by modeling them accurately and incorporating them into the design process. [36] presents a pulse width modulation controlled series resonant converter (PWM-SRC) intended for magnetron use. The converter operates in Mode 3, which enables a preferred compromise between zero-voltage switching (ZVS) and zero-current switching (ZCS) for enhancing switching efficiency and minimizing losses. The converter comprises a parallel-input-series-output (PISO) transformer configuration for meeting insulation specifications and reducing secondary voltage stress. The authors propose a hybrid dual-output resonant converter with CL and LLC networks combined in [37]. The CL resonant tank is employed to generate the high voltage required by the magnetron, and the LLC tank to supply the filament. Both networks employ individual control so that all semiconductor switches operate under ZVS conditions and diodes under ZCS. A unique AC-input converter design that integrates power factor correction (PFC) and a dual-output resonant stage is introduced in [38]. The converter uses a bridgeless PFC front-end operating in discontinuous conduction mode, which significantly reduces conduction losses. The resonant stage employs a CL network for the high-voltage anode output and an LLC network for the filament. By sharing switches between stages, the converter minimizes component count while maintaining high performance. [39] tackles the challenge of maintaining high efficiency across wide output voltage ranges using an LCC resonant converter. The authors introduce an Optimal Control Coordinate Trajectory (OCCT) approach, which allows adaptive phase-shift and frequency modulation while reducing control complexity. In [40], ultra-low output voltage ripple and precision in high-voltage DC power supplies are stressed using a three-phase LCC resonant

converter. The three-phase approach enables multiphase operation, which radically improves performance at full and light loads.

1.4 Photovoltaic Integration

The energy demand has been growing rapidly in the past few decades. Consequently, energy and the environment have been major concerns in the modern world [41]. This has led to more focus on renewable energy sources, including photovoltaic (PV), wind, hydro-power, bio-power, and geothermal [42].

Photovoltaics (PV) is at the center of this revolution. Installed PV capacity has grown from the kW scale to MW and now GW over the past 20 years, and it is likely that the 1 TW of installed global capacity milestone will be reached soon [43]. This is mainly due to declining costs. This decrease has been induced by 1) an increasing efficiency of solar cells, 2) technology advances in manufacturing, and 3) economies of scale [44], [15]. PV panels can be constructed using various types of cells, such as monocrystalline, polycrystalline, and thin-film PV cells. A PV module consists of several individual PV cells in series. A series connection of PV modules forms a PV string, and a parallel connection of PV strings forms PV arrays [45].

PV arrays exhibit non-linear electrical *I-V* and *P-V* characteristics, as shown in Figure 1.7. These characteristics depend on the environmental conditions. The point at which the *P-V* curve reaches its maximum value is known as the Maximum Power Point (MPP), which changes under different atmospheric conditions such as solar irradiance and temperature. Therefore, a controller is required to lead the PV panel to its maximum point, a process known as Maximum Power Point

Tracking (MPPT). Additionally, the harvested energy from the PV panel is not directly usable by the load or the connected DC grid due to the voltage incompatibility between PV panels and the load. The PV panel output voltage is low (30-40 V) compared to what a load or MVDC-grid would require (up to hundreds of kV) [46]-[48].

Thus, a controllable power interface (usually a DC/DC converter) is connected between the PV source and the load to achieve Maximum Power Point Tracking (MPPT) and voltage step-up (see Figure 1.8). The principle behind MPPT is the impedance match between the PV source and the load. MPPT can be applied by controlling the parameters, such as the duty ratio or the operating frequency of the DC/DC converter, to adjust the equivalent load resistance to match the MPP.

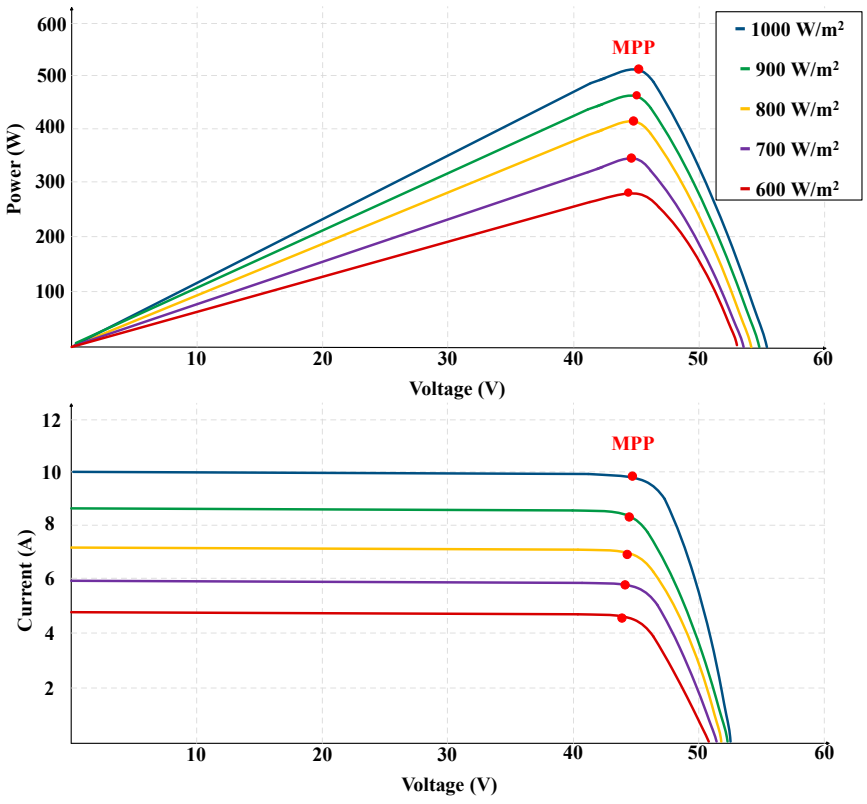

Figure 1.7 - The P-V and I-V curves of a sample PV module

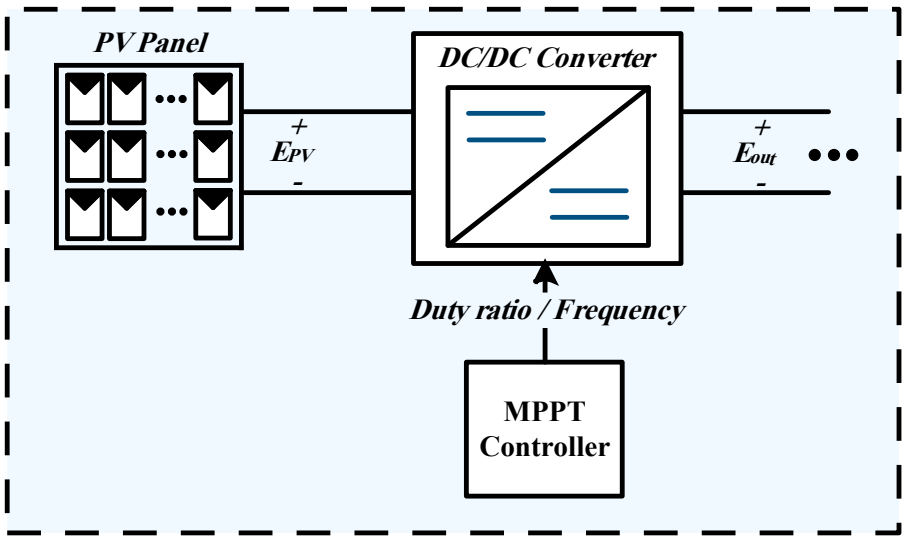

Figure 1.8 - PV panel with controllable power interface

1.4.1 Maximum Power Point Tracking (MPPT) Techniques

This section will go through some of the most common MPPT methods used in the literature [49]-[57][58].

1.4.1.1 Perturb and Observe (P&O)

The P&O algorithm, also known as the hill-climbing method, operates by iteratively perturbing the solar panel voltage through changes in duty ratio or operating frequency of the DC/DC converter. This results in a change (increase or decrease) in the operating power of the PV source. If a small perturbation in the voltage leads to an increase in power, the algorithm continues in the same direction; however, if the power decreases, the perturbation direction is reversed. The direction of voltage perturbation is determined by (1.1). This procedure continues until the system stabilizes around the MPP.

$$V_{ref} = \begin{cases} V + V_{step} & , \quad \frac{\Delta P}{\Delta V} > 0 \\ V - V_{step} & , \quad \frac{\Delta P}{\Delta V} < 0 \end{cases} \tag{1.1}$$

The possible outcomes of a perturbation are summarized in Table 1.1.

The main advantage of P&O is its simplicity, as this method does not require complex mathematical functions to determine whether the system is at the MPP. However, this simplicity also results in the system oscillating around the MPP. This technique still achieves high extraction efficiency (>90%).

Table 1.1- P&O method possible outcomes

Voltage Perturbation	Change in Power	Interpretation on P-V Curve	Next Perturbation
Positive (+)	Positive (+)	Left of MPP	Continue (+)
Positive (+)	Negative (-)	Right of MPP	Reverse (-)
Negative (-)	Positive (+)	Right of MPP	Continue (-)
Negative (-)	Negative (-)	Left of MPP	Reverse (+)

1.4.1.2 Incremental Conductance (INC)

Incremental Conductance (INC) is another well-known and commonly used MPPT method. The principles are very similar to the P&O technique, except that in this method, the voltage perturbation direction is based on the change in PV current with respect to the change in PV voltage (1.2). The direction of voltage perturbation for the INC method is determined by (1.3).

$$\frac{\Delta P}{\Delta V} = \frac{\Delta(IV)}{\Delta V} = I + V\frac{\Delta I}{\Delta V} \tag{1.2}$$

$$V_{ref} = \begin{cases} V + V_{step} & , \quad \frac{\Delta I}{\Delta V} > -\frac{I}{V} \\ V + 0 & , \quad \frac{\Delta I}{\Delta V} = -\frac{I}{V} \\ V - V_{step} & , \quad \frac{\Delta I}{\Delta V} < -\frac{I}{V} \end{cases} \tag{1.3}$$

The results indicate that INC can detect if the system is on the MPP, which is better than P&O. However, it should be noted that this condition is unlikely to be satisfied in practice due to digital resolution. INC utilizes more complex mathematical formulas than P&O, which reduces its tracking speed.

1.4.1.3 Curve Fitting

The P-V curve can be expressed as a third-order polynomial function as (1.4), which allows the voltage needed to operate at the MPP to be calculated. The coefficients a_0, a_1, a_2 , and a_3 differ with every PV panel and need to be obtained by monitoring the input voltage and power. With the parameters a_0, a_1, and a_2 determined, the voltage required to work at the MPP can be computed by (1.5) and (1.6). Because this method estimates the P-V curve, the resulting voltage at MPP is also an estimate, with the inference that the system will typically be operating close but not at the MPP. The sampling requirement also affects the operation rate, which can be troublesome under conditions of rapidly changing MPP [59].

$$P = a_0 v^3 + a_1 v^2 + a_2 v + a_3 \tag{1.4}$$

$$\frac{dP}{dv} = 3a_0 v^2 + 2a_1 v + a_2 \tag{1.5}$$

$$v_{mpp} = \frac{-a_1 \pm \sqrt{{a_1}^2 - 4a_0 a_2}}{2a_0} \tag{1.6}$$

1.4.1.4 Intelligent MPPT Algorithms

Several advanced and intelligent MPPT algorithms have been developed in literature, such as Fuzzy logic [60]-[63], Artificial Neural Network (ANN) [64]-[67], etc., which are beyond the scope of this thesis.

1.4.2 Energy Storage System

The energy provided by photovoltaic (PV) systems depends on environmental conditions, such as solar irradiance, which is always changing due to shading, clouds and nighttime. An energy storage system (ESS) is usually utilized alongside PV arrays to ensure continuous operation. Figure 1.9 shows a typical PV system with an energy storage system (ESS) unit. ESS compensates for the solar energy by supplying power during insufficient irradiance and stores energy when generation is higher than demand via a bidirectional DC/DC converter.

Various ESS configurations have been developed to store electrical energy, including the technologies around high power storage (HPS) and high energy storage (HES) methods [68]. These

systems also require control techniques such as storage management systems and charging/discharging strategies to ensure reliable operation. However, the design and control of ESSs are not addressed in this research, and the focus is on integrating only PV panels with the designed power supply.

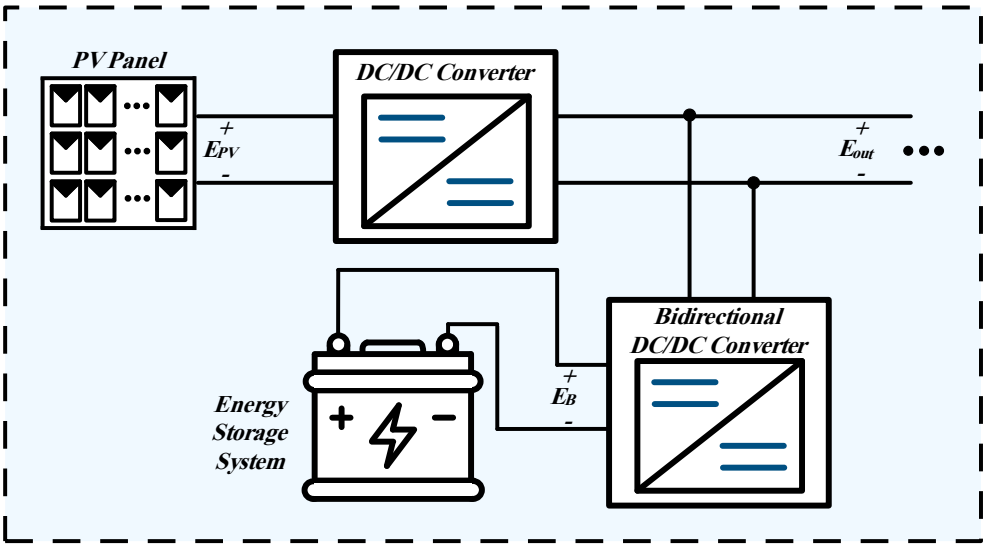

Figure 1.9 – Typical configuration of a PV panel with an energy storage system (ESS)

1.5 Research Motivation

Magnetrons, which generate high-power microwave energy, are pivotal devices in a wide range of industrial, medical, and scientific applications. They require compact, efficient, stable high-voltage DC power supplies with low ripple and electromagnetic interference (EMI) to operate. Traditional power supplies based on transformer-rectifier technology lack the requirements in terms of size, dynamic performance, and efficiency. Recent advancements in power electronics lead to designing high-level DC/DC converters that meet the demanding requirements of magnetron systems. Among them, resonant converters are promising due to their intrinsic soft-switching nature, high efficiency, and adaptability to high-frequency, high-voltage

operations. Furthermore, since the energy demand has been growing rapidly in the past few decades, renewable energy sources have been getting a lot of attention. Integrating these sources, such as photovoltaics (PV), needs additional design considerations. PV systems offer a clean and sustainable energy source, but they require advanced power electronic interfaces to ensure maximum power extraction. The motivation behind this research is to develop and optimize a high-efficiency, high-voltage-gain DC/DC converter integrated with PV energy for magnetron power supplies.

1.6 Thesis Objectives and Outline

Many magnetron power supplies have been introduced in the literature. These topologies often depend on a large quantity of circuit components, such as semiconductor switches and heavy electrolytic capacitors that add to system cost, size, and complexity. The majority of the designs still require large duty ratios to achieve the desired voltage gain, leading to efficiency and control losses. The absence of soft-switching techniques leads to high switching losses and high electromagnetic interference (EMI). The objective of this thesis is to develop a high step-up soft-switching DC-DC interleaved boost integrated CLL resonant converter for magnetron applications. The converter will utilize renewable energy sources by using photovoltaic energy as the input source while providing soft-switching over a wide range. Also, some duty-ratio-based MPPT control methods will be introduced to extract the maximum power from the PV source. The outline of this thesis is as follows:

Chapter 1 provided an introduction to the magnetron technology, the history of its development, its operating principles and a wide range of applications. Then, the need for high-

voltage DC power supplies and the challenges associated with the design procedure were discussed. Conventional and advanced DC/DC converter topologies, with a focus on resonant converters due to their high efficiency and soft-switching characteristics, were reviewed. Furthermore, the integration of photovoltaic systems with magnetron power supplies and MPPT techniques was addressed. Finally, the research motivation and the outline of the thesis were highlighted.

In Chapter 2, first, a high step-up soft-switching DC-DC converter operation will be discussed. The proposed topology integrates an interleaved boost converter with a CLL resonant tank, offering high voltage gain, soft-switching operation, and reduced current ripple. Then, the operating principles and theoretical analysis of the converter will be discussed considering parameters such as operating frequency, resonant frequency and quality factor. This chapter also includes simulation results validating the converter's characteristics as well as a proof-of-concept prototype providing experimental results to confirm the performance of the proposed converter.

Chapter 3 will focus on integrating the proposed high-gain converter with photovoltaic (PV) sources by implementing MPPT control schemes. Two duty ratio control methods based on the Perturb and Observe (P&O) algorithm will be presented: a discrete logic-based method and a PI-based closed-loop control. To support the PI-based approach, a small-signal model of the boost-integrated stage will be derived and analyzed to design a stable and responsive controller. Simulation and experimental results will demonstrate the converter's ability to track the maximum power point accurately under varying light conditions, while maintaining high voltage gain and soft-switching behavior.

In Chapter 4, the thesis will be concluded, and the possible future work related to the proposed converter will be discussed.

Chapter 2 Proposed High-Gain Single-Stage Soft-Switched Converter

As discussed in Chapter 1, considering the wide application of microwave energy, most industries require a high-voltage DC power supply to operate magnetron devices. This chapter will focus on developing a modular photovoltaic interleaved boost integrated CLL resonant converter for magnetron applications. The overall diagram of the proposed system is shown in Figure 2.1.

First, a high step-up soft-switching DC-DC converter will be introduced. Resonant topologies are a popular choice in PV energy systems, and by utilizing a resonant tank, the proposed converter achieves high voltage gain with high operating frequency, resulting in improved efficiency while allowing for smaller component size and higher power density. Then, the operating principles and theoretical analysis of the converter will be discussed. Finally, simulation and experimental results will be provided to confirm the performance of the proposed converter.

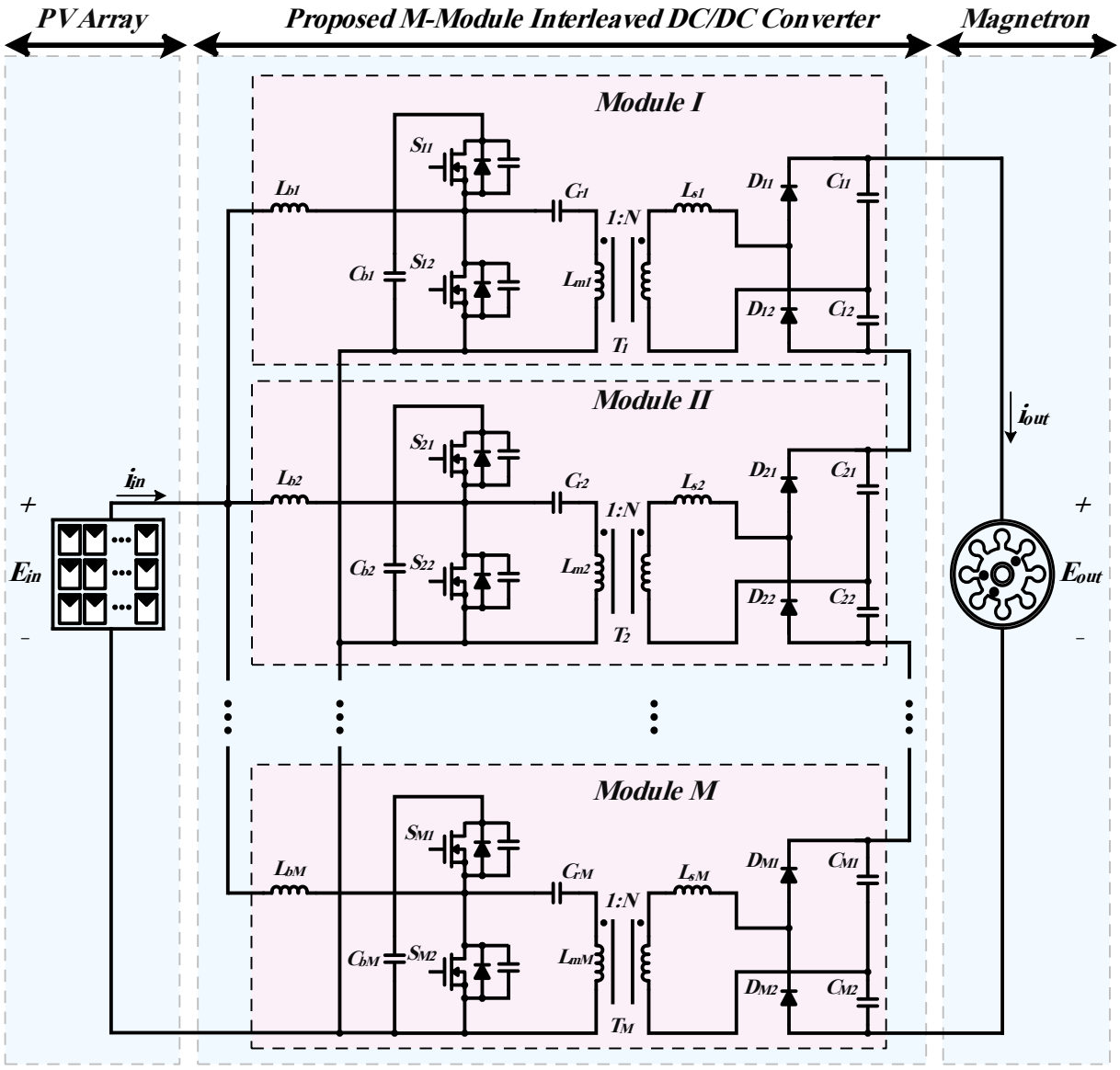

Figure 2.1- Overall diagram of the proposed M-module system

2.1 Proposed Converter Topology

For illustration, the proposed converter utilizing only two interleaved modules is presented in Figure 2.2. Each module exploits a CLL resonant converter and a single-stage boost converter combined with a voltage doubler to achieve high step-up gain. The two interleaved modules operate 180° out of phase with each other, and because they distribute the input current, the current

rating of the switching device can be decreased. Moreover, the interleaved structure helps reduce the input current ripple, output voltage ripple, and size of the passive components.

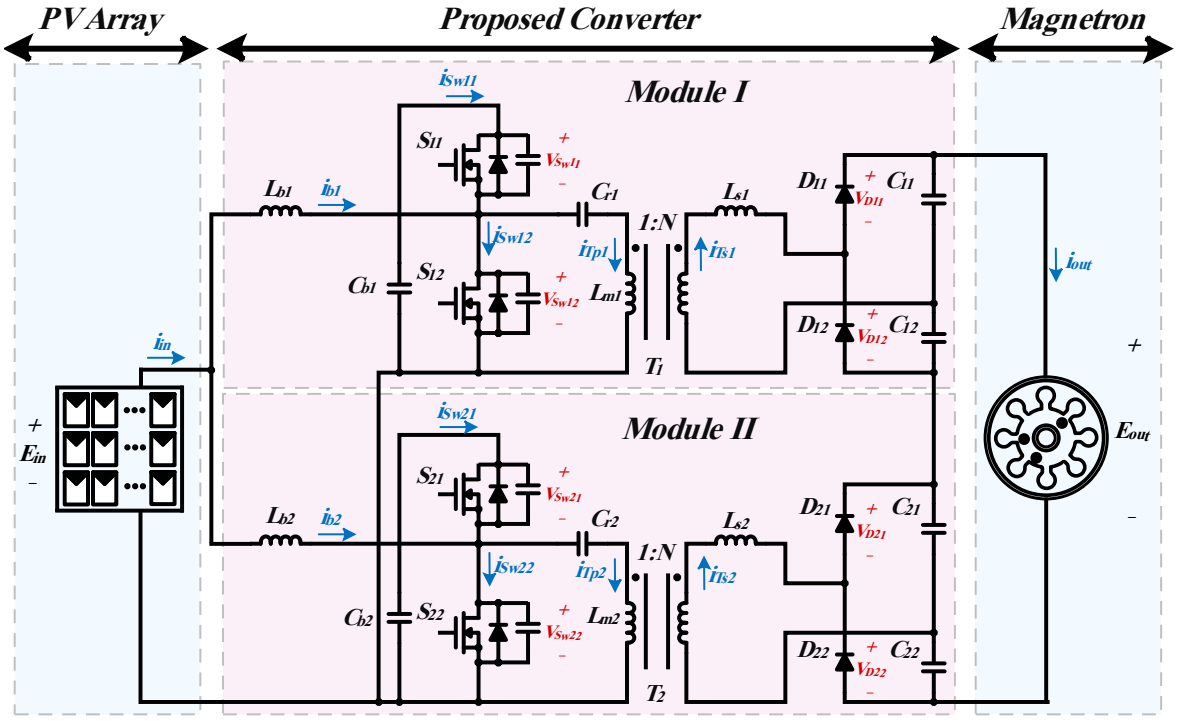

Figure 2.2- Proposed 2-module high-gain DC/DC CLL converter with integrated interleaved boost stage

Each module consists of

- An integrated boost stage
- A half-bridge inverter
- A CLL resonant circuit network
- A voltage doubler

The boost stage and the half-bridge stage are combined into a single-stage converter based on the methods presented in [68][69]. As a result, the converter operates with just two switches with a complementary duty ratio, which are responsible for boosting the PV voltage and providing an AC voltage waveform for the CLL resonant stage. A transformer with a turn ratio of *1:N* is used

in the CLL resonant stage, which (i) provides isolation between the primary and secondary sides, (ii) allows additional step-up voltage gain, and (iii) integrates the magnetizing and leakage inductor of the transformer with the series capacitor and inductor to form the CLL resonant tank.

2.1.1 Converter Operating Principles

In this section, the in-depth operating principles of the converter are analyzed. To simplify the steady-state analysis of the proposed converter, only one module is considered (See Figure 2.3). It is assumed that:

- The secondary side current of the transformer is zero only during the dead time.
- The duty ratio of switch S_2 is denoted by d

Figure 2.4 shows the operating waveforms of the converter, and the key operating stages are illustrated in Figure 2.5. As shown in Figure 2.3, the following equation holds for every time interval. Since the converter is always in CCM operation, i_b remains positive.

$$i_{sw1} + i_b = i_{sw2} + i_r \tag{2.1}$$

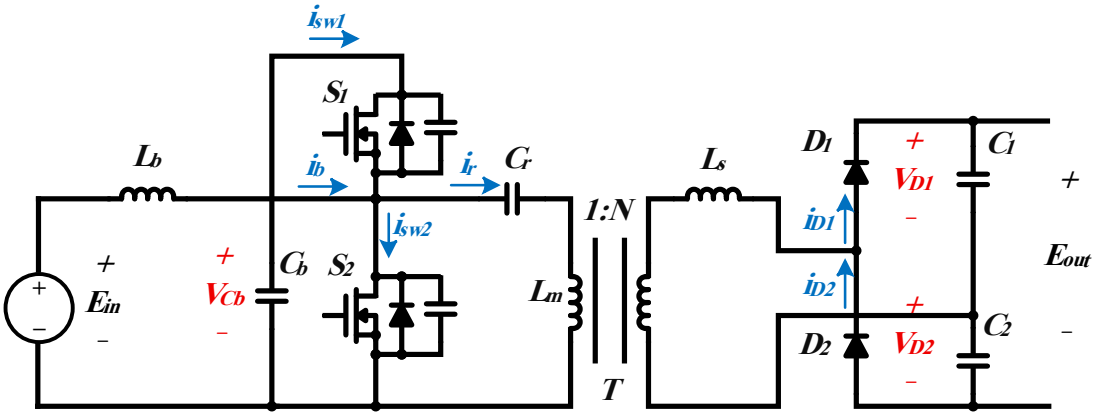

Figure 2.3- Circuit schematic for one module

[$t_0 < t < t_1$]: At time t_0, the gate signal V_{gs1} is applied to the switch S_1, and the gate signal of S_2 is removed. Since the resonant current is negative at the moment, i_{sw1} is also negative and flows through the anti-parallel diode of S_1. In this interval, the boost inductor is discharging into the DC-link capacitor, hence i_b decreases, while both i_{sw1} and i_r increase until the resonant current becomes positive at the end of this interval.

Since the voltage across the transformer is positive, the current in the secondary side flows through D_1 and charges C_1. This situation will stay until the transformer voltage changes polarity at time t_4.

[$t_1 < t < t_2$]: During this interval, the resonant current is positive, and the behavior is similar to the previous stage. The switch current i_{sw1} will increase until it becomes positive at the end of the interval, making S_1 turn on under ZVS conditions.

[$t_2 < t < t_3$]: At the start of this stage, the switch S_1 is turned on, and the DC-link capacitor is discharging, while i_b is still decreasing. i_{sw1} and i_r increase until the gate signal is removed from S_1 at the end of the interval.

[$t_3 < t < t_4$]: At time t_3 the gate signal of S_1 is removed. Due to the snubber capacitor $C_{S1,}$ the voltage across S_1 rises gradually after the gate signal is removed. The duration of this interval, known as deadtime, should be enough to ensure the ZCS turn-off of the switch.

[$t_4 < t < t_5$]: At time t_4, the gate signal V_{gs2} is applied to the switch S_2. Since the resonant current is positive at the moment and higher than i_b, i_{sw2} is negative and flows through the anti-parallel diode of S_2. In this stage, the boost inductor is charging and i_b is increasing. i_r decreases while

i_{sw2} increases until it becomes positive at the end of the interval, making S_2 turn on under ZVS conditions.

Since the voltage across the transformer is negative, the current in the secondary side flows through D_2 and charges C_2. This condition persists until the system returns to the initial state.

[$t_5 < t < t_6$]: At the start of this stage, the switch S_2 is turned on. i_b and i_{sw2} are increasing, while i_r continues to decrease until it becomes negative at time t_6.

[$t_6 < t < t_7$]: During this interval, the resonant current is negative and similar to the previous stage, i_b and i_{sw1} are still increasing while i_r decreases until the gate signal is removed from S_2 at the end of the interval.

[$t_7 < t < t_8$]: At time t_7 the gate signal of S_2 is removed. Due to the snubber capacitor C_{S2}, the voltage across S_2 rises gradually after the gate signal is removed. The duration of this interval, known as deadtime, should be enough to ensure the ZCS turn-off of the switch. This stage ends once the gate signal is applied to S_1 and the system transitions back to the first state.

The effect of interleaving two modules is depicted in Figure 2.6. The input current is the sum of the boost inductor currents of each module, and since they have a 180° phase difference, the ripple of the input current is much lower. Ideally, the ripple is zero at $d = 0.5$.

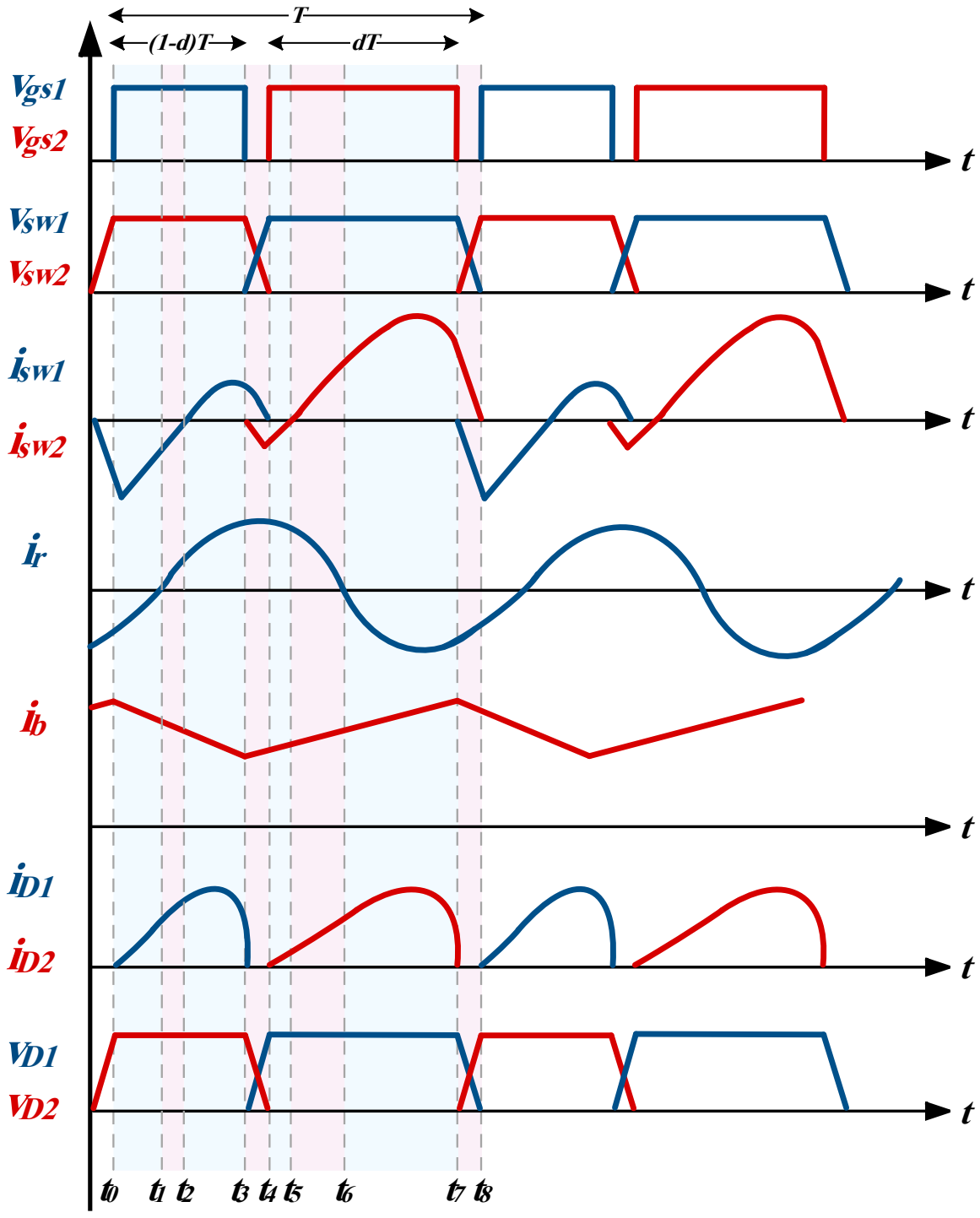

Figure 2.4- The operating waveforms of the converter for $d > 0.5$ (one module)

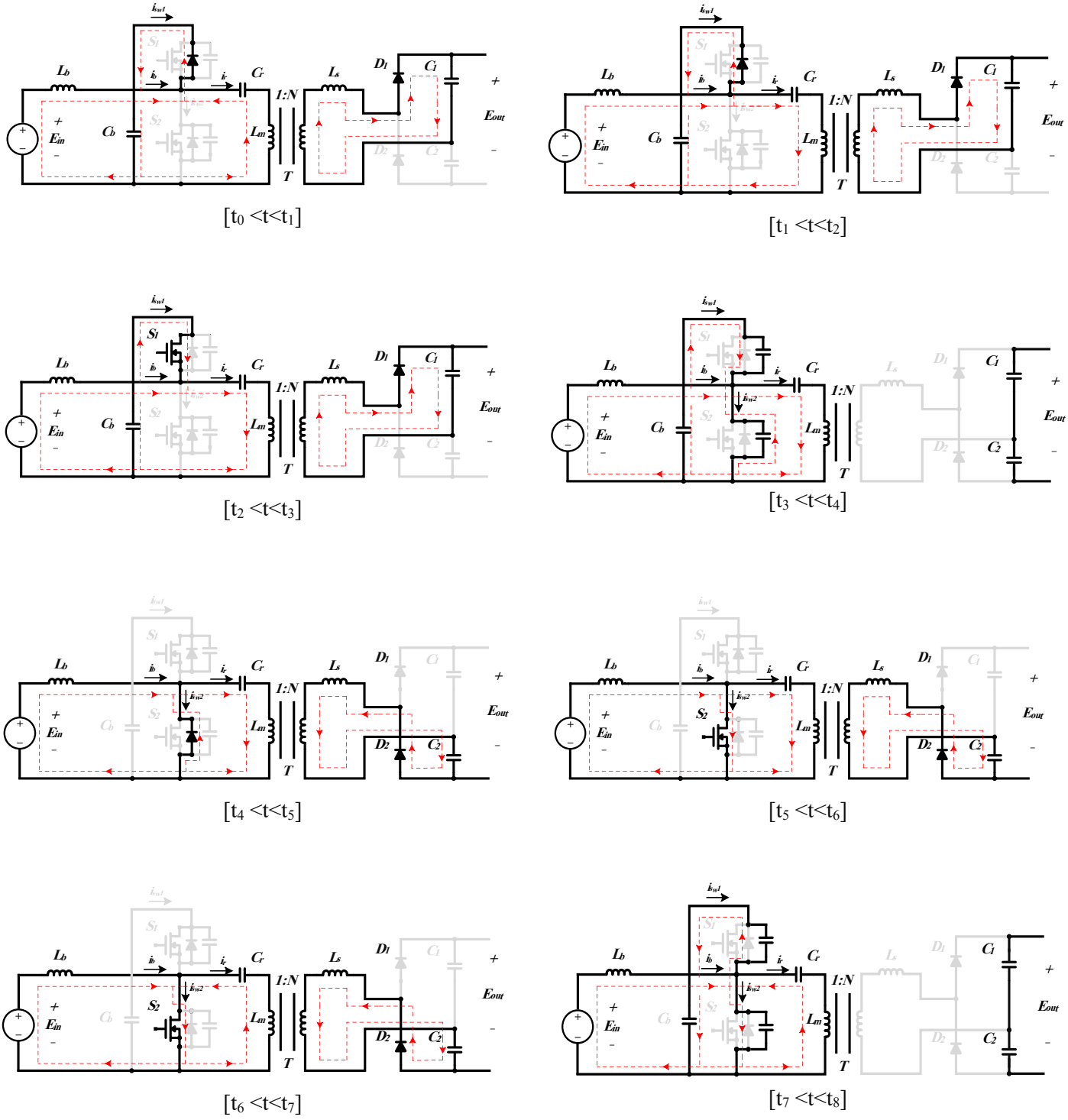

Figure 2.5- The key operating stages of the circuit (one module)

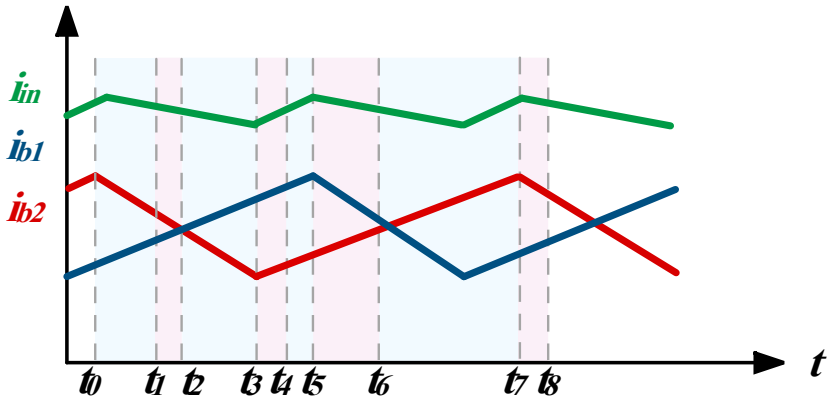

Figure 2.6- The operating current waveforms of the interleaved converter for $d > 0.5$

2.1.2 Converter Theoretical Analysis

This section presents a detailed steady-state analysis of the converter. For simplification, only one module is considered. The following assumptions are made in the analysis.

1. All components, such as semiconductor switches, diodes, inductors, and capacitors, are ideal unless stated otherwise.
2. The delay between the switch gating signals is neglected.
3. The effect of snubber capacitors is neglected.

2.1.2.1 DC Link Capacitor and Switch Voltage

Figure 2.7 shows the first stage of the converter when (a) switch S_2 is on, and (b) when it is off. Switches S_1 and S_2 operate in complementary duty ratios. The duty ratio of switch S_2 is denoted by d. When switch S_2 is on, the voltage across the boost inductor is E_{in}, and when switch

S_2 is off, the voltage across the boost inductor is $(E_{in} - V_{Cb})$. In steady-state operation of the converter, the integral of the inductor voltage over the period T must be zero. Therefore, we have:

$$(E_{in})(dT) = (E_{in} - V_{Cb})(1 - d)T \tag{2.2}$$

$$V_{Cb} = \frac{1}{1-d} E_{in} \tag{2.3}$$

Also, the voltage across both switches when they are off is V_{Cb}.

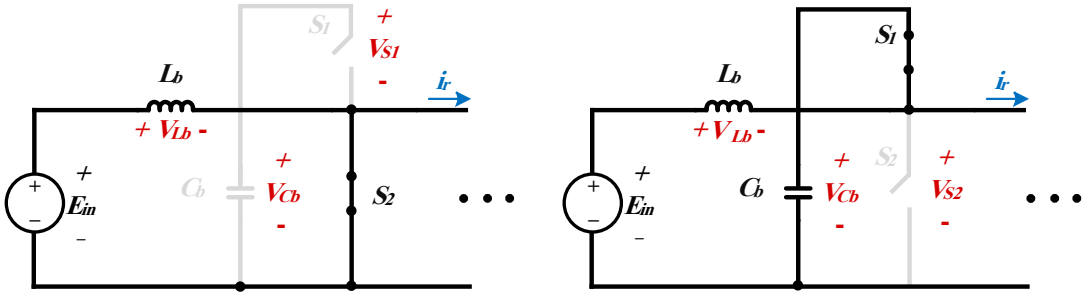

Figure 2.7- The first stage of the converter (a) S_2 is on (b) S_2 is off

2.1.2.2 Resonant Voltage

The rectangular voltage waveform applied to the resonant circuit, which is generated by the two switches, is depicted in Figure 2.8. The Fourier series of the waveform is given in (2.4) to (2.7). Due to the DC blocking capability of the resonant capacitor, only the AC component is applied to the resonant circuit. Since the harmonic content in the resonant circuits can be assumed to be negligible, the fundamental approximation is then used in the following calculations. (2.9)

shows the fundamental component of the resonant input voltage where f_s is the operating switching frequency and θ is the phase angle.

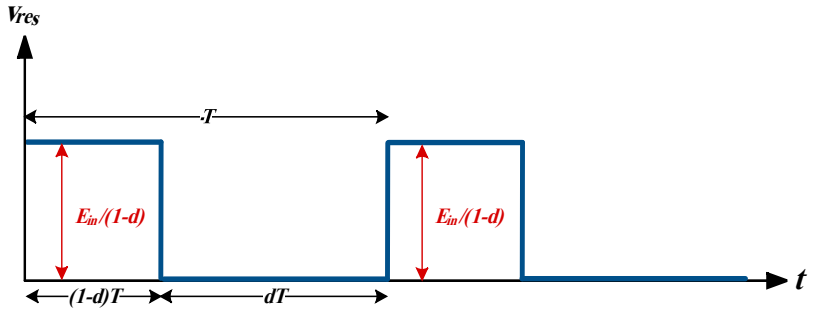

Figure 2.8- The square rectangular voltage waveform applied to the resonant circuit

$$v_{res} = \frac{a_0}{2} + \sum_{n=1}^{\infty} (a_n \cos(n\omega_0 t) + b_n \sin(n\omega_0 t)) \tag{2.4}$$

$$a_0 = V_{Cb}(1-d) \tag{2.5}$$

$$a_n = \frac{2}{T}\int_0^T x(t)\cos(n\omega_0 t)dt = \frac{V_{Cb}}{n\pi}\sin\big(2n\pi(1-d)\big) \tag{2.6}$$

$$b_n = \frac{2}{T}\int_0^T x(t)\,\sin(n\omega_0 t)\,dt = \frac{V_{Cb}}{n\pi}(1-\cos(2\pi(1-d)) \tag{2.7}$$

$$V_{Cb} = \frac{1}{1-d}E_{in} \tag{2.8}$$

$$V_{res} = \frac{\sqrt{2}E_{in}}{(1-d)\pi}\sqrt{1-\cos(2\pi(1-d))}\,\sin(2\pi f_s t + \theta) \tag{2.9}$$

$$\theta = \tan^{-1}\left(\frac{\sin\big(2\pi(1-d)\big)}{1-\cos(2\pi(1-d)}\right) \tag{2.10}$$

$$\left|\frac{V_{res}}{E_{in}}\right| = \frac{\sqrt{2}}{(1-d)\pi}\sqrt{1-cos(2\pi(1-d))} \tag{2.11}$$

2.1.2.3 Voltage Gain

The total voltage gain of the converter includes the boost stage, the resonant stage, and the voltage doubler rectifier. The boost stage was analyzed earlier in (2.3). Figure 2.9 shows the fundamental harmonic equivalent resonant circuit. The CLL resonant tank includes C_r, L_m, and L_s, where L_m represents the magnetizing inductance of the high-frequency transformer. The leakage inductance of the transformer is neglected, and the load is shown as an equivalent resistance (R_L). For simplification, the voltage doubler rectifier and the load can be replaced by an equivalent resistance and all the components can be transferred to the primary side of the transformer, as shown in Figure 2.10. R_{ac} is defined by (2.12). L_{sp} is the equivalent secondary side inductance transferred to the primary side and can be obtained by (2.13). Considering these assumptions and only the fundamental frequency, basic AC circuit analysis can be performed.

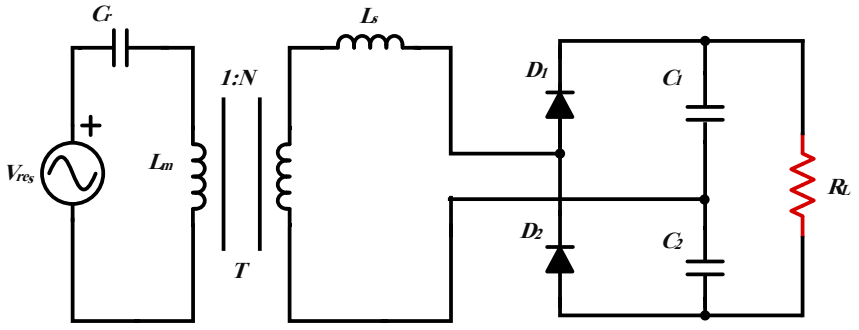

Figure 2.9- The fundamental harmonic equivalent resonant circuit

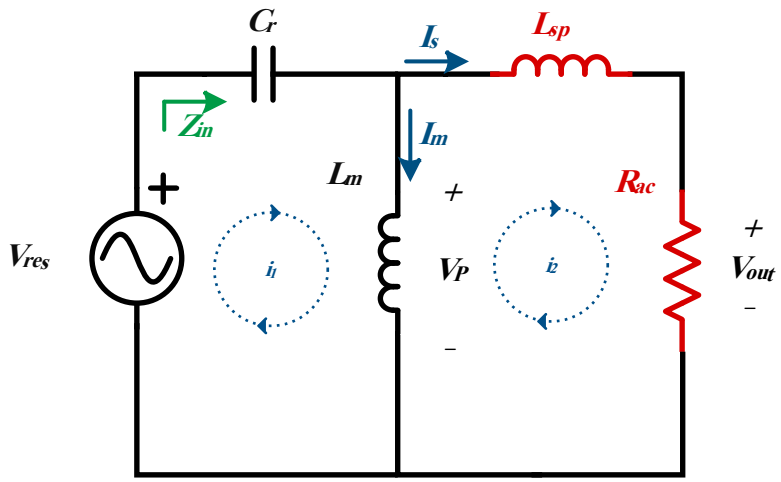

Figure 2.10- The fundamental harmonic equivalent resonant circuit transferred to the primary side

$$R_{ac} = \frac{2}{N^2\pi^2} R_L \tag{2.12}$$

$$L_{sp} = \frac{L_s}{N^2} \tag{2.13}$$

$$KVL\ I:\ -V_{in} - jX_{C_r} i_1 + jX_{L_m}(i_1 - i_2) = 0 \tag{2.14}$$

$$KVL\ II:\ jX_{L_m}(i_2 - i_1) + jX_{L_{s1}} i_2 + R_{ac} i_2 = 0 \tag{2.15}$$

$$i_2 = \frac{jX_{L_m} V_{res}}{X_{L_m}X_{C_r} - X_{L_{s1}}X_{L_m} + X_{L_{s1}}X_{C_r} + jR_{ac}(X_{L_m} - X_{C_r})} \tag{2.16}$$

$$V_{out} = i_2 \times R_{ac} \tag{2.17}$$

$$\frac{V_{out}}{V_{res}} = \frac{jX_{L_m} R_{ac}}{X_{L_m}X_{C_r} - X_{L_{s1}}X_{L_m} + X_{L_{s1}}X_{C_r} + jR_{ac}(X_{L_m} - X_{C_r})} \tag{2.18}$$

The ratio between the series and the magnetizing inductances is defined as $k = L_{sp}/L_m$. The full-load equivalent inductance L_e is approximated to be the parallel combination of these

inductances given by (2.19). The angular resonant frequency ω_0 *(rad/s),* quality factor Q, angular operating frequency and normalized angular switching frequency are defined as follows.

$$L_e = \frac{L_m L_{sp}}{L_{m+} L_{sp}} = \frac{k}{k+1} L_m = \frac{L_{sp}}{k+1} \tag{2.19}$$

$$\omega_0 = \frac{1}{\sqrt{L_e C_r}} \tag{2.20}$$

$$Q = \frac{R_{ac}}{\omega_0 L_e} = R_{ac} C_r \omega_0 \tag{2.21}$$

$$\omega_s = 2\pi f_s \tag{2.22}$$

$$\omega_r = \frac{\omega_s}{\omega_0} \tag{2.23}$$

By applying the above assumptions to the resonant voltage gain, the following simplified equation is obtained.

$$\frac{V_{out}}{V_{res}} = \frac{1}{\left(1 - \frac{k}{\omega_r^2 (k+1)}\right) + j \frac{1}{Q\omega_r} \left((-1-k) + \omega_r^2 (k+1) \right)} \tag{2.24}$$

$$\left|\frac{V_{out}}{V_{res}}\right| = \frac{1}{\sqrt{\left(1 - \frac{k}{\omega_r^2 (k+1)}\right)^2 + \left(\frac{1}{Q\omega_r}\left((-1-k) + \omega_r^2 (k+1)\right)\right)^2}} \tag{2.25}$$

Furthermore, the voltage gain of the voltage doubler rectifier is given by (2.26).

$$\left|\frac{E_{out}}{V_{out}}\right| = \frac{N\pi}{2} \tag{2.26}$$

By using (2.11), (2.25) and (2.26), the proposed converter's total voltage gain can be achieved as:

$$G_{total} = \left|\frac{V_{res}}{E_{in}} \times \frac{V_{out}}{V_{res}} \times \frac{E_{out}}{V_{out}}\right| \tag{2.27}$$

$$G_{total} = \frac{N\sqrt{1 - cos(2\pi(1-d))}}{\sqrt{2}(1-d)\sqrt{\left(1 - \frac{k}{\omega_r^2(k+1)}\right)^2 + (\frac{1}{Q\omega_r}\left((-1-k) + \omega_r^2(k+1)\right))^2}} \tag{2.28}$$

A plot of voltage gain as a function of k and ω_r is depicted in Figure 2.11. Over a range of ω_r, the voltage gain reaches its peak at a specific value of k known as $k_{critical}$. Furthermore, Figure 2.12 (a) shows that with higher values of k, higher gains can be achieved. However, increasing k has limitations, which will be explained later. Figure 2.12(b) and 2.11(c) show the voltage gain for different values of Q and d.

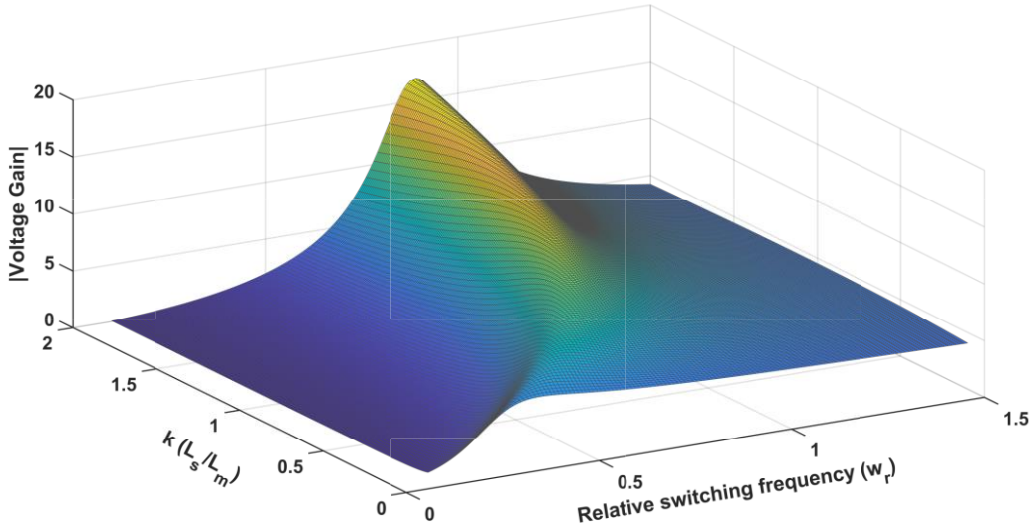

Figure 2.11- Voltage gain as a function of k and ω_r for $Q=5$ and $d=0.5$

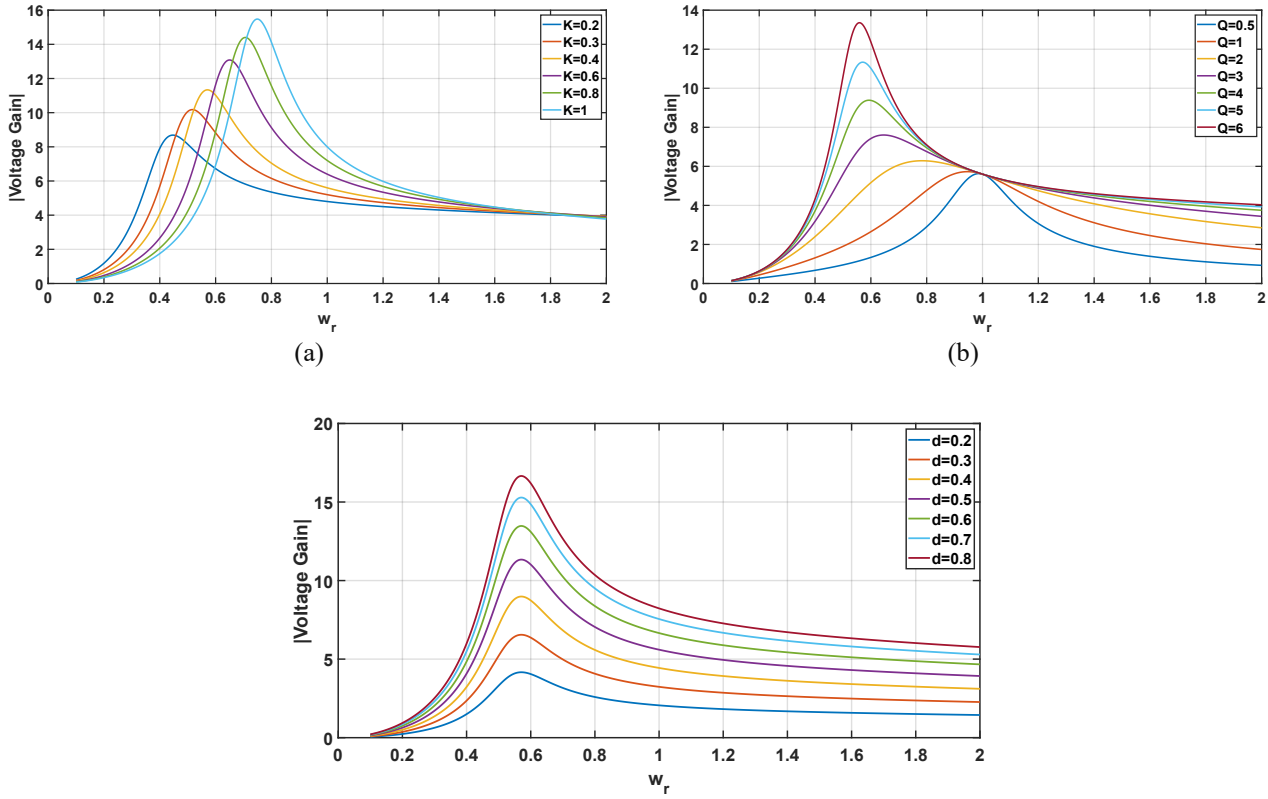

Figure 2.12- Voltage gain plot for different (a) Q with $k=0.4$, $d=0.5$ (b) k with $Q=5$, $d=0.5$ (b) d with $Q=5$, $k=0.4$

2.1.2.4 Resonant Current

The fundamental component of the resonant current is given by (2.29), where $|Z_{in}|$ is the magnitude of fundamental harmonic of the input impedance and $\emptyset_{Z_{in}}$ is the phase angle of the mentioned impedance.

$$I_r = \frac{\sqrt{2}E_{in}}{(1-d)\pi|Z_{in}|}\sqrt{1-cos(2\pi(1-d))}\,sin\left(2\pi f_s t + \theta - \emptyset_{Z_{in}}\right) \tag{2.29}$$

$$Z_{in} = R_{ac}\frac{(\frac{1}{k}+1)(1-\omega_r^2)+jQ(\frac{\omega_r}{k}-\frac{1}{\omega_r(1+k)})}{\frac{Q^2}{k+1}+jQ\omega_r(\frac{1}{k}+1)} \tag{2.30}$$

$$\emptyset_{Z_{in}} = \tan^{-1}\left(\frac{Q(\frac{\omega_r}{k}-\frac{1}{\omega_r(1+k)})}{(\frac{1}{k}+1)(1-\omega_r^2)}\right) - \tan^{-1}\left(\frac{Q\omega_r(\frac{1}{k}+1)}{\frac{Q^2}{k+1}}\right) \tag{2.31}$$

From (2.29) the peak and RMS value of the fundamental resonant current can be determined as shown in the following, respectively.

$$I_{res_{(peak)}} = \frac{\sqrt{2}E_{in}}{(1-d)\pi|Z_{in}|}\sqrt{1-cos(2\pi(1-d))} \tag{2.32}$$

$$I_{res_{(rms)}} = \frac{E_{in}}{(1-d)\pi|Z_{in}|}\sqrt{1-cos(2\pi(1-d))} \tag{2.33}$$

In order to operate in the ZVS condition, the switch currents should be inductive, meaning they should lag the switch voltage. Since the switch current is the sum of resonant current and boost current, assuming a reasonable approximation, this implies that the value of $\emptyset_{Z_{in}}$should always be positive. Thus, the switching and resonant frequencies should be selected in such a way that ω_r ensures a positive phase angle for the input impedance. Figure 2.13 shows $\emptyset_{Z_{in}}$, as a function of ω_r for different values of Q and k. It can be observed by changes in Q and k, the ZVS region is achieved under different values of ω_r.

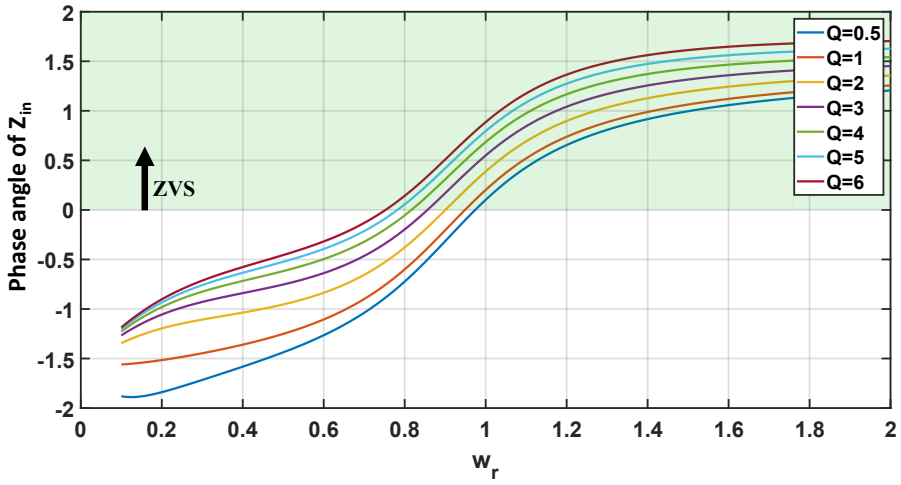

(a)

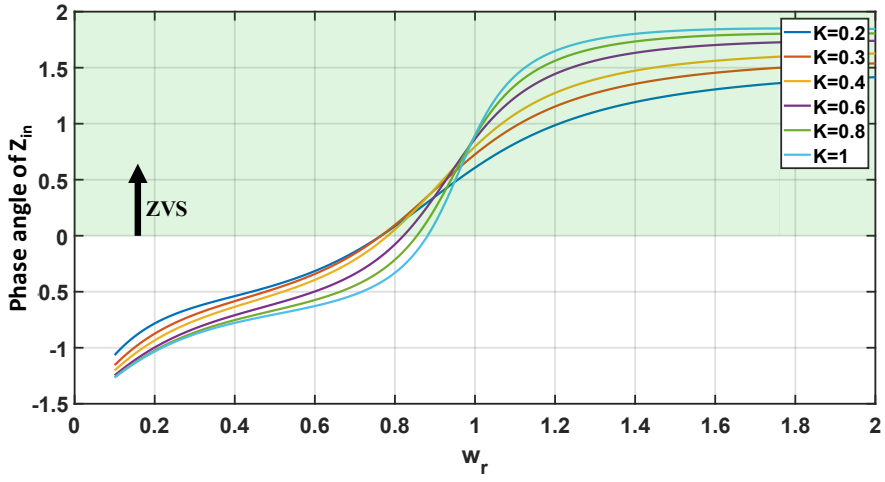

(b)

Figure 2.13- Plot of $\emptyset_{Z_{in}}$ as a function of ω_r For different values of (a) Q with *k=0.4,* (b) k with *Q=5*

Also, according to Figure 2.10, the ratio of the magnetizing inductor *(L_m)* current to the series inductor current *(L_{sp})* is given by (2.37). It shows that increasing the operating frequency and reducing k and the quality factor can effectively reduce the circulating current in the circuit, leading to reduced conduction losses. As k approaches zero (i.e., by increasing L_m), the circuit behaves like a series-resonant converter, and the current through the parallel branch approaches zero. This results in lower conduction losses. However, with a higher k (smaller L_m), more current flows through the parallel branch, reducing efficiency. Also, as mentioned before, higher k will result in higher voltage gain. Therefore, there is a size, efficiency and voltage gain tradeoff in choosing the value for k.

$$I_m = \frac{V_p}{jX_{L_m}} \tag{2.34}$$

$$I_s = \frac{V_p}{jX_{L_{sp}} + R_{ac}} \tag{2.35}$$

$$\frac{I_m}{I_s} = k\left(1 - j\frac{Q}{\omega_r k}\right) \tag{2.36}$$

$$\left|\frac{I_m}{I_s}\right| = k\sqrt{1 + \frac{Q^2}{{\omega_r}^2 k^2}} \tag{2.37}$$

2.1.2.5 Turn-Off Current of S_1

The turn-off current of S_1 can be achieved form the following equation at time $t = (1-d)T$.

$$I_{sw1(off)} = I_{res} - I_b \tag{2.38}$$

$$I_{sw1(off)} = \frac{\sqrt{2}E_{in}}{(1-d)\pi|Z_{in}|}\sqrt{1-\cos\big(2\pi(1-d)\big)}\,sin\big(2\pi f_s(1-d)T+\theta-\emptyset_{Z_{in}}\big) - I_b \tag{2.39}$$

To turn on S_2 under zero voltage switching, as shown in Figure 2.5, this current should force the S_2 antiparallel diode to conduct prior to the turn-on instant of the switch. Hence, $I_{sw1(off)}$ should be positive.

2.1.2.6 Turn-Off Current of S_2

The turn-off current of S_2 can be achieved form the following equation at time t =0.

$$I_{sw2(off)} = I_b - I_{res} \tag{2.40}$$

$$I_{sw2(off)} = I_b - \frac{\sqrt{2}E_{in}}{(1-d)\pi|Z_{in}|}\sqrt{1-\cos\big(2\pi(1-d)\big)}\,sin\big(\theta-\emptyset_{Z_{in}}\big) \tag{2.41}$$

To turn-on S_1 under zero voltage switching, this current should force the S_1 antiparallel diode to conduct prior to the turn-on instant of the switch. Hence, $I_{sw2(off)}$ should be positive.

2.2 Simulation Results

To demonstrate the operation of the proposed converter, a 900W 100VDC to 1.9kVDC high-gain CLL converter with an integrated interleaved boost stage is simulated using the circuit simulation software PowerSim (PSIM). This software is specially designed for power electronics simulation. The proposed converter was designed using PSIM's schematic capture interface, and its simulation results were obtained via the Simview waveform viewer. In this chapter, the converter is tested with a DC voltage source, and its duty ratio is controlled using an open-loop approach for performance verification. The results and analysis of PV integration will be discussed in the next chapter. The base switching frequency of the converter is selected to be 70 kHz to minimize the size of the converter and its components. Note that the design procedure for the proof-of-concept circuit will be presented in Section 2.3. Figure 2.14 shows the operating waveforms of the switches in both modules. All four switches are operating under ZVS conditions as a negative current flows through them before turn-on. Figure 2.15 demonstrates the current of the boost inductors for both modules and the input current. As expected, with a duty ratio of $d=0.5$, the input current has almost zero ripple as the two modules are 180° out of phase. The input and output voltages are also shown, which demonstrates the converter's high voltage gain of nearly 20. The switching waveforms of the voltage doubler rectifier are shown in Figure 2.16, demonstrating the ZCS switching of the diodes. Figure 2.17 shows the primary and secondary sides current of the transformer. It illustrates that during each period, there is a time interval with no current on the secondary side, enabling the ZCS operation of the diodes. The input and output power of the converter are shown in Figure 2.18, which indicates an efficiency of 98% at full load.

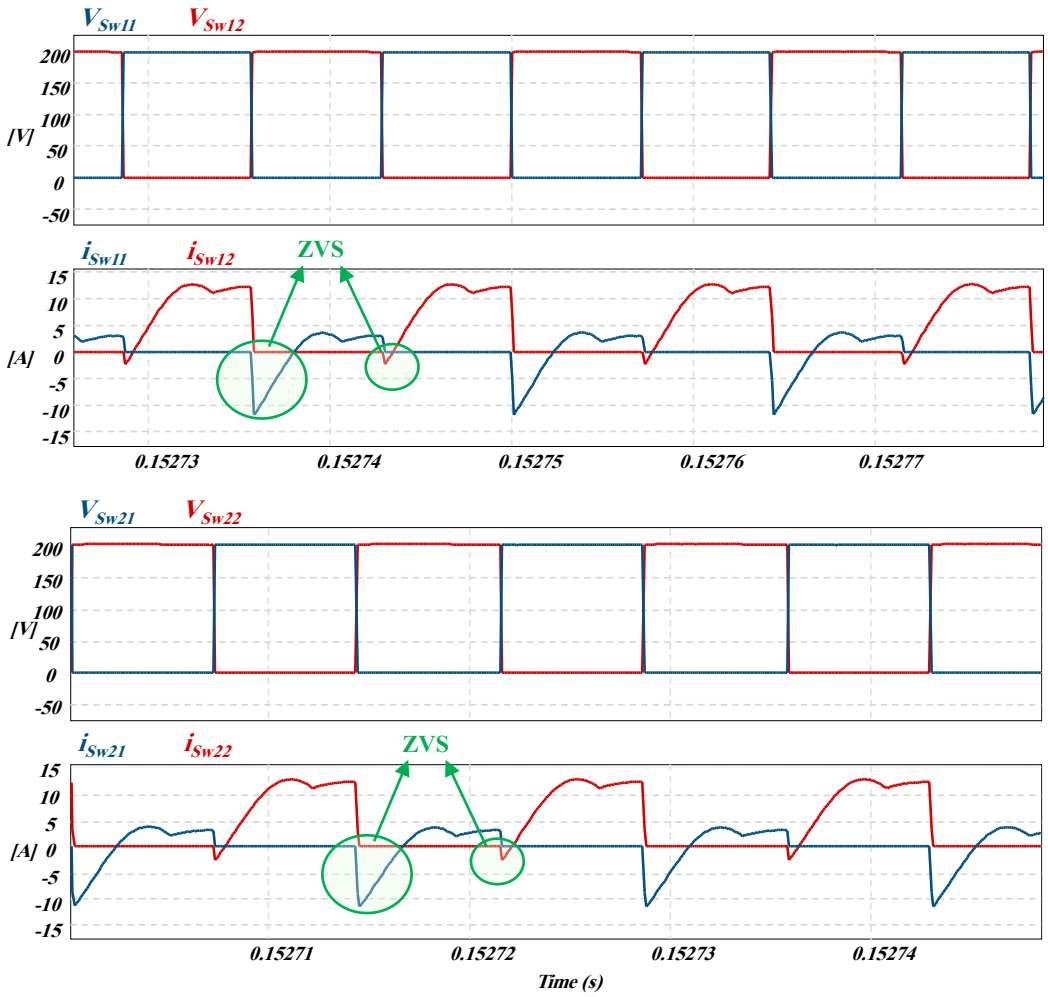

Figure 2.14- Operating switching waveforms for both modules

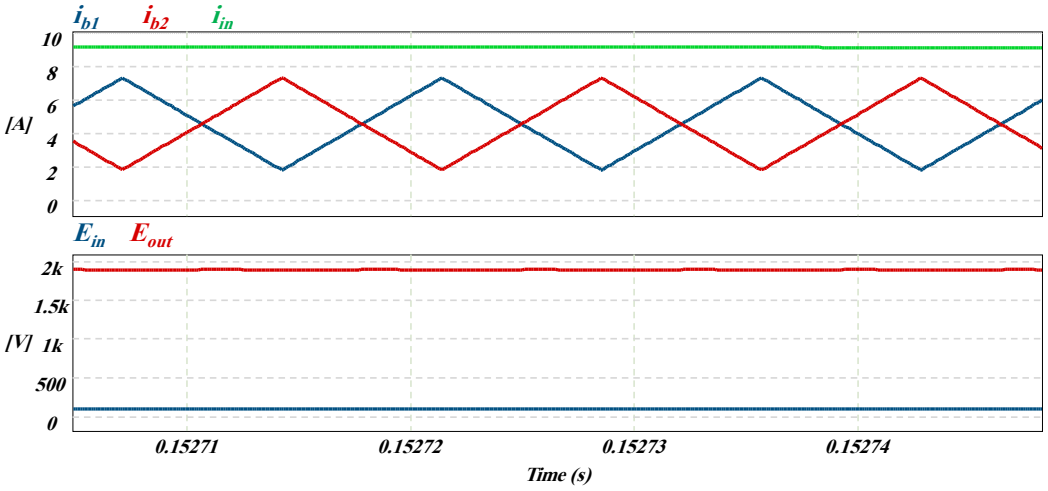

Figure 2.15- Operating waveforms for boost and input currents, input and output voltage ($d=0.5$)

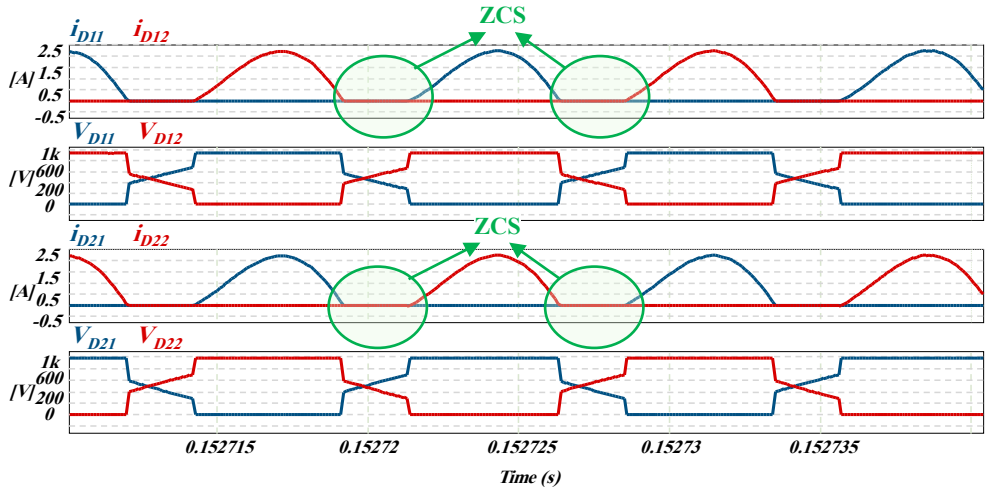

Figure 2.16- Operating waveforms for voltage doubler waveforms *(d=0.5)*

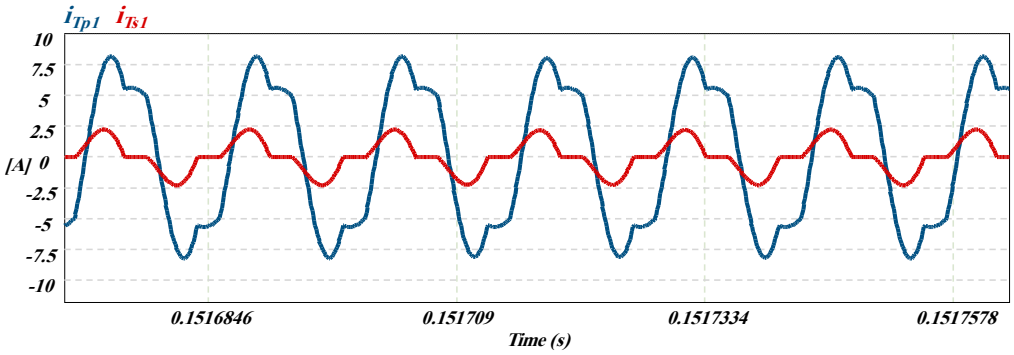

Figure 2.17- Operating waveforms for transformer primary and secondary current for one module (*d=0.5*)

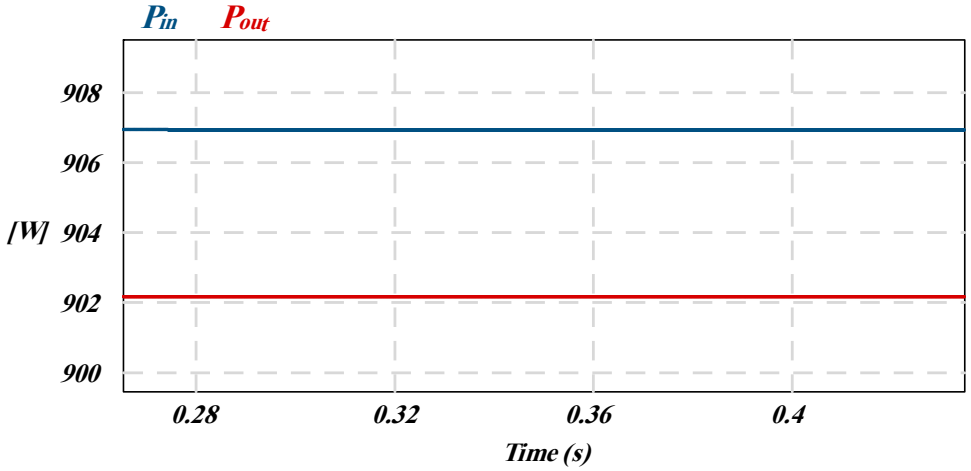

Figure 2.18- Simulation results for input and output power (*d=0.5*)

2.3 Design Procedure and Experimental Results

To further verify the performance of the proposed high-gain CLL converter with an integrated interleaved boost stage, a scaled-down 100W 40VDC/660VDC proof-of-concept hardware prototype is developed. Figure 2.19(a) shows the prototype, with the two modules stacked vertically. The experimental setup in the laboratory is shown in Figure 2.19(b). An InfiniiVision MSOX6004A oscilloscope from Keysight Technologies was used to obtain the experimental waveforms and measurements.

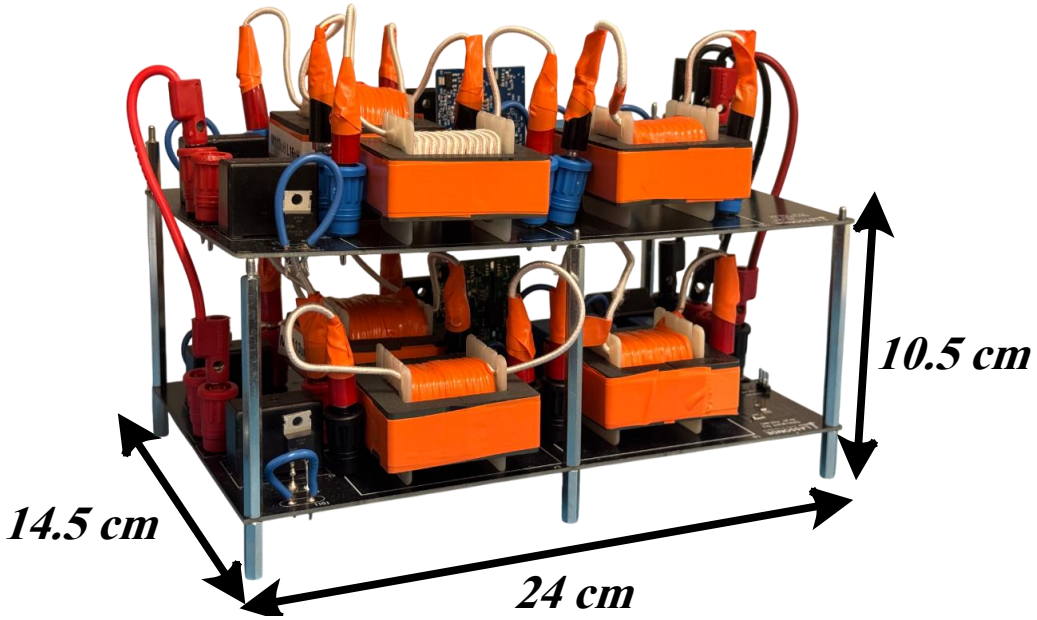

(a)

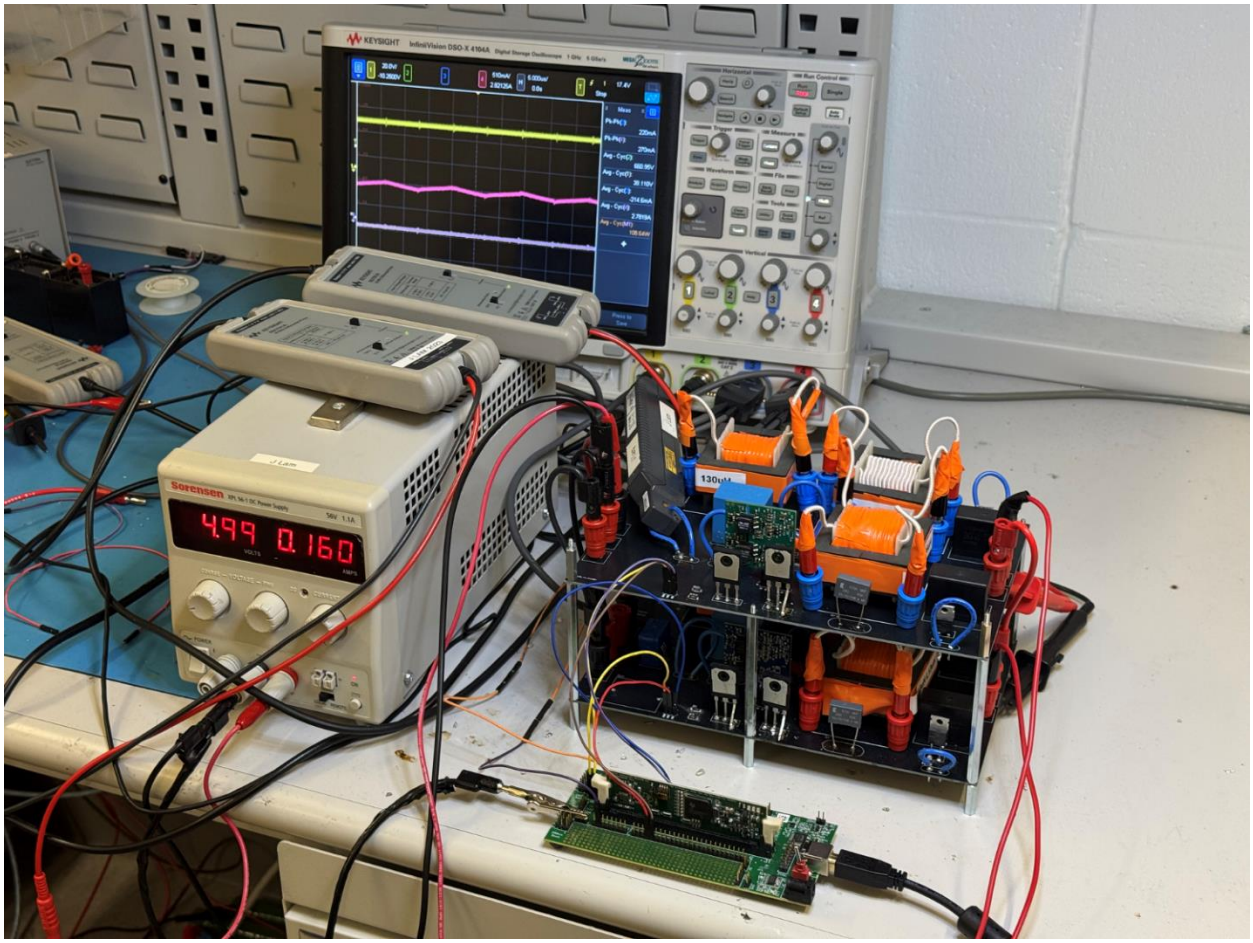

(b)

Figure 2.19- (a) Proof-of-concept prototype picture (b) experimental platform

The converter design involves the following steps. First, the equivalent output resistance is obtained by:

$$R_L = \frac{E_{out}^2}{P_{out}} = \frac{2000^2}{1000} = 2k\Omega \tag{2.42}$$

$$R_{ac} = \frac{2}{N^2\pi^2} R_L = 101\Omega \tag{2.43}$$

The base resonant frequency is assumed to be 100*kHz*. According to Figure 2.12, to achieve a total voltage gain of approximately 8, the values of Q, k, and N are chosen to be 5, 0.4 and 2, respectively. Then, the circuit parameters are chosen as follows:

$$\omega_o = 2\pi f_o = 2\pi \times 100kHz = 62.83 \times 10^4 \tag{2.44}$$

$$L_e = \frac{R_{ac}}{\omega_0 Q} = 32.25\mu H \tag{2.45}$$

$$L_{sp} = L_e(k+1) = 45\mu H \tag{2.46}$$

$$L_s = N^2 L_{sp} = 180\mu H \tag{2.47}$$

$$L_m = \frac{L_{sp}}{k} = 112\mu H \tag{2.48}$$

$$C_r = \frac{1}{{\omega_o}^2 L_e} = 78.54nF \tag{2.49}$$

A list of the final circuit parameters of the prototype and the simulation is summarized in Table 2.1. Figure 2.20(a) shows the converter input voltage and current, and output voltage; and 2.19(b) shows the input power. Given an output load of 4.1 kΩ, the output power, and subsequently the efficiency, can be calculated as follows:

$$P_{out} = \frac{{E_{out}}^2}{R_L} = \frac{660^2}{4.1k} = 106.24 \tag{2.50}$$

$$Efficiency = \frac{P_{out}}{P_{in}} = \frac{106.24}{108.6} \approx 98\% \quad (2.51)$$

Figure 2.21 and Figure 2.22 illustrate the switching waveforms of both modules. The waveforms confirm that the converter operates under ZVS conditions. The boost currents of both modules and the input current are depicted in Figure 2.23. The low ripple of the input current can be observed. The primary and secondary side currents of the transformer for both modules are shown in Figure 2.24, showing behaviour similar to the simulation results. In Figure 2.25, the switching waveforms of the voltage doubler are shown for both modules, which confirms the ZCS condition of the diodes.

Table 2.1- Simulation and hardware circuit parameters

Specifications

	Simulation	Scaled-down proof-of-concept
Rated Power	1kW	150W
Input Voltage	100V	40V
Output Voltage	1.9kV	660V
Operating Frequency	70kHz	70kHz

Circuit Components

	Simulation	Scaled-down proof-of-concept
Boost Inductance	130µH	130µH
Boost Capacitance	10µF	10µF
Resonant Capacitance	78.54nF	82nF
Magnetizing Inductance	112µH	112µH
Series Inductance	180µH	160µH
Voltage Doubler Capacitance	10µF	10µF
Output Load	$4k\Omega$	$4.1k\Omega$

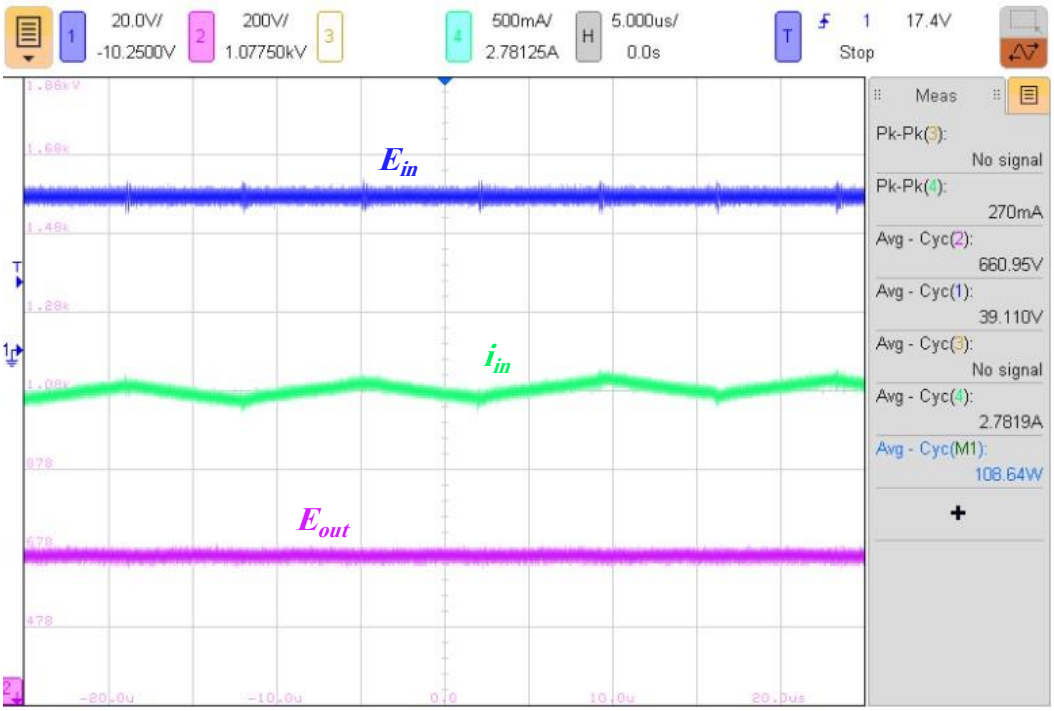

(a)

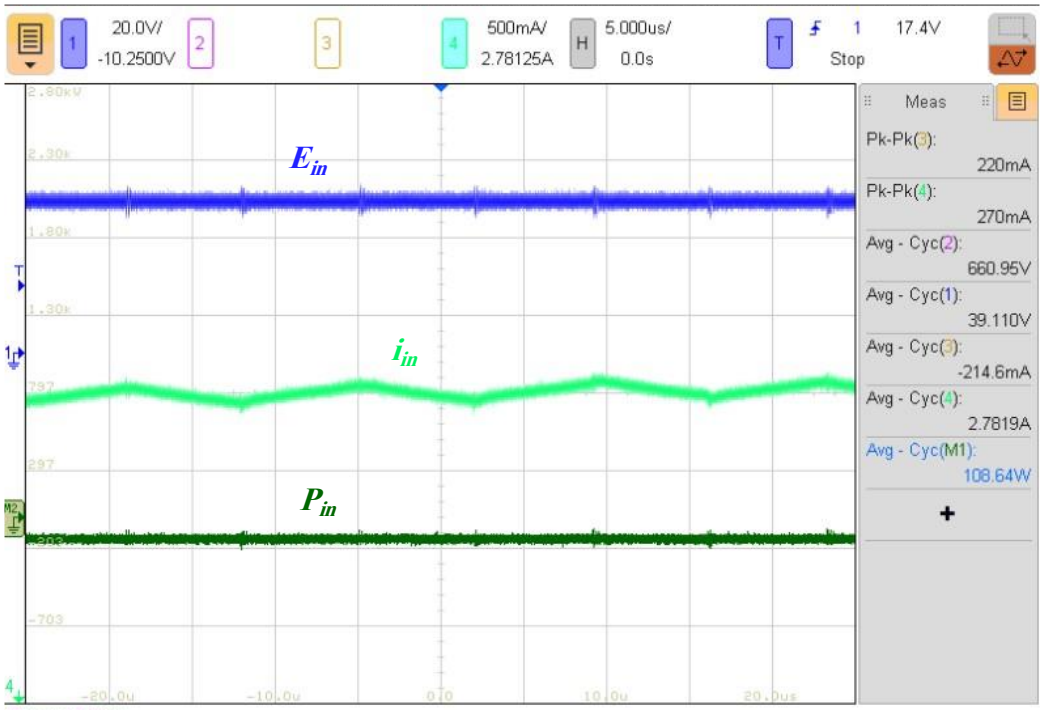

(b)

Figure 2.20- (a) Input voltage and current, and output voltage (b) Input voltage, current, and power

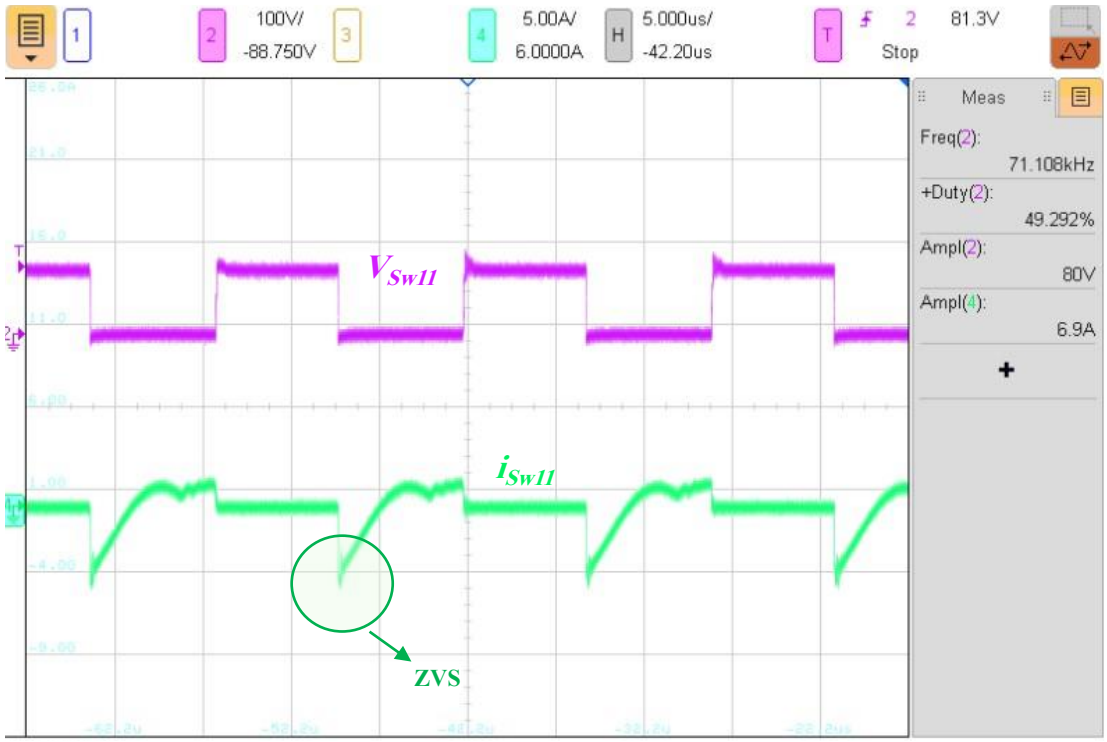

(a)

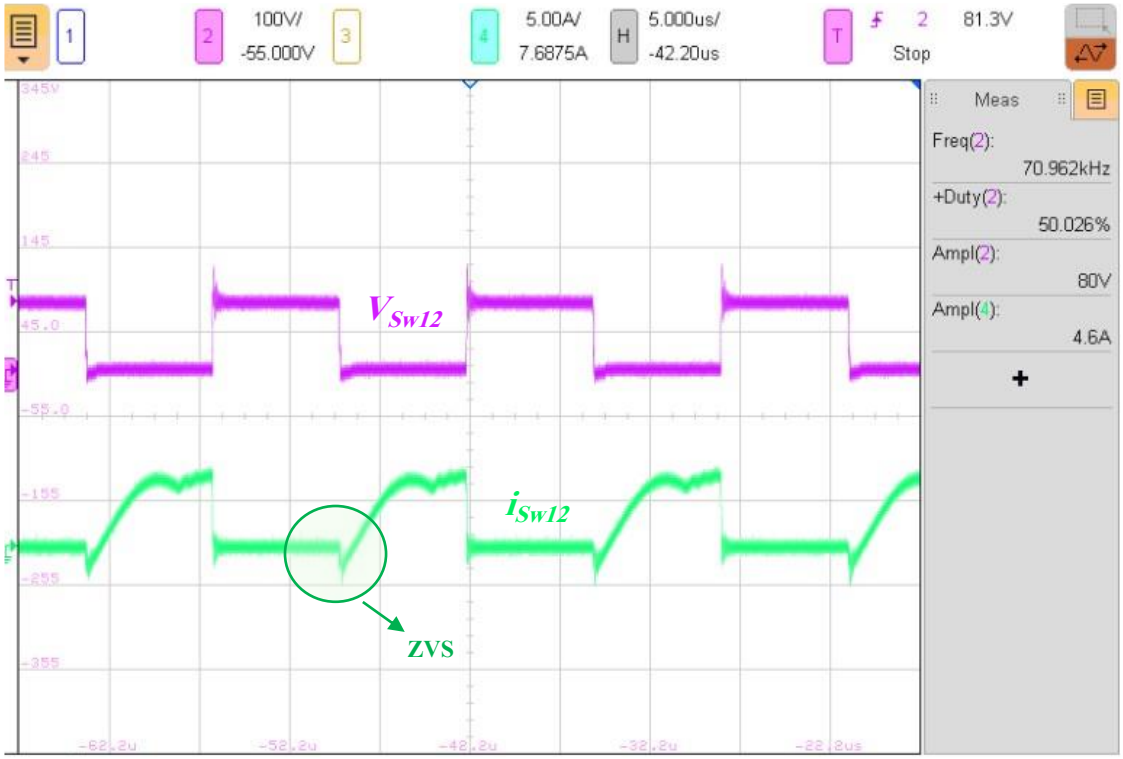

(b)

Figure 2.21- Module 1 experimental switching waveforms for *d=0.5*

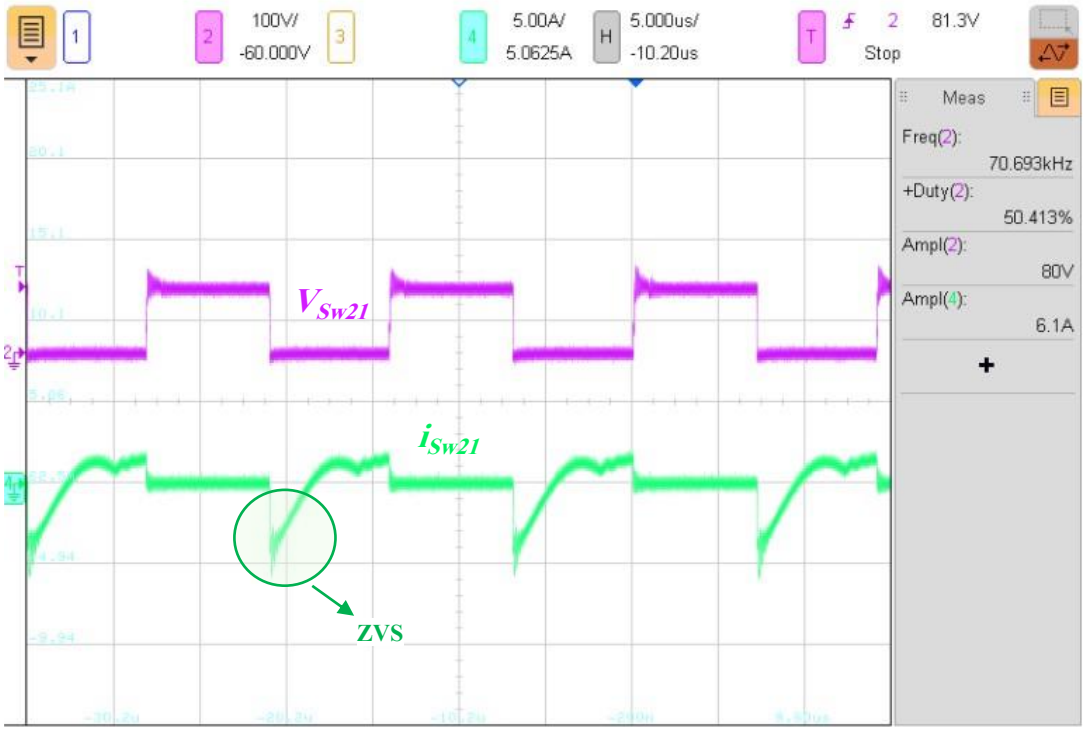

(a)

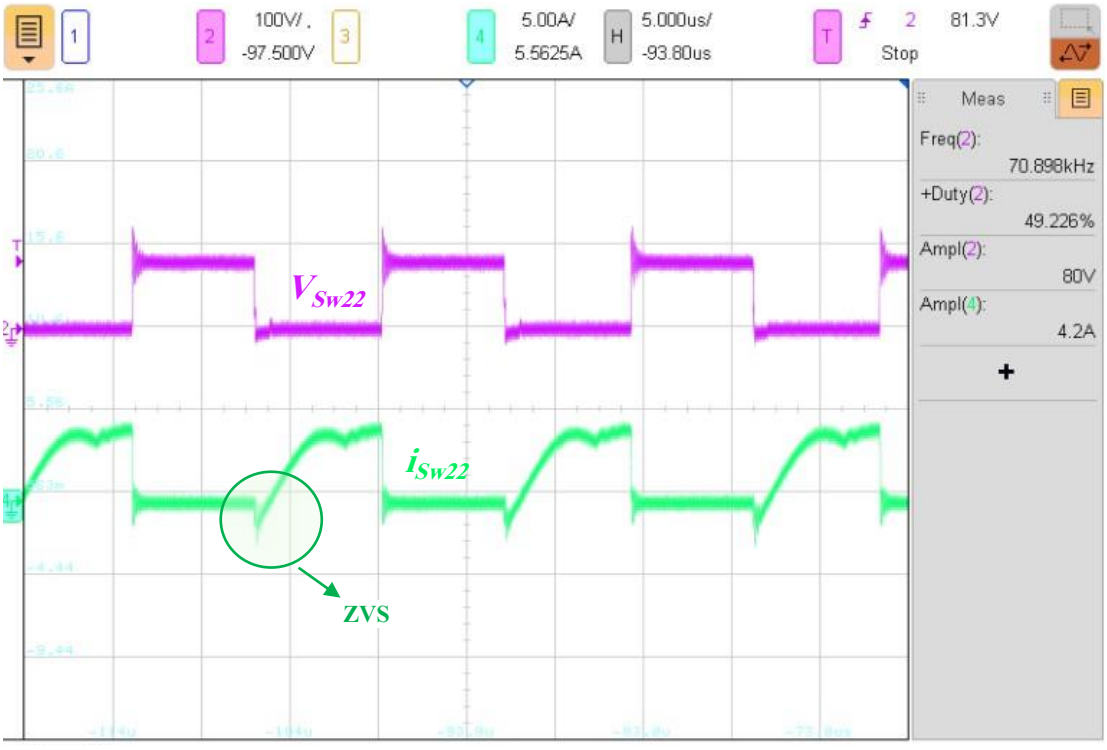

(b)

Figure 2.22- Module 2 experimental switching waveforms for d=0.5

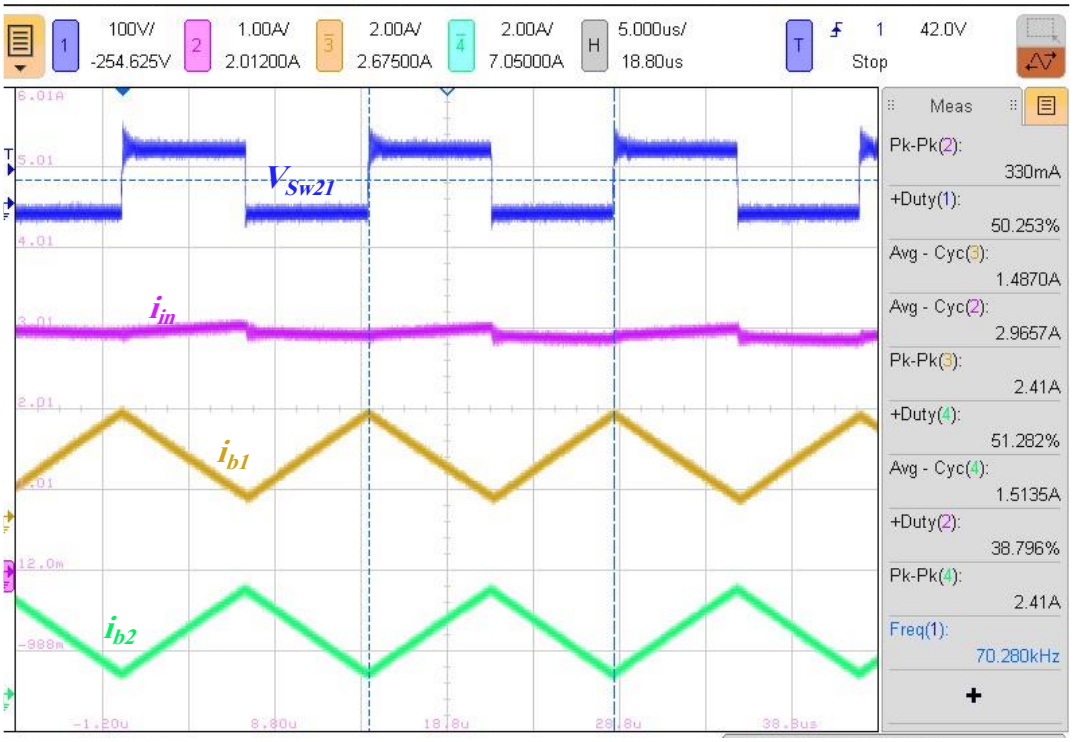

Figure 2.23- Boost current and input current experimental waveforms for *d=0.5*

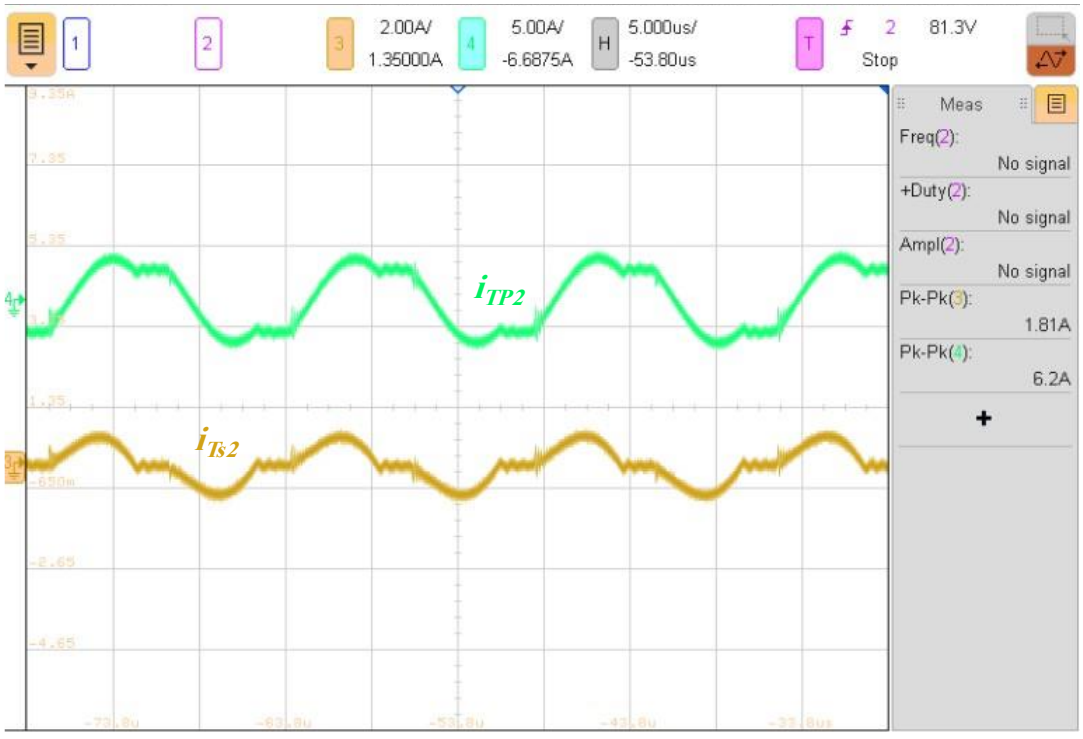

Figure 2.24- Module 2 transformer primary and secondary currents experimental waveforms *d=0.5*

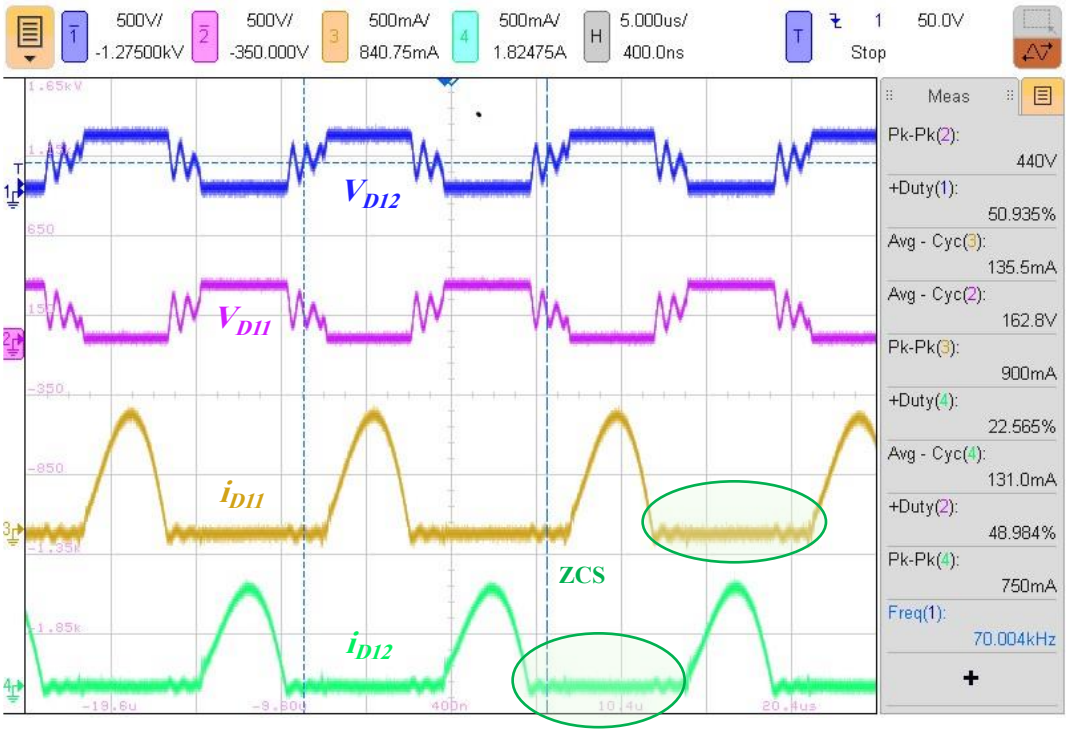

(a)

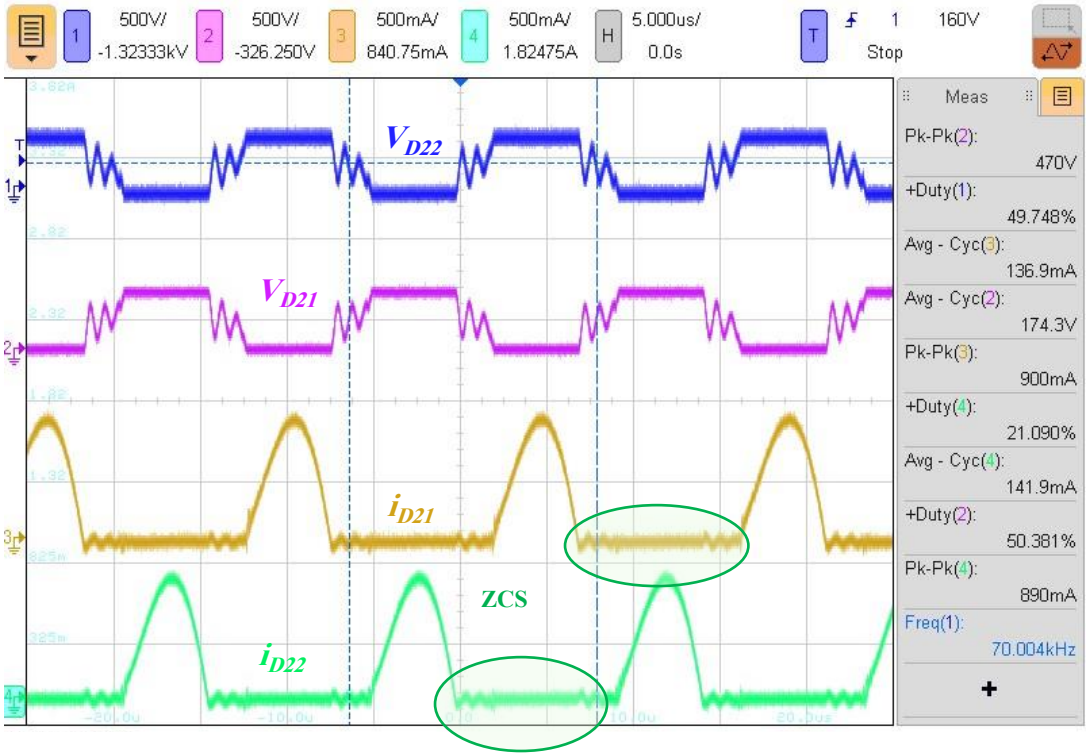

(b)

Figure 2.25- Voltage doubler experimental switching waveforms for *d=0.5* (a) Module 1 (b) Module 2

2.4 Chapter Summary

A high step-up single-stage soft-switched DC/DC converter topology combining an interleaved boost converter with a CLL resonant tank was proposed in this chapter for magnetron applications. The design integrates the boost and inverter stages into a single-stage converter. The system includes M modules interleaved together. This topology results in high voltage gain, low input and output current ripple and light stress on switching devices. Also, a detailed explanation of the converter's operating principles and theoretical analysis was presented.

The proposed converter was validated using both simulations and experimental tests. A 900W design was simulated in PSIM, showing a high voltage gain of approximately 20, high efficiency of up to 98%, and near ripple-free input current at 50% duty cycle due to the interleaving effect. The ZVS operation for the switches and ZCS operation for the diodes were validated. In addition, a 100W proof-of-concept hardware prototype was tested in the laboratory. Experimental data closely followed simulation results, such as soft-switching characteristics, large voltage gain, and low current ripple. A full-load efficiency of 98% was also measured.

Chapter 3 Photovoltaic MPPT Control Schemes for the Proposed Interleaved Converter

In the previous chapter, a high step-up single-stage DC/DC CLL resonant converter with an integrated interleaved boost stage for magnetron applications was proposed, and the operating principles and analysis were addressed. The converter's operation was validated in simulation and a hardware prototype using a DC power supply. This chapter will discuss the integration of the proposed converter with renewable energy systems by using photovoltaic (PV) panels as the input source.

First, two duty ratio control methods based on the P&O MPPT technique will be explained. These control schemes include a discrete logic-based MPPT and a PI-based MPPT approach. A small-signal analysis will be conducted for modeling the first stage of the proposed converter, which is essential for designing and implementing the control loop. Finally, simulation and experimental results will be provided to confirm the performance of the proposed converter and the control system.

3.1 Duty Ratio Control

As discussed in Chapter 1, implementing a Maximum Power Point Tracking (MPPT) method is essential for extracting the maximum available power from the photovoltaic (PV) panels. This tracking can be achieved by controlling parameters such as the switching frequency

or duty ratio of the converter connected to the panel. Among various MPPT methods, the P&O technique is one of the most widely used. This section will address duty ratio control schemes based on this method.

3.1.1 Discrete Logic-based MPPT

One of the most common methods used in the literature is a discrete logic-based duty ratio control using the P&O algorithm. This algorithm can be easily developed using a flowchart, as illustrated in Figure 3.1. The controller first reads the input (PV panel) voltage and current, then calculates the updated operating power. Next, the power and voltage differences between the current and the previous states are calculated. The polarity of ΔP and ΔV is then determined. Based on these values, the controller either increases or decreases the duty ratio and sends it to the pulse-width modulation unit. The values of voltage and power are stored for use in the next cycle. While this approach is simple and fast, it is sensitive to noise since the system dynamics are not considered, and it cannot be analyzed or optimized using control theory.

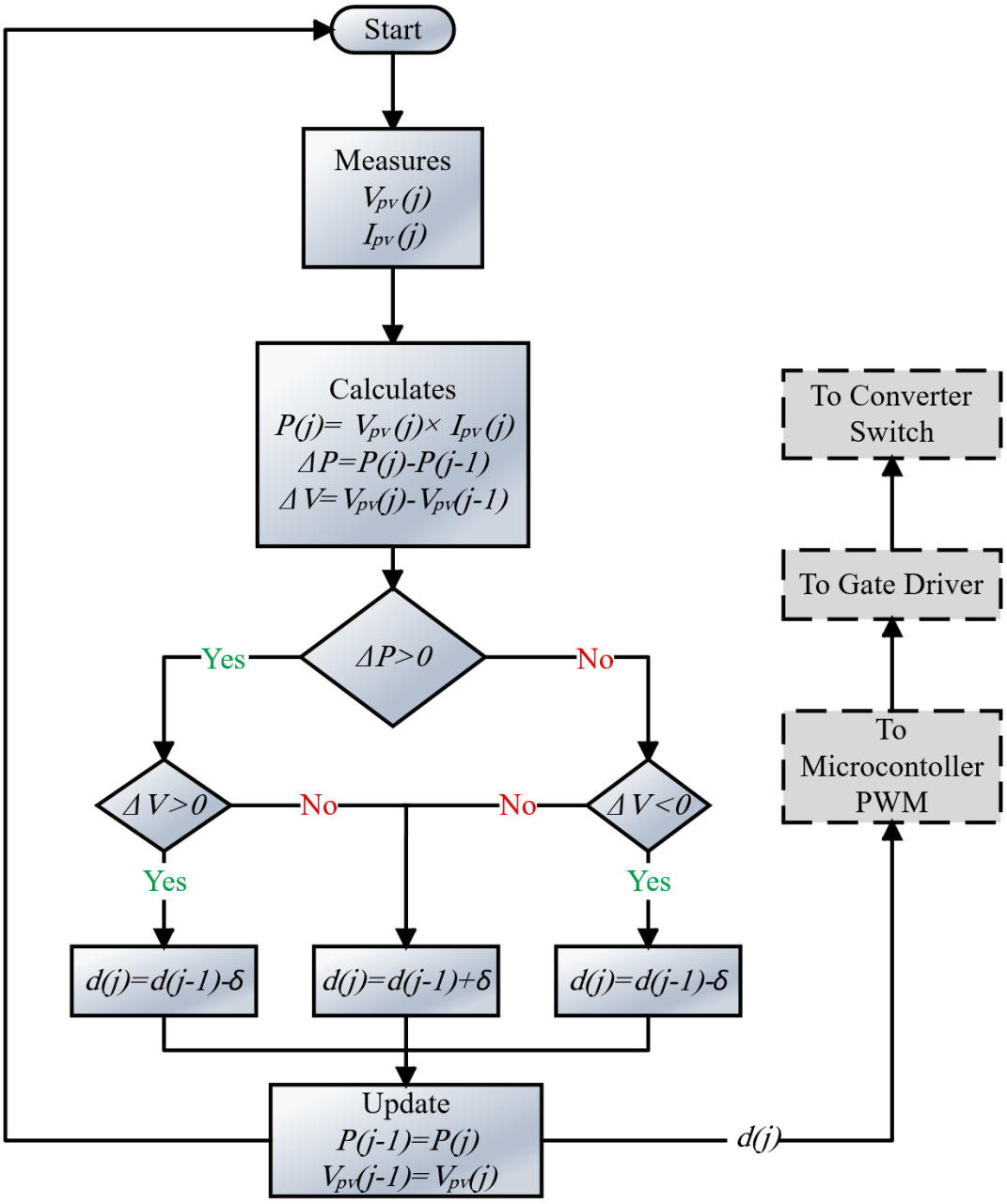

Figure 3.1- The P&O MPPT Method flowchart with duty ratio control

3.1.2 PI-based MPPT

In another duty ratio control method, the P&O algorithm is still used for MPPT; however, instead of directly adjusting the duty ratio, it updates a reference voltage, which represents the PV operating voltage corresponding to the maximum power point. A closed-loop control system is then used to regulate the actual PV operating voltage to match the reference voltage. A diagram of this control loop applied to the designed converter in Chapter 2 is shown in Figure 3.2.

As demonstrated, the error between the reference voltage received from the MPPT algorithm and the actual PV panel voltage is calculated and fed into a Proportional-Integral (PI) controller. The controller minimizes this error and provides the required duty ratio for the converter as its output. Utilizing a PI controller allows for gradual adjustment of the duty ratio and acts as a filter to cancel the effect of small noises. The system can be modeled and analyzed using small-signal analysis and control theory.

3.1.2.1 Small-Signal Analysis

To support the PI-based Maximum Power Point Tracking (MPPT) and ensure robust dynamic behaviour, a small-signal analysis is developed for the boost integrated stage, which serves as the interface between the PV source and the CLL resonant stage. For this analysis, the CLL resonant stage and the voltage doubler rectifier are modeled as an equivalent resistance, as shown in Figure 3.3. This is a valid approximation due to the filtering characteristics of the downstream stages, which cause the load to appear nearly constant from the perspective of the boost stage.

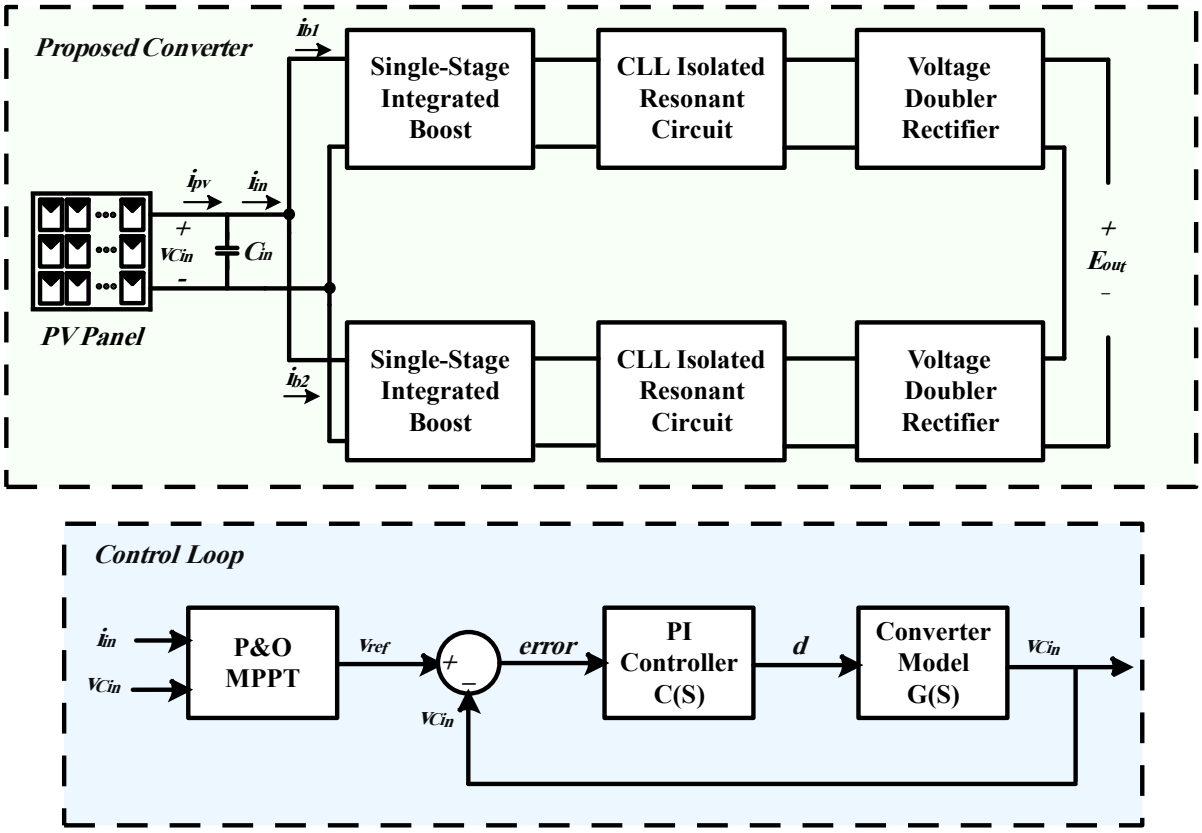

Figure 3.2- Overall block diagram of the proposed converter system with PI-based MPPT control loop

The primary objective of the small-signal analysis is to linearize the converter's nonlinear equations around a known steady-state operating point, resulting in a transfer function that describes how certain parameters vary in response to small changes in the control input. While the traditional small-signal analysis of boost converters in the literature usually obtains the output voltage to duty ratio transfer function, in this section, a different approach is taken. Because the controller adjusts the duty ratio to extract the maximum power from the PV panel, this analysis derives the transfer function of input voltage with respect to duty to examine how small variations in the duty ratio influence the input voltage. Understanding this relationship is fundamental for analyzing the dynamic characteristics of the converter, such as stability, transient response, and PI controller design.

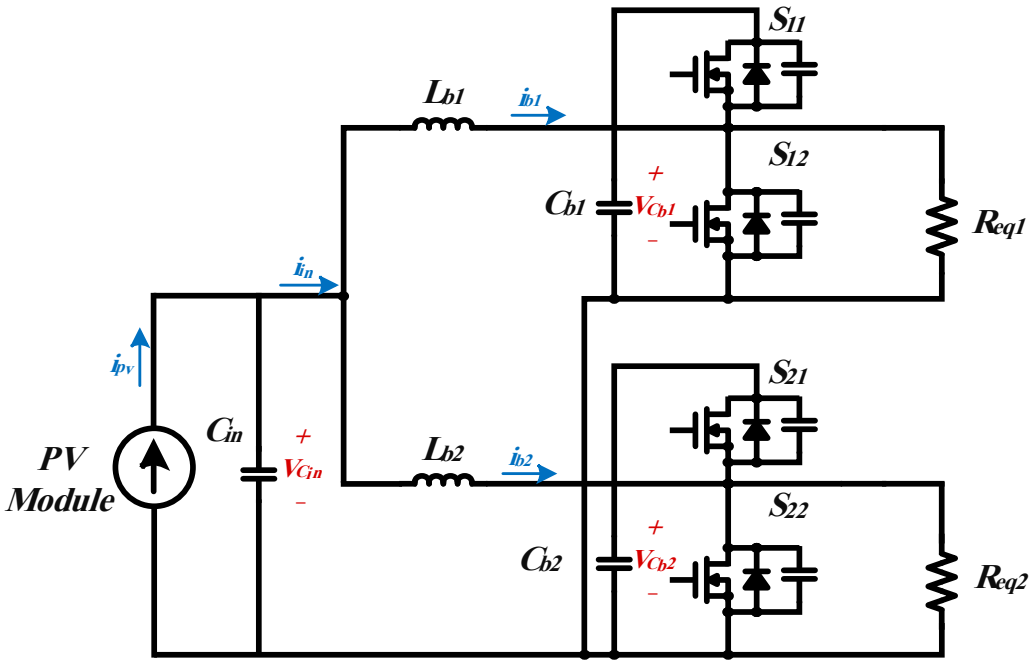

Figure 3.3- Equivalent single-stage integrated boost circuit

In this analysis, the following assumptions are made:

- PV module is modelled as a current source
- Boost stage output voltage is considered constant
- Converter is in CCM operation
- Two modules are identical

In the first step, the inductor current and input capacitor voltage (input voltage) are considered as state variables. The following equations for both modules ($n=1,2$) can be derived for the two switching stages of the boost converter.

When S_{n2} is on and S_{n1} is off:

$$\frac{di_{b1}(t)}{dt} = \frac{v_{Cin}}{L_{b1}} \tag{3.1}$$

$$\frac{di_{b2}(t)}{dt} = \frac{v_{Cin}}{L_{b2}} \tag{3.2}$$

When S_{n2} is off and S_{n1} is on:

$$\frac{di_{b1}(t)}{dt} = \frac{v_{Cin} - v_{Cb1}}{L_{b1}} \tag{3.3}$$

$$\frac{di_{b2}(t)}{dt} = \frac{v_{Cin} - v_{Cb2}}{L_{b2}} \tag{3.4}$$

And the following equation is true in both stages.

$$\frac{dv_{Cin}(t)}{dt} = \frac{1}{C_{in}} \left(i_{pv}(t) - i_{in}(t)\right) \tag{3.5}$$

$$i_{in}(t) = i_{b1}(t) + i_{b2}(t) \tag{3.6}$$

Next, a weighted average over one switching period T is taken, using d as the duty ratio of switch S_{n2}, assuming identical modules and constant voltage at the output of the boost stage ($v_{Cb1} = v_{Cb2} = V_o$).

$$\frac{di_{in}(t)}{dt} = \frac{di_{Lb1}(t)}{dt} + \frac{di_{Lb2}(t)}{dt} = 2\frac{v_{Cin}(t)}{L} - 2\frac{(1-d)}{L}V_o \tag{3.7}$$

$$L = L_{b1} = L_{B2} \tag{3.8}$$

By applying small perturbations around the steady-state values, as shown in (3.9) - (3.11), and substituting them into the averaged equations, the results are obtained in (3.12) and (3.13). Since the PV current is considered constant, the perturbation in PV current is ignored. After simplification and applying first-order approximation (neglecting products of small signal terms), the final small-signal state-space equations are derived, as shown in (3.14) and (3.15).

$$i_{in}(t) = I_{in} + \hat{\imath}_{in}(t) \tag{3.9}$$

$$v_{Cin}(t) = V_{Cin} + \hat{v}_{Cin}(t) \tag{3.10}$$

$$d(t) = D + \hat{d}(t) \tag{3.11}$$

$$\frac{d(I_{in} + \hat{\imath}_{in}(t))}{dt} = = 2\frac{V_{Cin} + \hat{v}_{Cin}(t)}{L} - 2\frac{\left(1 - (D + \hat{d}(t))\right)}{L}V_o \tag{3.12}$$

$$\frac{d(V_{Cin} + \hat{v}_{Cin}(t))}{dt} = \frac{1}{C_{in}}\left(I_{pv} - (I_{in} + \hat{\imath}_{in}(t))\right) \tag{3.13}$$

$$\frac{d\hat{\imath}_{in}(t)}{dt} = \frac{2}{L}(\hat{v}_{Cin}(t) + V_o\hat{d}(t)) \tag{3.14}$$

$$\frac{d\hat{v}_{Cin}(t)}{dt} = \frac{-1}{C}\hat{\imath}_{in}(t) \tag{3.15}$$

Applying the Laplace transform to the above equations and assuming zero initial conditions yields the following Laplace-domain equations.

$$s\hat{I}_{in}(S) = \frac{2}{L}(\hat{V}_c(S) + V_o\hat{D}(S)) \tag{3.16}$$

$$s\hat{V}_{Cin}(S) = \frac{-1}{C}\hat{I}_{in}(S) \tag{3.17}$$

Where:

$$\mathcal{L}\{\hat{\imath}_L(t)\} = \hat{I}_L(S) \tag{3.18}$$

$$\mathcal{L}\{\hat{v}_{Cin}(t)\} = \hat{V}_{Cin}(S) \tag{3.19}$$

$$\mathcal{L}\{\hat{d}(t)\} = \hat{D}(s) \tag{3.20}$$

By solving these two equations, the final transfer function is obtained.

$$G(S) = \frac{\hat{v}_{Cin}(S)}{\hat{D}(S)} = \frac{-2V_o}{S^2C_{in}L + 2} \tag{3.21}$$

3.1.2.2 PI Controller Design

After applying a pole-zero analysis to the small-signal transfer function $G(S)$, it is obvious that the boost converter stage shows a second-order behaviour with two imaginary poles, resulting in a marginally stable second-order response. The negative gain indicates that the PV panel voltage and the duty ratio have an inverse relationship, which is expected due to the characteristics of the boost converter. The location of the poles depends on the boost inductor and input capacitor. Figure 3.4 shows the root locus plot of the small-signal transfer function generated using *MATLAB* with $L=130\ \mu H$, $C_{in}=1\ \mu F$, and $V_o=400\ V$.

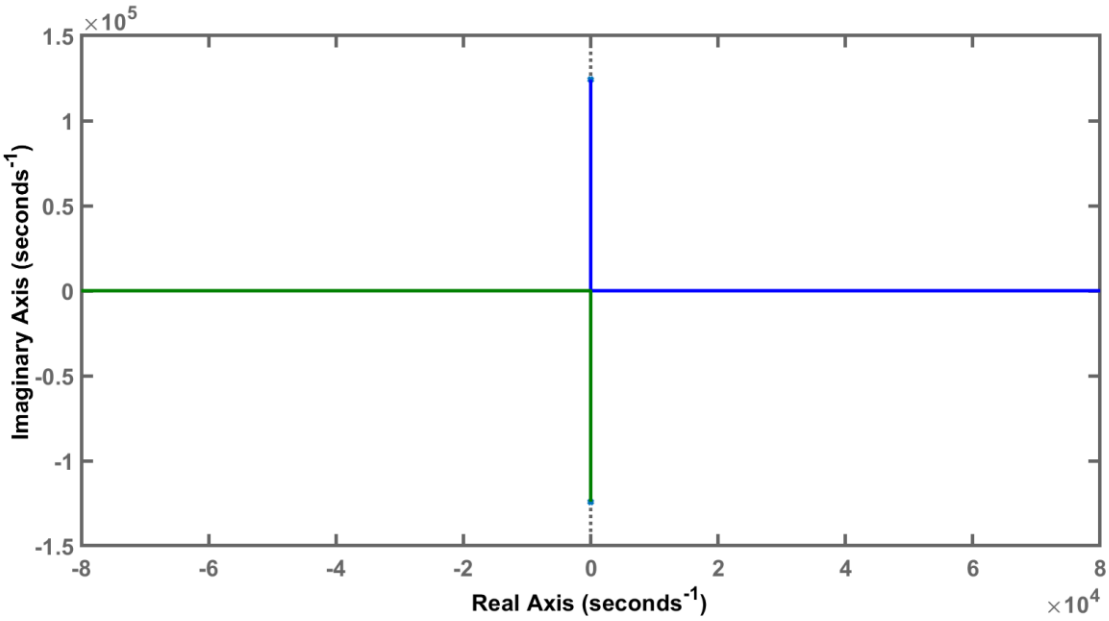

Figure 3.4- Root locus plot of the boost stage small-signal transfer function

To stabilize the system and improve transient performance, a PI controller with the following transfer function is considered.

$$C(S) = K_p + \frac{K_i}{S} = \frac{K_p(S + \frac{K_i}{K_p})}{S} \tag{3.22}$$

The controller adds a pole at the origin and a zero with a tunable location. To cancel the harmful effect of the pole at the origin, the zero should be placed close to the pole. The root locus plot of the system with the controller, defined by the following transfer function, is shown in Figure 3.5.

$$C(S) = K_p \frac{(S + 5000)}{S} \tag{3.23}$$
$$\frac{K_i}{K_p} = 5000$$

According to Figure 3.6, to achieve the damping ratio of $\zeta = 0.7$ and overshoot of $M_P = 5\%$, the desired proportional gain should be $K_p = 0.0027$. However, since this value is based on MATLAB simulations under ideal conditions, such a gain may be too aggressive for circuit simulation software and practical application. Therefore, a gain of $K_p = 0.001$ is used to ensure stability. The corresponding integral gain is then calculated as $K_i = 5$.

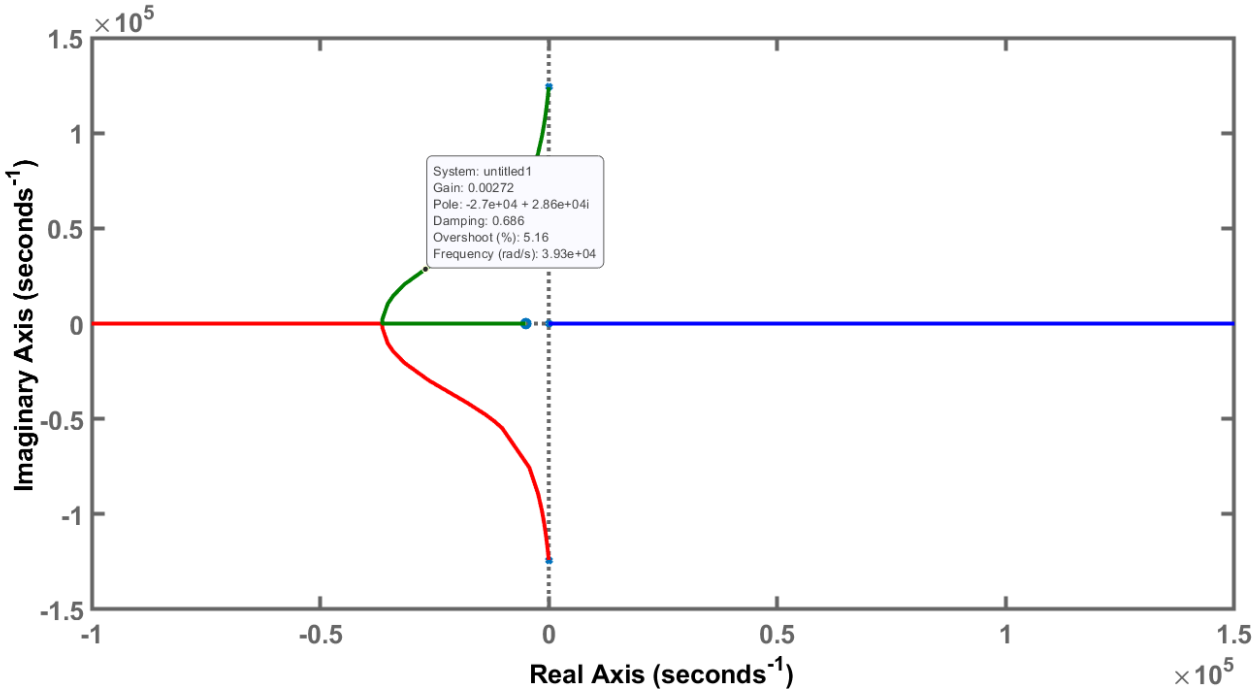

Figure 3.5- Root locus plot of the boost stage small-signal transfer function after adding the controller

3.2 Simulation Results

To demonstrate the operation of the proposed converter, a 1kW 100VDC to 2kVDC high-gain CLL converter with an integrated interleaved boost stage is simulated in the circuit simulation software PowerSim (PSIM). In this chapter, the converter is tested with a PV panel to verify the PI-based MPPT algorithm implemented using C-Block in the software. A PV array model with a maximum operating power of 330 W, MPP voltage of 30 V, and MPP current of 10 A was

configured using the Solar Module (physical model), consisting of 30 series-connected cells. The open circuit voltage and short circuit current were 40V and 11A, respectively. Note that the design procedure of the proposed circuit is similar to the one in Chapter 2.

To achieve higher power levels, the converter is tested using the same module but with 3×30 cells, with an operating frequency of 70 kHz. The duty ratio was controlled within the range of 10% to 80% by the closed-loop system. To validate the performance of the proposed converter under different operating conditions, three different light intensities were applied to the PV module. Figure 3.6 shows the performance of the controller in tracking the maximum power point and bringing the operating power close to it under 600W/m^2, 1000W/m^2, and 800W/m^2 light intensities.

The input and output voltages, switch currents, and voltage across switches are depicted in Figure 3.7 for both modules. The output voltage remains steady at 2kV with a 100V input, and ZVS operation is achieved under all conditions. Highlighted regions are enlarged for clarity.

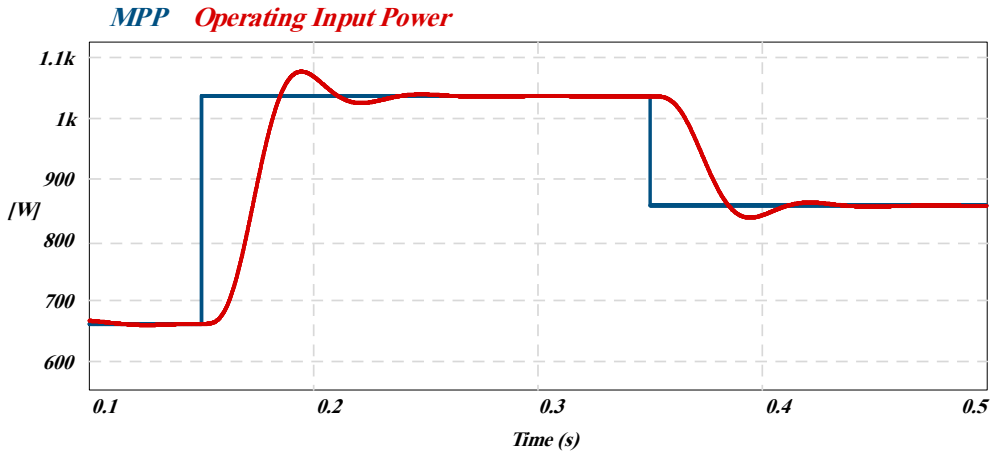

Figure 3.6- MPP and the operating input power of the converter

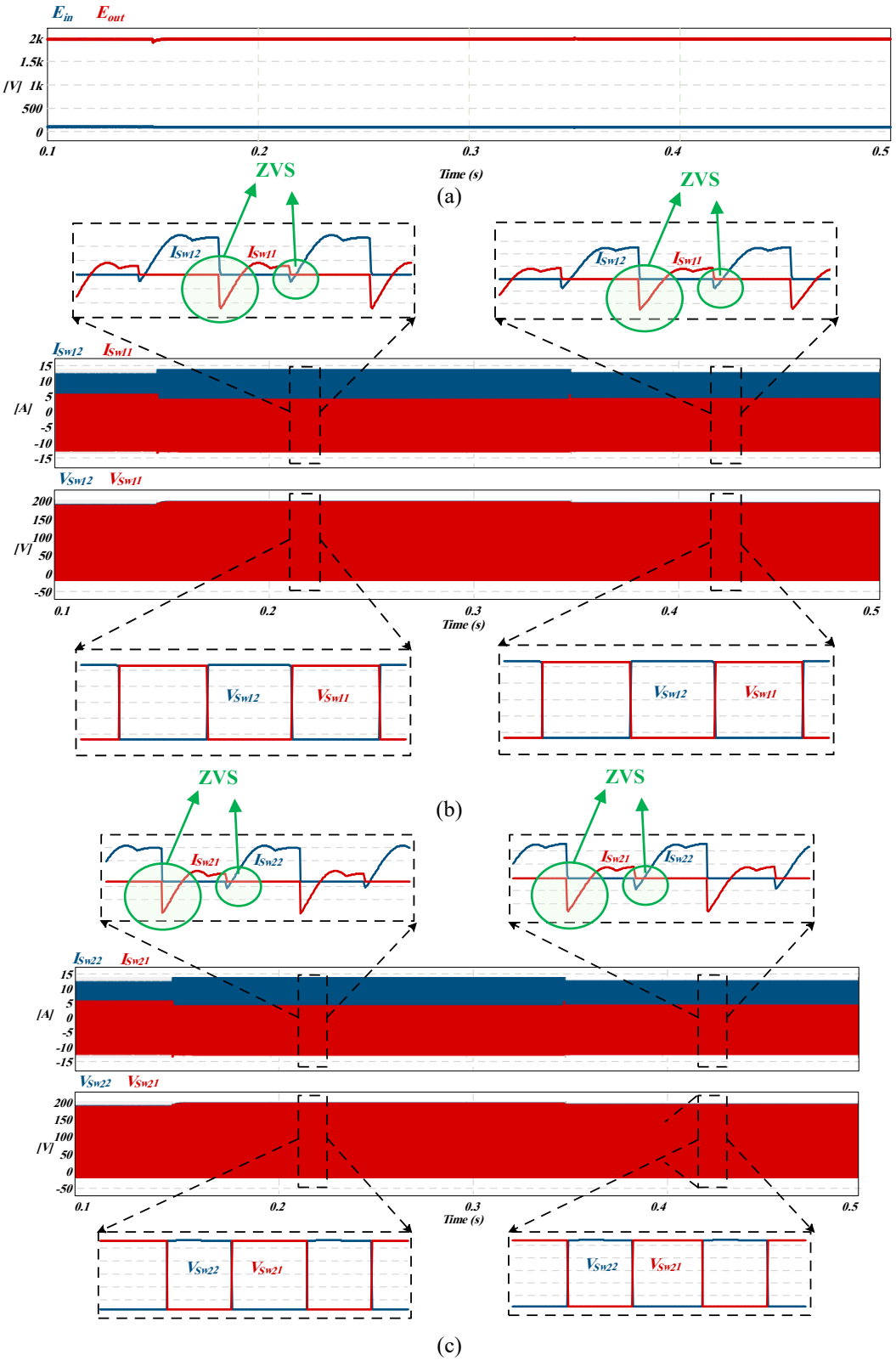

Figure 3.7- Operating waveforms of the 2 modules under different conditions (b) module I (c) module II

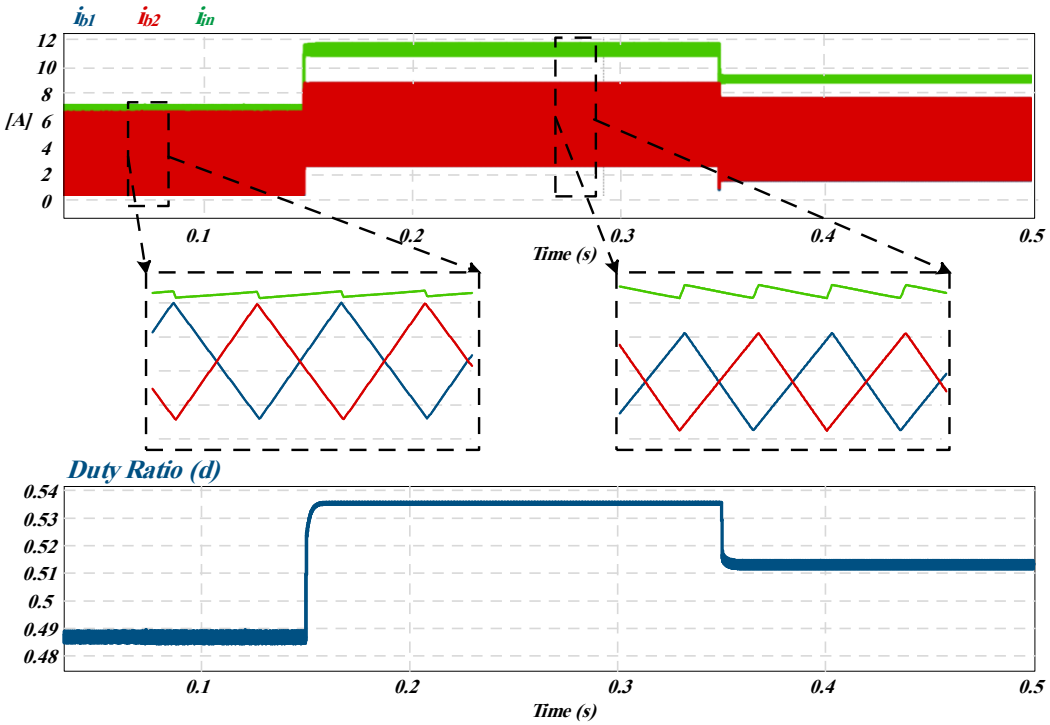

Figure 3.8- The boost current for both modules, the input current, and the duty ratio under all conditions

Figure 3.8 shows the integrated boost stage current for both modules, as well as the input current drawn from the PV module. The duty ratio under the three operating conditions is also demonstrated. The converter always operates in continuous conduction mode (CCM), and since the duty ratio range is around 0.5, the input current ripple remains very low. The selected areas are enlarged.

3.3 Experimental Results

To further verify the performance of the proposed high-gain converter and the MPPT controller, a scaled-down 150W 40VDC/660VDC proof-of-concept prototype, which its design procedure was presented in detail in Chapter 2, is tested using a PV emulator. An E4360A Modular Solar Array Simulator (SAS) was used to simulate the operating conditions of a PV array. The

discrete logic-based and PI-based MPPT algorithms were implemented on a (TMS)320F28335 DSP board using Texas Instruments Code Composer Studio (CCS) software. As mentioned earlier, the controller requires the PV voltage and current to implement the MPPT methods and control the duty ratio. Hence, input voltage and current sensing is necessary.

A simple voltage divider using a resistive bridge is implemented on the board to measure the voltage. This method offers a low-cost, low-loss solution compared to other voltage sensing techniques. Furthermore, a CAS 6-NP current transducer designed for precise measurement of AC, DC, and pulsed currents was used to measure the input current. This sensor has high accuracy, low offset, and fast response, making it an ideal option.

First, the converter is controlled by the logic-based MPPT algorithm and tested under different operating conditions. Figure 3.9 shows the input voltage, input current, and switch currents (Module 2 as an example), along with the operating power of the PV panel. The MPP changes every 5 seconds between 70W, 95W, and 120W. The controller adjusts the converter operating power by changing the duty ratio to track the highest power of the panel. Enlarged views of selected waveform regions are also presented. A low input current ripple is observed, and the system maintains soft-switching operation regardless of the operating condition.

Figure 3.10 illustrates the operating conditions of the PV emulator under different power levels. The MPP% is located at the top right of each figure, confirming that the extraction efficiency is above 99% in all scenarios.

Subsequently, the same tests were performed with the PI-based MPPT algorithm implemented on the controller. Figure 3.11 shows similar operating waveforms where the

maximum power point changes every 5 seconds between 65W, 80W, and 95W. A low ripple of the input current is observed, and the system maintains soft-switching operation regardless of the operating condition.

Figure 3.12 illustrates the operating conditions of the PV emulator controlled by PI-based MPPT under different power levels. The MPP% is located at the top right of each figure, confirming that the extraction efficiency is above 99% in all scenarios.

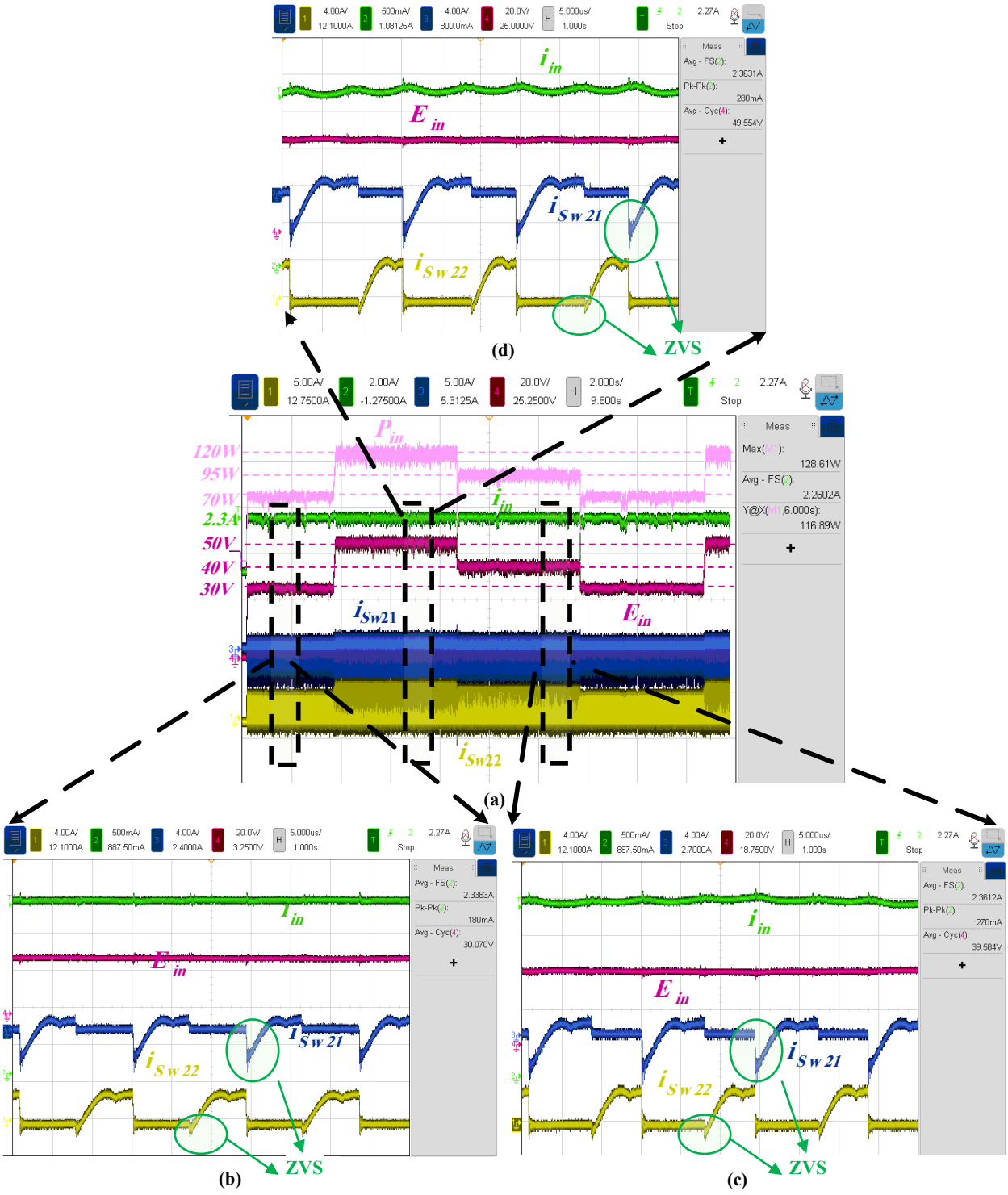

Figure 3.9- Converter operating waveforms controlled by logic-based MPPT under 3 different operating power, including (b)70W, (c) 95W, and (d)120W

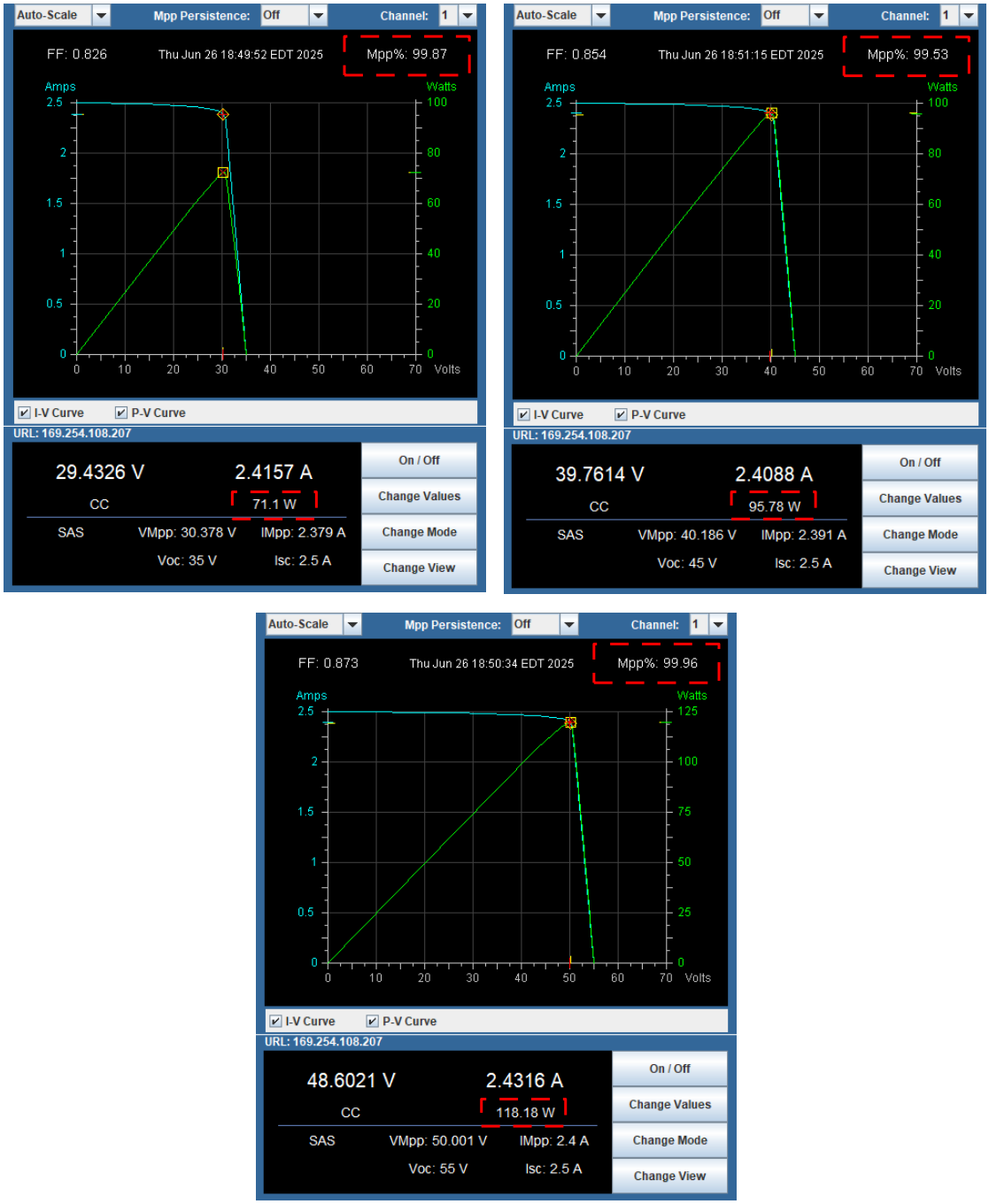

Figure 3.10- Logic-based controlled solar emulator MPPT display at (a) 70W, (b) 95W and (c) 120W

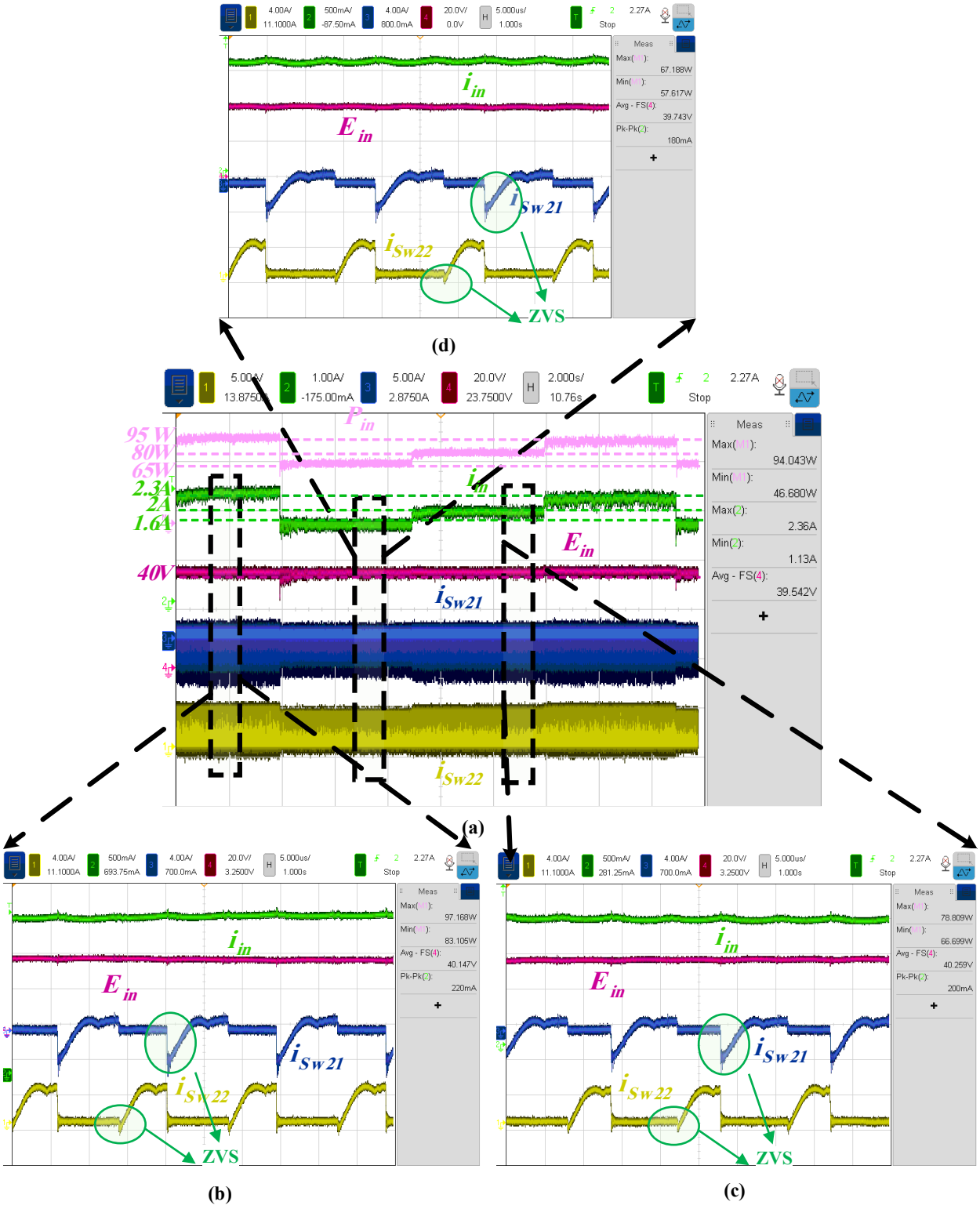

Figure 3.11- Converter operating waveforms controlled by PI-based MPPT under 3 different operating power, including (b) 95W, (c) 80W, and (d) 65W

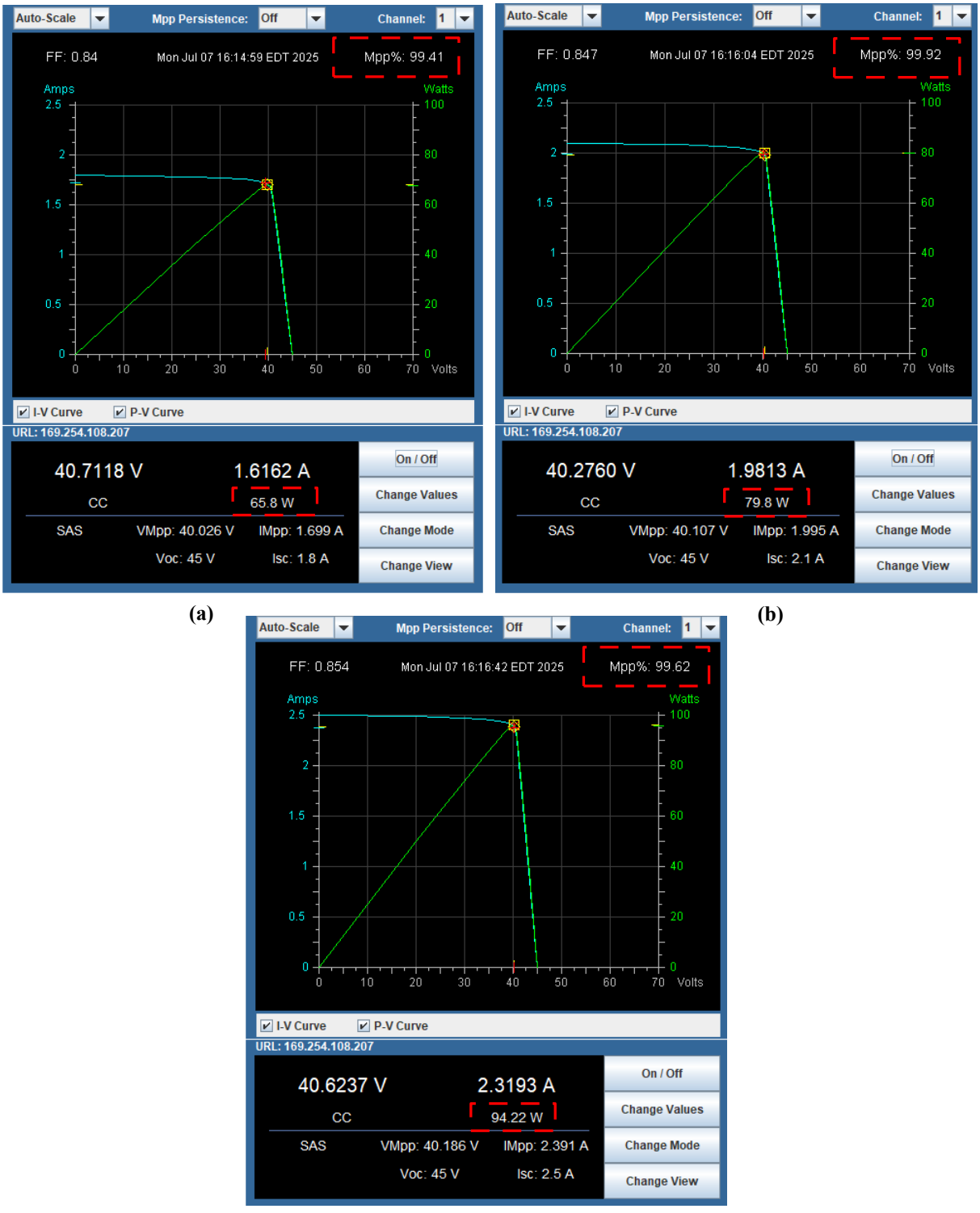

Figure 3.12- PI-based controlled solar emulator MPPT display at (a) 65W, (b) 80W and (c) 95W

To highlight the advantages of the proposed design, a comparison of several magnetron resonant power supplies is provided in Table 3.1. Considering the other topologies, the proposed converter utilizes only two switches per module, making it the lowest switch count among them. This low switch count simplifies the control scheme, reduces losses, and improves reliability. Furthermore, unlike most of the others that rely on a high number of transformers with complex design and high turns ratio, the proposed system uses a single transformer with a *1:2* turns ratio, enabling simple magnetic design while achieving high voltage gain. Also, the voltage gain of the converter is one of the highest, while being able to achieve higher gains by increasing the number of modules. Among all the designs, the proposed system is the only one explicitly designed to integrate with photovoltaic (PV) sources, making it unique for sustainable energy applications.

Table 3.1- Comparison of high-gain magnetron power supplies

Design (1 module)	**Switch count**	**Transformers**	**f_s (kHz)**	**In / Out Voltage (Hardware)**	**Gain**	**Efficiency**	**PV Integration**
[22]	4	1 (1:*n*:*n*:*n*)	>100	0.8kV / 2.5kV	≈3	98.6%	No
[35]	8	6 (1:*k*)	40-150	3.5kV / 10kV	≈3	96.5%	No
[36]	4	3 (1:4:4)	50	0.3kV / 2.5kV	≈8.5	-	No
[40]	6	3 (1:20)	20-130	- / 20kV	-	98%	No
Proposed	2	1 (1:2)	70	40V / 330V	≈8.5	98%	Yes

3.4 Chapter Summary

This chapter presented the implementation and validation of maximum power point tracking (MPPT) control strategies to interface with the designed interleaved boost-integrated CLL resonant converter with photovoltaic (PV) systems. Two MPPT methods using the Perturb and Observe (P&O) algorithm were provided: a discrete logic controller and a PI controller. While the first method is simpler to implement, the PI-based control offers smoother response and improved robustness against noise. To support the PI-based scheme, the integrated boost stage was modeled using a small-signal model. This enabled the derivation of the duty ratio to the PV input voltage transfer function, which is an important aspect in designing the control system. Through the analysis, a Proportional-Integral (PI) controller was designed to regulate the PV operating voltage with respect to the MPP reference. The operation of the converter was validated through simulation in PSIM under various irradiance levels and hardware experiments with a PV emulator and DSP-based controller. Both methods demonstrated high MPPT accuracy of over 99%, and stable ZVS operation with a wide load range. Experiments on the 150W 40VDC/660VDC prototype confirmed the effectiveness of the proposed converter and control schemes in PV-based systems.

Chapter 4 Conclusion and Future Work

4.1 Conclusion

The growing demand for compact, efficient, and high-voltage power supplies in industrial and scientific applications like magnetron-based systems has motivated the research towards more sophisticated power electronic converter topologies. Moreover, these converters play an essential role in integrating renewable energy sources, like wind turbines and photovoltaic panels, due to the recent interest in sustainable technologies. Because of their low voltage output and the requirement for the highest power extraction, photovoltaic (PV) sources have some integration challenges. To mitigate these challenges, this thesis presented a novel high step-up resonant DC-DC converter topology as a solution for magnetron power supplies fed by PV panels to address both power conversion and control challenges.

The contributions of this dissertation are summarized below:

1. The main contribution of this research involves the design and development of a high-gain soft-switching M-module interleaved DC/DC converter. Each module is a result of combining four conventional step-up stages, including a boost stage, a half-bridge inverter, a CLL resonant tank and a voltage doubler rectifier. The boost and inverter stages are combined into a single stage. The structure enables high voltage gain together with low current ripple and soft-switching (ZVS/ZCS) for all switches and diodes, which are essential for the reliable and efficient operation of

high-voltage loads such as magnetrons. The interleaved operation technique decreases component stress while enabling continuous current mode (CCM) operation with low input ripple, which enhances both efficiency and electromagnetic compatibility

2. A novel system for magnetron power supplies is presented. This system utilizes the proposed interleaved converter integrated with PV panels. The proposed converter is compatible with maximum power tracking (MPPT), considering its low ripple input current.
3. Two maximum power point tracking (MPPT) methods were implemented to connect the converter to the PV source: a discrete logic-based method and a PI-based voltage regulation scheme using duty ratio control. The converter demonstrated its performance according to both simulation and experimental testing results. The hardware prototype underwent initial testing with a DC source to verify both high voltage gain and soft-switching operation. Then, a PV emulator was used to test the system, achieving successful MPPT operation at more than 99% accuracy throughout various operating scenarios.
4. A small-signal model of the interleaved boost stage was developed to design the PI controller. The research focused on studying how changes in duty ratio affect the input voltage instead of concentrating on output voltage variations, like most existing studies.

4.2 Future Work

Some future works relating to this research are summarized below:

1. Although a logic-based and PI-based MPPT controller were successfully implemented, further work can be focused on implementing and testing advanced adaptive control algorithms such as fuzzy logic, sliding mode control, or machine learning–based MPPT. These methods can improve tracking speed and stability under highly dynamic environmental conditions.
2. The current hardware prototype was limited to a proof-of-concept scale and tested by a PV emulator and resistors as an equivalent load for the magnetron. Future research can scale up the design for higher power levels using a real domestic or industrial magnetron. Also, the setup can be tested with PV arrays in an environment similar to the desired application. This will allow for the evaluation of the converter's performance in real-world industrial or renewable energy systems, including compliance with power quality standards and safety regulations.
3. Another potential extension of this work is the integration of an energy storage system (ESS) with the current topology using a bidirectional DC/DC converter. Adding an ESS would improve the system reliability by compensating energy during shading or nighttime. The research could investigate the possible control strategies for MPPT operation and battery management, alongside the design of a high-efficiency bidirectional converter for this application.
4. At high power levels, thermal considerations are dominant. Future work must include a detailed thermal model and experimental study of heat dissipation through the switching and passive components. The study of long-term reliability and possible component aging due to thermal stress and electrical transients will be mandatory for industrial applications.

5. The designed converter currently operates unidirectionally as a power supply for the magnetron. However, this topology can be used for grid-connected applications. A promising research direction is to modify the topology for bidirectional power. This would enable the system to not only extract power from sources like PV but also to return power to the source or grid, which is vital for applications in smart grids and microgrids.

References

[1] Jones, Graham A.; Layer, David H.; Osenkowsky, Thomas G. (2013). National Association of Broadcasters Engineering Handbook, 10th Ed. Focal Press. p. 6. ISBN 978-1136034107.

[2] T. B. R. Company, "Microwave Devices Global Market Report," 2025. [Online]. Available: https://www.thebusinessresearchcompany.com/report/microwave-devices-global-market-report.

[3] W. C. Brown, "The microwave magnetron and its derivatives," *in IEEE Transactions on Electron Devices*, vol. 31, no. 11, pp. 1595-1605, Nov. 1984, doi: 10.1109/T-ED.1984.21757.

[4] C. G. B, Microwave Magnetrons, New York: Mcgraw-hill Book Company Inc., 1948.

[5] J. C. S, Microwave Electronics: Dover Books, 1950.

[6] Y. Liu et al., "A Dual-Output Power Supply Integrated High -Voltage Anode Power Supply and Filament Power Supply for Magnetrons," in IEEE Transactions on Industrial Electronics, vol. 71, no. 5, pp. 4629-4639, May 2024, doi: 10.1109/TIE.2023.3288204.

[7] H. A. H. Boot and J. T. Randall, "Historical notes on the cavity magnetron," in *IEEE Transactions on Electron Devices*, vol. 23, no. 7, pp. 724-729, July 1976, doi: 10.1109/T-ED.1976.18476.

[8] M. Heggannavar and H. Kulkarni, "Power supply design for Magnetron power source from single phase supply," *2015 International Conference on Energy Systems and Applications*, Pune, India, 2015, pp. 546-551, doi: 10.1109/ICESA.2015.7503409.

[9] M. Heggannavar and H. Kulkarni, "Design of Magnetron power source from three phase supply," *2015 International Conference on Energy Systems and Applications*, Pune, India, 2015, pp. 552-556, doi: 10.1109/ICESA.2015.7503410.

[10] M. Brady and M. Edwards, "Developments in marine radar magnetrons," *2010 International Conference on the Origins and Evolution of the Cavity Magnetron*, Bournemouth, UK, 2010, pp. 58-63, doi: 10.1109/CAVMAG.2010.5565565.

[11] Y. Zhou, Y. Zhang, H. Zhu and Y. Yang, "Study of the Influence of Power Supply Ripple on Magnetron's Output Spectrum," in *IEEE Transactions on Electron Devices*, vol. 68, no. 9, pp. 4698-4704, Sept. 2021, doi: 10.1109/TED.2021.3097317.

[12] J. -Y. Lee, M. -K. Choi, H. -B. Jo and H. -J. Ryoo, "Comparative Study of High-Voltage Isolated Filament Power Supply for Driving a High-Power Magnetron," in *IEEE Transactions on Plasma Science*, vol. 52, no. 7, pp. 2699-2705, July 2024, doi: 10.1109/TPS.2024.3445126.

[13] Haitham B. Al-Wakeel, Z.A. Abdul Karim, Hussain H. Al-Kayiem, M.H. Mat Jamlus, "Soot Reduction Strategy: A Review". *Journal of Applied Sciences, 2012*, 12: 2338–2345, doi:10.3923/jas.2012.2338.2345

[14] A. I. Zemtsov, I. I. Artyukhov, S. F. Stepanov, E. E. Mirgorodskaya, N. P. Mityashin and N. A. Kalistratov, "Modeling and simulation of a low power magnetron as an element of electrical system," *2018 28th International Conference Radioelektronika (RADIOELEKTRONIKA),* Prague, 2018, pp. 1-5, doi: 10.1109/RADIOELEK.2018.8376358.

[15] J. M. Carrasco *et al*., "Power-Electronic Systems for the Grid Integration of Renewable Energy Sources: A Survey," in *IEEE Transactions on Industrial Electronics*, vol. 53, no. 4, pp. 1002-1016, June 2006, doi: 10.1109/TIE.2006.878356.

[16] B. -M. Song, M. -H. Kye and R. -Y. Kim, "Design of a cost-effective DC-DC converter with high power density for magnetron power supplies," *The 2010 International Power Electronics Conference* - ECCE ASIA -, Sapporo, Japan, 2010, pp. 137-141, doi: 10.1109/IPEC.2010.5543855.

[17] J. . -S. Lai, B. M. Song, R. Zhou, A. R. Hefner, D. W. Berning and C. . -C. Shen, "Characteristics and utilization of a new class of low on-resistance MOS-gated power device," *Conference Record of the 1999 IEEE Industry Applications Conference. Thirty-Forth IAS Annual Meeting* (Cat. No.99CH36370), Phoenix, AZ, USA, 1999, pp. 1073-1079 vol.2, doi: 10.1109/IAS.1999.801637.

[18] Zhenxian Liang, Bing Lu, J. D. van Wyk and F. C. Lee, "Integrated CoolMOS FET/SiC-diode module for high performance power switching," in *IEEE Transactions on Power Electronics*, vol. 20, no. 3, pp. 679-686, May 2005, doi: 10.1109/TPEL.2005.846547.

[19] S. K. Mazumder, K. Acharya and C. M. Tan, "Design of an All-SiC Radio-frequency Controlled Parallel DC-DC Converter Unit," *2007 IEEE Power Electronics Specialists Conference*, Orlando, FL, USA, 2007, pp. 2833-2839, doi: 10.1109/PESC.2007.4342468.

[20] N. Mohan, T. M. Undeland, and W. P. Robbins, Power Electronics: Converters, Applications, and Design, 3rd ed. Hoboken, NJ, USA: Wiley, 2002.

[21] M. Forouzesh, Y. P. Siwakoti, S. A. Gorji, F. Blaabjerg and B. Lehman, "Step-Up DC–DC Converters: A Comprehensive Review of Voltage-Boosting Techniques, Topologies, and Applications," in *IEEE Transactions on Power Electronics*, vol. 32, no. 12, pp. 9143-9178, Dec. 2017, doi: 10.1109/TPEL.2017.2652318.

[22] J. Zhang *et al*., "Design and Optimization of a Magnetron DC–DC Isolated Power Supply With High Efficiency," in *IEEE Transactions on Power Electronics*, vol. 37, no. 8, pp. 9392-9405, Aug. 2022, doi: 10.1109/TPEL.2022.3155257.

[23] S. -R. Jang, H. -J. Ryoo, S. -H. Ahn, J. Kim and G. H. Rim, "Development and Optimization of High-Voltage Power Supply System for Industrial Magnetron," in *IEEE Transactions on Industrial Electronics*, vol. 59, no. 3, pp. 1453-1461, March 2012, doi: 10.1109/TIE.2011.2163915.

[24] N. A. Abodhir, A. J. Watson and J. C. Clare, "Control of high voltage series resonant power supply for industrial magnetrons," *7th IET International Conference on Power Electronics, Machines and Drives (PEMD 2014)*, Manchester, UK, 2014, pp. 1-6, doi: 10.1049/cp.2014.0398.

[25] Z. Li and Z. Liu, “Preparation of few-layer graphene by annealing Ni_3C film deposited by high power impulse magnetron sputtering,” in *Proc. 2024 IEEE Int. Conf. Plasma Sci. (ICOPS)*, Beijing, China, Jun. 2024, pp. 909–910.

[26] A. Alzahrani, M. Ferdowsi, and P. Shamsi, “A family of scalable non-isolated interleaved DC-DC boost converters with voltage multiplier cells,” *IEEE Access*, vol. 7, pp. 11707–11721, 2019, doi: 10.1109/ACCESS.2019.2891625. Performance Analysis of Voltage Multiplier Coupled Cascaded Boost Converter With Solar PV Integration for DC Microgrid Application

[27] Seshagiri Rao Vemparala and Sundaramoorthy Kumaravel, “Performance Analysis of Voltage Multiplier Coupled Cascaded Boost Converter With Solar PV Integration for DC Microgrid Application,” *IEEE Trans Ind Appl*, vol. 59, no. 1, pp. 10131–1023, Sep. 2023.

[28] P. Mohseni, S. Mohammadsalehian, M. R. Islam, K. M. Muttaqi, D. Sutanto, and P. Alavi, “Ultrahigh Voltage Gain DC-DC Boost Converter with ZVS Switching Realization and Coupled Inductor Extendable Voltage Multiplier Cell Techniques,” *IEEE Transactions on*

Industrial Electronics, vol. 69, no. 1, pp. 323–335, Jan. 2022, doi: 10.1109/TIE.2021.3050385

[29] A. Alzahrani, M. Ferdowsi, and P. Shamsi, “High-Voltage-Gain DC-DC Step-Up Converter with Bifold Dickson Voltage Multiplier Cells,” *IEEE Trans Power Electron*, vol. 34, no. 10, pp. 9732–9742, Oct. 2019, doi: 10.1109/TPEL.2018.2890437.

[30] Kumar Amit, Awasthi Abhishek, Salari Omid, Bagawade Snehal, and P. Jain, “A Novel Time Domain Analysis of the LLC-L Resonant Converter for the Use of the CLL and LLC Resonant Converter,” in *2019 IEEE Applied Power Electronics Conference and Exposition (APEC)*, 2019, pp. 3453–3460.

[31] R. L. Steigerwald, "A comparison of half-bridge resonant converter topologies," in *IEEE Transactions on Power Electronics*, vol. 3, no. 2, pp. 174-182, April 1988, doi: 10.1109/63.4347.

[32] S.-Y. Yu, R. Chen, and A. Viswanathan, “Survey of Resonant Converter Topologies,” Dallas, 2018. [Online]. Available: www.ti.com/psds

[33] D. J. Tschirhart and P. K. Jain, “A CLL resonant asymmetrical pulsewidth-modulated converter with improved efficiency*,” IEEE Transactions on Industrial Electronics*, vol. 55, no. 1, pp. 114–122, Jan. 2008, doi: 10.1109/TIE.2007.906176.

[34] M. T. Outeiro, G. Buja, and D. Czarkowski, “Resonant Power Converters: An Overview with Multiple Elements in the Resonant Tank Network,” *IEEE Industrial Electronics Magazine*, vol. 10, no. 2, pp. 21–45, Jun. 2016, doi: 10.1109/MIE.2016.2549981.

[35] Y. Liu *et al*., "A Multimode Wide Output Range High-Voltage Power Supply for Magnetrons," in *IEEE Transactions on Industrial Electronics*, vol. 70, no. 11, pp. 11153-11162, Nov. 2023, doi: 10.1109/TIE.2022.3225803.

[36] S. -W. Choi, I. -O. Lee and J. -Y. Lee, "Design of 5-kV/5-kW Magnetron Power Supply Using PWM SRC With PISO-Connected Transformer," in *IEEE Transactions on Plasma Science*, vol. 46, no. 8, pp. 2840-2847, Aug. 2018, doi: 10.1109/TPS.2018.2854892.

[37] M. Bakalian and J. Lam, "Dual CL/LLC DC/DC Resonant Circuit Modules For Step-up Power Interface in Microwave Magnetron Application," *2022 IEEE 1st Industrial Electronics Society Annual On-Line Conference (ONCON)*, kharagpur, India, 2022, pp. 1-5, doi: 10.1109/ONCON56984.2022.10126886.

[38] M. Bakalian and J. Lam, "A Double-Output Soft-Switched Step-Up AC/DC Bridge-Less Converter for Microwave Energy Application," *IECON 2021 – 47th Annual Conference of the IEEE Industrial Electronics Society*, Toronto, ON, Canada, 2021, pp. 1-6, doi: 10.1109/IECON48115.2021.9589055.

[39] R. Hou *et al*., "Optimization and Design of LCC Resonant High-Voltage Wide Range Power Supply for Magnetrons," in *IEEE Journal of Emerging and Selected Topics in Power Electronics*, vol. 12, no. 4, pp. 3835-3847, Aug. 2024, doi: 10.1109/JESTPE.2024.3412800.

[40] S. -H. Ahn, H. -J. Ryoo, J. -W. Gong and S. -R. Jang, "Low-Ripple and High-Precision High-Voltage DC Power Supply for Pulsed Power Applications," in *IEEE Transactions on Plasma Science*, vol. 42, no. 10, pp. 3023-3033, Oct. 2014, doi: 10.1109/TPS.2014.2333813.

[41] B. K. Bose, "Global Warming: Energy, Environmental Pollution, and the Impact of Power Electronics," in *IEEE Industrial Electronics Magazine*, vol. 4, no. 1, pp. 6-17, March 2010, doi: 10.1109/MIE.2010.935860.

[42] REN21, “The First Decade : 2004 – 2014,” Jun. 2019. [Online]. Available: https://www.ren21.net/the-first-decade-2004-2014/

[43] N. M. Haegel and S. R. Kurtz, "Global Progress Toward Renewable Electricity: Tracking the Role of Solar," in *IEEE Journal of Photovoltaics*, vol. 11, no. 6, pp. 1335-1342, Nov. 2021, doi: 10.1109/JPHOTOV.2021.3104149

[44] M. Malinowski, J. I. Leon, and H. Abu-Rub, “Solar Photovoltaic and Thermal Energy Systems: Current Technology and Future Trends,” Proceedings of the IEEE, vol. 105, no. 11, pp. 2132–2146, Nov. 2017, doi: 10.1109/JPROC.2017.2690343.

[45] Kajanana Phd dessertation

[46] *1709-2018 - IEEE Recommended Practice for 1 kV to 35 kV Medium-Voltage DC Power Systems on Ships*. IEEE, 2018.

[47] J. W. Gajda, P. E. Duke, and O. Support, “Impacts to utility distribution systems Solar Farms: design & construction,” Raleigh, North Carolina. [Online]. Available: https://standards.ieee.org/wp content/uploads/import/documents/presentations/nesc_workshop__solar_farms design_construction.pdf

[48] Ma. Z, “Medium voltage direct current (MVDC) grid feasibility study,” CIGRE Digital Magazine.

[49] X. Li, Q. Wang, H. Wen and W. Xiao, "Comprehensive Studies on Operational Principles for Maximum Power Point Tracking in Photovoltaic Systems," in *IEEE Access*, vol. 7, pp. 121407-121420, 2019, doi: 10.1109/ACCESS.2019.2937100.

[50] S. H. Hanzaei, S. A. Gorji, and M. Ektesabi, “A scheme-based review of MPPT techniques with respect to input variables including solar irradiance and PV arrays’ temperature,” *IEEE Access*, vol. 8. Institute of Electrical and Electronics Engineers Inc., pp. 182229–182239, 2020. doi: 10.1109/ACCESS.2020.3028580.

[51] M. E. E. Telbany, A. Youssef, and A. A. Zekry, “Intelligent Techniques for MPPT Control in Photovoltaic Systems: A Comprehensive Review,” in Proceedings - *2014 4th International Conference on Artificial Intelligence with Applications in Engineering and Technology*, ICAIET 2014, Institute of Electrical and Electronics Engineers Inc., Dec. 2015, pp. 17–22. doi: 10.1109/ICAIET.2014.13.

[52] K. Y. Yap, C. R. Sarimuthu, and J. M. Y. Lim, “Artificial Intelligence Based MPPT Techniques for Solar Power System: A review,” *Journal of Modern Power Systems and Clean Energy*, vol. 8, no. 6, pp. 1043–1059, Nov. 2020, doi: 10.35833/MPCE.2020.000159.

[53] B. Subudhi and R. Pradhan, “A comparative study on maximum power point tracking techniques for photovoltaic power systems,” *IEEE Trans Sustain Energy*, vol. 4, no. 1, pp. 89–98, 2013, doi: 10.1109/TSTE.2012.2202294.

[54] Xiao Weidong and Elnosh Ammar, “Overview of Maximum Power Point Tracking Technologies for Photovoltaic Power Systems,” in *IEEE Industrial Electronics Society*, 2011, p. 4746.

[55] T. Esram and P. L. Chapman, “Comparison of photovoltaic array maximum power point tracking techniques,” *IEEE Transactions on Energy Conversion*, vol. 22, no. 2, pp. 439 449, Jun. 2007, doi: 10.1109/TEC.2006.874230.

[56] J. Dadkhah and M. Niroomand, “Optimization Methods of MPPT Parameters for PV Systems: Review, Classification, and Comparison,” *Journal of Modern Power Systems and Clean Energy*, vol. 9, no. 2. State Grid Electric Power Research Institute, pp. 225 236, Mar. 01, 2021. doi: 10.35833/MPCE.2019.000379.

[57] A. El Hibaoui, M. Essaaidi, Y. Zaz, International Solar Energy Society, and Institute of Electrical and Electronics Engineers, *Proceedings of 2019 7th International Renewable and Sustainable Energy Conference (IRSEC)*.

[58] M. Kumar, K. P. Panda, J. C. Rosas-Caro, A. Valderrabano-Gonzalez, and G. Panda, "Comprehensive Review of Conventional and Emerging Maximum Power Point Tracking Algorithms for Uniformly and Partially Shaded Solar Photovoltaic Systems," *IEEE Access*, vol. 11, pp. 31778–31812, 2023, doi: 10.1109/ACCESS.2023.3262502.

[59] T. T. N. Khatib, A. Mohamed, N. Amin, and K. Sopian, "An Efficient Maximum Power Point Tracking Controller for Photovoltaic Systems Using New Boost Converter Design and Improved Control Algorithm.

[60] R. B. Bollipo, S. Mikkili, and P. K. Bonthagorla, "Hybrid, optimal, intelligent and classical PV MPPT techniques: A review," *CSEE Journal of Power and Energy Systems*, vol. 7, no. 1. Institute of Electrical and Electronics Engineers Inc., pp. 9–33, Jan. 01, 2021. doi: 10.17775/CSEEJPES.2019.02720.

[61] R. Patil and H. Anantwar, "Comparitive analysis of fuzzy based MPPT for buck and boost converter topologies for PV application," *2017 International Conference On Smart Technologies For Smart Nation (SmartTechCon)*, Bengaluru, India, 2017, pp. 1479-1484, doi: 10.1109/SmartTechCon.2017.8358610.

[62] X. Li and H. Wen, "A fuzzy logic controller with beta parameter for maximum power point tracking of Photovoltaic systems," *2016 IEEE 8th International Power Electronics and Motion Control Conference (IPEMC-ECCE Asia)*, Hefei, China, 2016, pp. 1550-1555, doi: 10.1109/IPEMC.2016.7512522.

[63] N. Priyadarshi, S. Padmanaban, P. Kiran Maroti and A. Sharma, "An Extensive Practical Investigation of FPSO-Based MPPT for Grid Integrated PV System Under Variable Operating Conditions With Anti-Islanding Protection," in *IEEE Systems Journal*, vol. 13, no. 2, pp. 1861-1871, June 2019, doi: 10.1109/JSYST.2018.2817584

[64] L. P. N. Jyothy and M. R. Sindhu, "An Artificial Neural Network based MPPT Algorithm For Solar PV System," *2018 4th International Conference on Electrical Energy Systems (ICEES)*, Chennai, India, 2018, pp. 375-380, doi: 10.1109/ICEES.2018.8443277.

[65] J. S. Smith, B. Wu and B. M. Wilamowski, "Neural Network Training With Levenberg–Marquardt and Adaptable Weight Compression," in *IEEE Transactions on Neural*

Networks and Learning Systems, vol. 30, no. 2, pp. 580-587, Feb. 2019, doi: 10.1109/TNNLS.2018.2846775.

[66] Mohamed Lasheen, Mazen Abdel-Salam, Maximum power point tracking using Hill Climbing and ANFIS techniques for PV applications: A review and a novel hybrid approach, *Energy Conversion and Management*, Volume 171,2018,Pages 1002-1019,ISSN 0196-8904,https://doi.org/10.1016/j.enconman.2018.06.003.

[67] M. Rolevski and Ž. Zečević, "MPPT controller based on the neural network model of the photovoltaic panel," *2020 24th International Conference on Information Technology (IT)*, Zabljak, Montenegro, 2020, pp. 1-4, doi: 10.1109/IT48810.2020.9070299.

[68] T. Sutikno, W. Arsadiando, A. Wangsupphaphol, A. Yudhana and M. Facta, "A Review of Recent Advances on Hybrid Energy Storage System for Solar Photovoltaics Power Generation," in *IEEE Access*, vol. 10, pp. 42346-42364, 2022, doi: 10.1109/ACCESS.2022.3165798.

[69] Tsai-Fu Wu and Te-Hung Yu, "Unified approach to developing single-stage power converters," in *IEEE Transactions on Aerospace and Electronic Systems*, vol. 34, no. 1, pp. 211-223, Jan. 1998, doi: 10.1109/7.640279.

Appendix A. Printed Circuit Board (PCB) Layouts

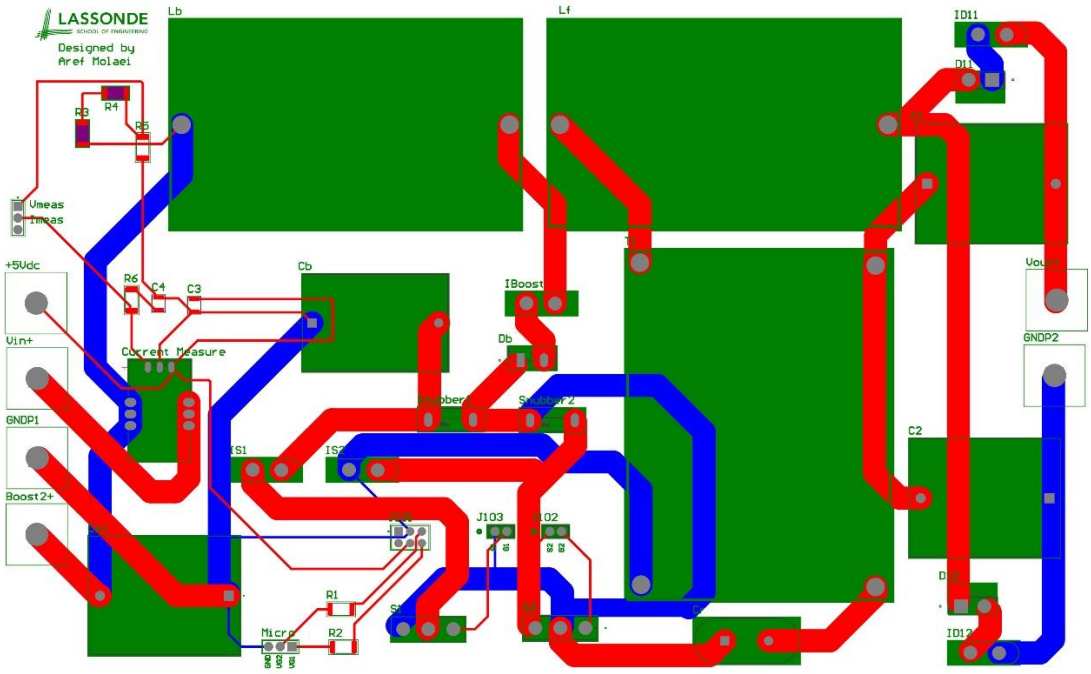

Figure A. 1- PCB layout of proposed converter module 2

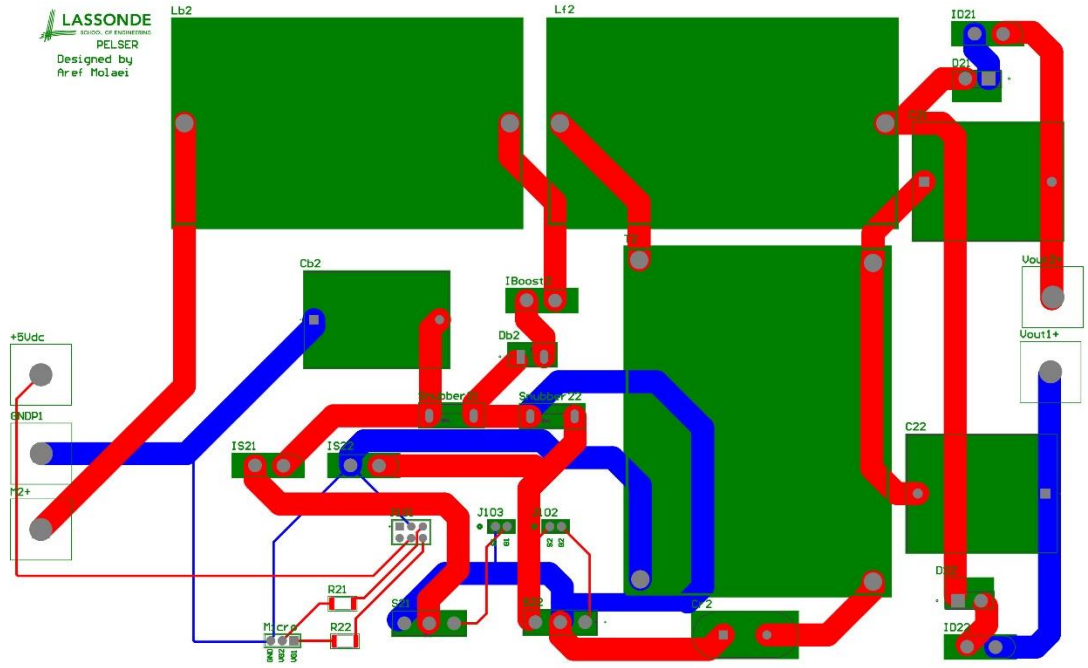

Figure A. 2- PCB layout of proposed converter module 1

Appendix B. PSIM Schematics

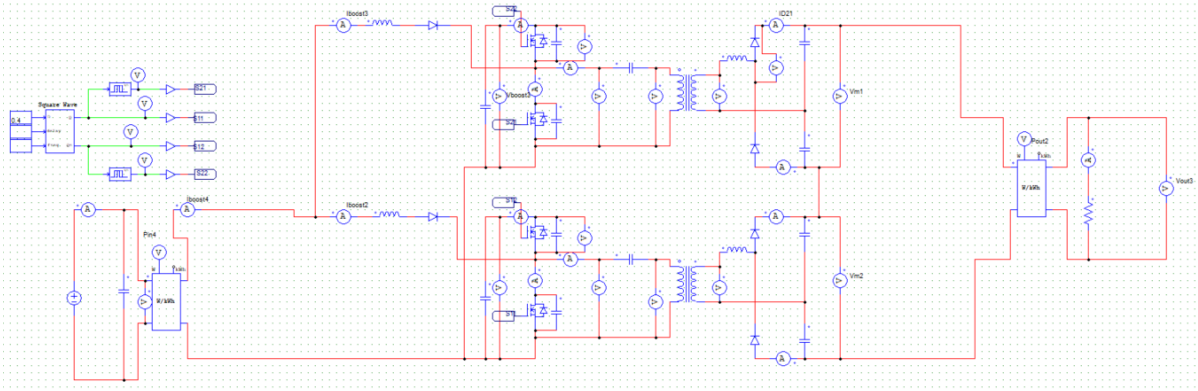

Figure B. 1- PSIM schematic of the proposed converter with two modules

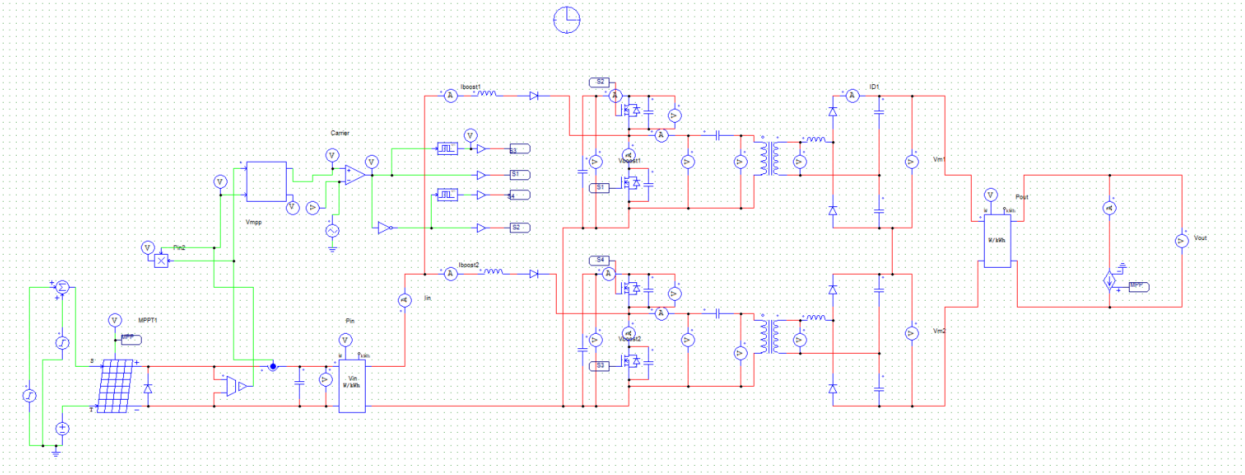

Figure B. 2- PSIM schematic of the proposed converter with two modules controlled by logic-based MPPT

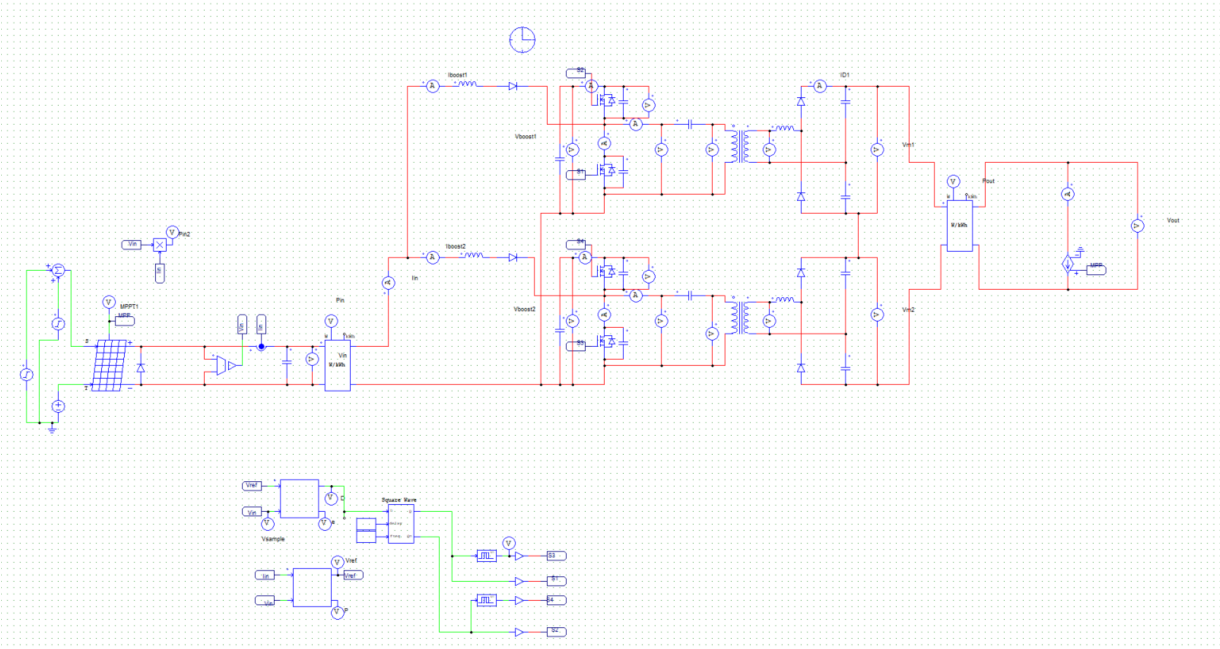

Figure B. 3- PSIM schematic of the proposed converter with two modules controlled by PI-based MPPT

Appendix C. DSP Code for Logic-based MPPT

```
// Function prototypes

void EPWM_Config(void);

void EPWM2_Config(void);


// ADC Configuration Macros

#if (CPU_FRQ_150MHZ)

  #define ADC_MODCLK 0x3  // 150/(2*3) = 25.0 MHz

#endif

#if (CPU_FRQ_100MHZ)

  #define ADC_MODCLK 0x2  // 100/(2*2) = 25.0 MHz

#endif


#define ADC_CKPS    0x5   // ADC clock prescaler

#define ADC_SHCLK   0x8   // Sample and Hold width = 16 ADC clocks

#define AVG         1000  // Averaging window

#define BUF_SIZE    1020  // ADC sample buffer size

#define freq        70000 // PWM switching frequency (Hz)
```

```
// Global Variables
Uint16 SampleTable1[BUF_SIZE];
Uint16 SampleTable2[BUF_SIZE];

double FinalV1 = 0, FinalI1 = 0;
double Vi = 0, Ii = 0;
int count = (150000000 / freq);

double P = 0, dP = 0, dV = 0, dI = 0;
double Pprev = 0, Vprev = 0, Iprev = 0;

double step = 0.007;
double D = 0.6;
double delay = 20;

//  Function Prototypes
void EPWM_Config(void);
void EPWM2_Config(void);

int main(void)
```

```
{
    Uint16 i;
    double sum1 = 0, sum2 = 0;

    // System Initialization
    InitSysCtrl();
    EALLOW;
    SysCtrlRegs.HISPCP.all = ADC_MODCLK;
    EDIS;

    DINT;
    InitPieCtrl();
    IER = 0x0000;
    IFR = 0x0000;
    InitPieVectTable();

    InitEPwm1Gpio();
    InitEPwm2Gpio();
    InitAdc();
```

```
// ADC Configuration
AdcRegs.ADCTRL1.bit.ACQ_PS     = ADC_SHCLK;
AdcRegs.ADCTRL3.bit.ADCCLKPS   = ADC_CKPS;
AdcRegs.ADCTRL1.bit.SEQ_CASC   = 1;
AdcRegs.ADCTRL3.bit.SMODE_SEL  = 1;
AdcRegs.ADCTRL1.bit.CONT_RUN   = 0;
AdcRegs.ADCTRL1.bit.SEQ_OVRD   = 1;
AdcRegs.ADCCHSELSEQ1.all       = 0x1;
AdcRegs.ADCCHSELSEQ2.all       = 0x1;
AdcRegs.ADCMAXCONV.bit.MAX_CONV1 = 0x0;

// Disable PWM synchronization for configuration
EALLOW;
SysCtrlRegs.PCLKCR0.bit.TBCLKSYNC = 0;
EDIS;

EPWM_Config();
EPWM2_Config();

// Enable PWM sync
```

```
EALLOW;
SysCtrlRegs.PCLKCR0.bit.TBCLKSYNC = 1;
EDIS;

// Start ADC Sequencer
AdcRegs.ADCTRL2.all = 0x2000;

while (1)
{
   // Clear buffers
   for (i = 0; i < BUF_SIZE; i++) {
      SampleTable1[i] = 0;
      SampleTable2[i] = 0;
   }

   sum1 = 0; sum2 = 0;

   // Sampling and Averaging
   for (i = 0; i < AVG; i++) {
      AdcRegs.ADCTRL2.bit.RST_SEQ1 = 1;
```

```
    AdcRegs.ADCTRL2.bit.SOC_SEQ1 = 1;
    AdcRegs.ADCTRL2.bit.INT_MOD_SEQ1 = 0;
    while (AdcRegs.ADCST.bit.INT_SEQ1 == 0) {}
    AdcRegs.ADCST.bit.INT_SEQ1_CLR = 1;

    SampleTable1[i] = (AdcRegs.ADCRESULT0 >> 4);
    SampleTable2[i] = (AdcRegs.ADCRESULT1 >> 4);
    sum1 += SampleTable1[i];
    sum2 += SampleTable2[i];
}

// ADC Calibration to Voltage and Current
FinalV1 = (sum1 / AVG) * 3.0 / 4096.0;
FinalI1 = (sum2 / AVG) * 3.0 / 4096.0;
Vi = (FinalV1 - 0.0006) / 0.001 + 8;
Ii = (FinalI1 - 2.48) * 6 / 0.625;

// Power and Delta Calculations
P = Vi * Ii;
dP = P - Pprev;
```

```
dV = Vi - Vprev;
dI = Ii - Iprev;

if (Vi > 10) {
    // Perturb & Observe MPPT Logic
    if (dP > 0) {
        if (dV > 0) D -= step;  // Keep increasing
        else        D += step;
    } else {
        if (dV > 0) D += step;
        else        D -= step;
    }

    // Clamp Duty Cycle
    if (D > D_MAX) D = D_MAX;
    if (D < D_MIN) D = D_MIN;

    // Update PWM Compare
    EPwm1Regs.CMPA.half.CMPA = D * count;
    EPwm2Regs.CMPA.half.CMPA = D * count;
```

```
        }


        // Save previous values
        Pprev = P;
        Vprev = Vi;
        Iprev = Ii;


        DELAY_US(delay);
    }
}


void EPWM_Config(void)
{
    EPwm1Regs.TBCTL.bit.CTRMODE = 0;      // Up-count mode
    EPwm1Regs.TBPRD = count;              // Set period
    EPwm1Regs.TBCTL.bit.CLKDIV = 0;
    EPwm1Regs.TBCTL.bit.HSPCLKDIV = 0;
    EPwm1Regs.TBPHS.half.TBPHS = 0x0000;
    EPwm1Regs.TBCTL.bit.PHSEN = 0;
    EPwm1Regs.TBCTR = 0;
```

```
    EPwm1Regs.TBCTL.bit.SYNCOSEL = TB_CTR_ZERO;
    EPwm1Regs.CMPCTL.bit.SHDWAMODE = 0;
    EPwm1Regs.CMPCTL.bit.SHDWBMODE = 0;
    EPwm1Regs.CMPCTL.bit.LOADAMODE = 0;
    EPwm1Regs.CMPCTL.bit.LOADBMODE = 0;
    EPwm1Regs.CMPA.half.CMPA = D * count;
    EPwm1Regs.AQCTLA.bit.ZRO = AQ_SET;
    EPwm1Regs.AQCTLA.bit.CAU = AQ_CLEAR;
    EPwm1Regs.DBCTL.bit.IN_MODE = 0;
    EPwm1Regs.DBCTL.bit.POLSEL = 0x02;
    EPwm1Regs.DBCTL.bit.OUT_MODE = 0x03;
    EPwm1Regs.DBRED = 10;
    EPwm1Regs.DBFED = 10;
}

void EPWM2_Config(void)
{
    EPwm2Regs.TBCTL.bit.CTRMODE = 0;      // Up-count mode
    EPwm2Regs.TBPRD = count;
    EPwm2Regs.TBCTL.bit.CLKDIV = 0;
```

```
    EPwm2Regs.TBCTL.bit.HSPCLKDIV = 0;
    EPwm2Regs.TBPHS.half.TBPHS = count / 2.02; // 180° phase shift
    EPwm2Regs.TBCTL.bit.PHSEN = 1;
    EPwm2Regs.TBCTR = 0;
    EPwm2Regs.TBCTL.bit.SYNCOSEL = TB_SYNC_IN;
    EPwm2Regs.CMPCTL.bit.SHDWAMODE = 0;
    EPwm2Regs.CMPCTL.bit.SHDWBMODE = 0;
    EPwm2Regs.CMPCTL.bit.LOADAMODE = 0;
    EPwm2Regs.CMPCTL.bit.LOADBMODE = 0;
    EPwm2Regs.CMPA.half.CMPA = D * count;
    EPwm2Regs.AQCTLA.bit.ZRO = AQ_SET;
    EPwm2Regs.AQCTLA.bit.CAU = AQ_CLEAR;
    EPwm2Regs.DBCTL.bit.IN_MODE = 0;
    EPwm2Regs.DBCTL.bit.POLSEL = 0x02;
    EPwm2Regs.DBCTL.bit.OUT_MODE = 0x03;
    EPwm2Regs.DBRED = 10;
    EPwm2Regs.DBFED = 10;
}
```

Appendix D. DSP Code for PI-based MPPT

```
#include "DSP28x_Project.h"

#include "math.h"

#include "stdlib.h"

#include "stdio.h"


// Function prototypes

void EPWM_Config(void);

void EPWM2_Config(void);


// ADC Configuration Macros

#if (CPU_FRQ_150MHZ)

  #define ADC_MODCLK 0x3  // 150/(2*3) = 25.0 MHz

#endif

#if (CPU_FRQ_100MHZ)

  #define ADC_MODCLK 0x2  // 100/(2*2) = 25.0 MHz

#endif


#define ADC_CKPS    0x5   // ADC clock prescaler
```

```
#define ADC_SHCLK   0x8   // Sample and Hold width = 16 ADC clocks

#define AVG         1000  // Averaging window

#define BUF_SIZE    1020  // ADC sample buffer size

#define freq        70000 // PWM switching frequency (Hz)


// Global Variables

Uint16 SampleTable1[BUF_SIZE];

Uint16 SampleTable2[BUF_SIZE];


double FinalV1 = 0, FinalI1 = 0;

double Vi = 0, Ii = 0;

int count = (150000000 / freq);

double P = 0, dP = 0, dV = 0, Pprev = 0, Vprev = 0;

double Vstep = 0.05, Vmax = 50.0, Vmin = 10.0;

double Vref = 30.0, integral = 0.0;

double Kp = -0.016, Ki = -5;

double Dmax = 0.7, Dmin = 0.3;

float Ts = 0.0002;

double D = 0.5, e = 0.1, delay = 20;
```

```
void main(void)
{
    Uint16 i;
    double sum1 = 0, sum2 = 0;

    // Initialize system
    InitSysCtrl();

    // ADC Clock Configuration
    EALLOW;
    SysCtrlRegs.HISPCP.all = ADC_MODCLK;
    EDIS;

    // Interrupt and vector table setup
    DINT;
    InitPieCtrl();
    IER = 0x0000;
    IFR = 0x0000;
    InitPieVectTable();
```

```
// GPIO & Peripheral Initialization
InitEPwm1Gpio();
InitEPwm2Gpio();
InitAdc();

// ADC Configuration
AdcRegs.ADCTRL1.bit.ACQ_PS = ADC_SHCLK;
AdcRegs.ADCTRL3.bit.ADCCLKPS = ADC_CKPS;
AdcRegs.ADCTRL1.bit.SEQ_CASC = 1;
AdcRegs.ADCTRL3.bit.SMODE_SEL = 1;
AdcRegs.ADCTRL1.bit.CONT_RUN = 0;
AdcRegs.ADCTRL1.bit.SEQ_OVRD = 1;
AdcRegs.ADCCHSELSEQ1.bit.CONV00 = 0x1;
AdcRegs.ADCCHSELSEQ2.all = 0x1;
AdcRegs.ADCMAXCONV.bit.MAX_CONV1 = 0x0;

// Disable PWM sync for configuration
EALLOW;
SysCtrlRegs.PCLKCR0.bit.TBCLKSYNC = 0;
EDIS;
```

```
EPWM_Config();
EPWM2_Config();

// Enable PWM sync
EALLOW;
SysCtrlRegs.PCLKCR0.bit.TBCLKSYNC = 1;
EDIS;

// Start ADC Conversion
AdcRegs.ADCTRL2.all = 0x2000;

while (1)
{
   // Reset ADC buffers
   for (i = 0; i < BUF_SIZE; i++) {
      SampleTable1[i] = 0;
      SampleTable2[i] = 0;
   }
```

```
sum1 = 0; sum2 = 0;


// ADC Sampling
for (i = 0; i < AVG; i++) {
   AdcRegs.ADCTRL2.bit.RST_SEQ1 = 1;
   AdcRegs.ADCTRL2.bit.SOC_SEQ1 = 1;
   AdcRegs.ADCTRL2.bit.INT_MOD_SEQ1 = 0;
   while (AdcRegs.ADCST.bit.INT_SEQ1 == 0) {}
   AdcRegs.ADCST.bit.INT_SEQ1_CLR = 1;

   SampleTable1[i] = (AdcRegs.ADCRESULT0 >> 4);
   SampleTable2[i] = (AdcRegs.ADCRESULT1 >> 4);

   sum1 += SampleTable1[i];
   sum2 += SampleTable2[i];
}

// Voltage and Current calculation
FinalV1 = (sum1 / AVG) * 3.0 / 4096.0;
FinalI1 = (sum2 / AVG) * 3.0 / 4096.0;
```

```
Vi = (FinalV1 - 0.0006) / 0.001 + 8;

Ii = (FinalI1 - 2.48) * 6 / 0.625;


// MPPT Algorithm

P = Vi * Ii;

dP = P - Pprev;

dV = Vi - Vprev;


if (Vi > 10) {

    // Perturb & Observe MPPT

    if (dP > 0 && dV > 0) Vref += Vstep;

    else if (dP > 0 && dV < 0) Vref -= Vstep;

    else if (dP < 0 && dV > 0) Vref -= Vstep;

    else if (dP < 0 && dV < 0) Vref += Vstep;


    // Clamp Vref

    if (Vref > Vmax) Vref = Vmax;

    if (Vref < Vmin) Vref = Vmin;


    Vprev = Vi;
```

```
    Pprev = P;

    // PI Controller
    e = Vref - Vi;
    integral += Ki * e * Ts;
    if (integral > Dmax) integral = Dmax;
    if (integral < Dmin) integral = Dmin;

    D = Kp * e + integral;
    if (D > Dmax) D = Dmax;
    if (D < Dmin) D = Dmin;
} else {
    D = 0.5;
}

// Update PWM Duty Cycle
EPwm1Regs.CMPA.half.CMPA = D * count;
EPwm2Regs.CMPA.half.CMPA = D * count;

DELAY_US(delay);
```

```
    }
}

void EPWM_Config(void)
{
    EPwm1Regs.TBCTL.bit.CTRMODE = 0;
    EPwm1Regs.TBPRD = count;
    EPwm1Regs.TBCTL.bit.CLKDIV = 0;
    EPwm1Regs.TBCTL.bit.HSPCLKDIV = 0;
    EPwm1Regs.TBPHS.half.TBPHS = 0;
    EPwm1Regs.TBCTL.bit.PHSEN = 0;
    EPwm1Regs.TBCTR = 0;
    EPwm1Regs.TBCTL.bit.SYNCOSEL = TB_CTR_ZERO;
    EPwm1Regs.CMPCTL.bit.SHDWAMODE = 0;
    EPwm1Regs.CMPCTL.bit.SHDWBMODE = 0;
    EPwm1Regs.CMPCTL.bit.LOADAMODE = 0;
    EPwm1Regs.CMPCTL.bit.LOADBMODE = 0;
    EPwm1Regs.CMPA.half.CMPA = D * count;
    EPwm1Regs.AQCTLA.bit.ZRO = AQ_SET;
    EPwm1Regs.AQCTLA.bit.CAU = AQ_CLEAR;
```

```
    EPwm1Regs.DBCTL.bit.IN_MODE = 0;
    EPwm1Regs.DBCTL.bit.POLSEL = 0x02;
    EPwm1Regs.DBCTL.bit.OUT_MODE = 0x03;
    EPwm1Regs.DBRED = 10;
    EPwm1Regs.DBFED = 10;
}

void EPWM2_Config(void)
{
    EPwm2Regs.TBCTL.bit.CTRMODE = 0;
    EPwm2Regs.TBPRD = count;
    EPwm2Regs.TBCTL.bit.CLKDIV = 0;
    EPwm2Regs.TBCTL.bit.HSPCLKDIV = 0;
    EPwm2Regs.TBPHS.half.TBPHS = count / 2.02;
    EPwm2Regs.TBCTL.bit.PHSEN = 1;
    EPwm2Regs.TBCTR = 0;
    EPwm2Regs.TBCTL.bit.SYNCOSEL = TB_SYNC_IN;

    EPwm2Regs.CMPCTL.bit.SHDWAMODE = 0;
    EPwm2Regs.CMPCTL.bit.SHDWBMODE = 0;
```

```
    EPwm2Regs.CMPCTL.bit.LOADAMODE = 0;
    EPwm2Regs.CMPCTL.bit.LOADBMODE = 0;
    EPwm2Regs.CMPA.half.CMPA = D * count;
    EPwm2Regs.AQCTLA.bit.ZRO = AQ_SET;
    EPwm2Regs.AQCTLA.bit.CAU = AQ_CLEAR;
    EPwm2Regs.DBCTL.bit.IN_MODE = 0;
    EPwm2Regs.DBCTL.bit.POLSEL = 0x02;
    EPwm2Regs.DBCTL.bit.OUT_MODE = 0x03;
    EPwm2Regs.DBRED = 10;
    EPwm2Regs.DBFED = 10;
}
```